IntechOpen

X-ray Characterization of Nanostructured Energy Materials by Synchrotron Radiation

Edited by Mehdi Khodaei and Luca Petaccia

X-RAY CHARACTERIZATION OF NANOSTRUCTURED ENERGY MATERIALS BY SYNCHROTRON RADIATION

Edited by **Mehdi Khodaei** and **Luca Petaccia**

X-ray Characterization of Nanostructured Energy Materials by Synchrotron Radiation
http://dx.doi.org/10.5772/62715
Edited by Mehdi Khodaei and Luca Petaccia

Contributors

Marco Giorgetti, Lorenzo Stievano, Marcel Miglierini, Vit Prochazka, Dino Tonti, Massimo Innocenti, Roberto Felici, Andrea Giaccherini, Won-Sub Yoon, Hyunchul Kim, Shoaib Muhammad, Mehdi Khodaei

Notice

First published in Croatia, 2017 by INTECH d.o.o.
eBook (PDF) Published by IN TECH d.o.o.
Place and year of publication of eBook (PDF): Rijeka, 2019.
IntechOpen is the global imprint of IN TECH d.o.o.
Printed in Croatia

Legal deposit, Croatia: National and University Library in Zagreb

Additional hard and PDF copies can be obtained from orders@intechopen.com

X-ray Characterization of Nanostructured Energy Materials by Synchrotron Radiation
Edited by Mehdi Khodaei and Luca Petaccia

p. cm.

Print ISBN 978-953-51-3013-0

Online ISBN 978-953-51-3014-7

eBook (PDF) ISBN 978-953-51-4896-8

Meet the editors

Mehdi Khodaei received his bachelor's degree in 2005 and master's degree in 2008 from the Department of Materials Engineering, Isfahan University of Technology, Iran. In 2014, he obtained his PhD degree from the University of Tehran, Iran in Nanotechnology-Materials Science under the supervision of Professor Seyyed Ali Seyyed Ebrahimi and under the advisement of Professor Sunggi Baik. His PhD thesis was on magnetoelectric multiferroic nanocomposite thin films and he has authored 10 peer-reviewed papers in this field. He was also a visiting researcher at Pohang University of Science and Technology (POSTECH), Korea, (March 2012–June 2013) working at Ferroelectric Nano Materials Lab. under the supervision of Prof. Sunggi Baik as well as Pohang Accelerator Laboratory (Korea Synchrotron facilities) under the supervision of Dr. Yong Jun Park. He is currently working as an assistant professor at Faculty of Materials Science and Engineering, K.N. Toosi University of Technology, Iran.

Luca Petaccia is a scientist and the head of the BaDElPh beamline at the Elettra Synchrotron Light Laboratory in Triest, Italy. He graduated in Physics, cum laude, from the Sapienza University of Rome in 1995 and earned his PhD degree in Physics from the University of L'Aquila in 2002. He was also a research fellow at the TASC-INFM national laboratory of Triest from 1997 to 2001. Then he has joined in Elettra as a beamline scientist and he has been promoted in charge of BaDElPh since 2007. He has a wealth of experience in photoemission spectroscopies and, in particular, in high-resolution angle-resolved photoemission spectroscopy (ARPES), which he exploits to carry out research in the fields of surface and nano science. To date, he has contributed over 100 publications in international peer-reviewed journals and has given several invited and oral contributions at various international meetings, schools, and conferences.

Contents

Preface

Nowadays, nanomaterials are attracting huge attentions not only from a basic research point of view but also for their potential applications. Since finding the structure-property-processing relationships can open new windows in the application of materials, the material characterizations play a crucial role in the research and development of materials science and engineering. Real-time and in-situ monitoring of the processing of nanomaterials is essential to understand their synthesis mechanism and properties. Since X-ray is sensitive to structural features with lengths from 10^{-3} to about 10 nm as well as to dynamic properties with characteristic time scales from about 10^{-16} to 10^{3} s, it is a powerful ingredient for exploring nanomaterials by X-ray–based techniques in the areas of scattering, diffraction, absorption, imaging, reflection, and photoelectron emission. Improvements in X-ray–based characterizations require increasing of the intensity, collimation, and focusing of the beam as well as tuning of the wavelength, which can be obtained by accelerator-based "light sources" facilities where investigations under specific conditions of pressure, temperature, and electric or magnetic fields, or even in-situ characterizations during synthesis, are possible.

The increasing demand for energy with the necessity to find alternative renewable and sustainable energy sources leads to the rapid growth in attention to energy materials. In this book, the results of some outstanding researches on synchrotron-based characterization of nanostructured materials related to energy applications have been collected. The editors would like to thank the authors for presenting their results and InTech for open access publication.

Mehdi Khodaei
K. N. Toosi University of Technology,
Iran

Luca Petaccia
Elettra Sincrotrone Trieste,
Italy

Chapter 1

Introductory Chapter: Synchrotron-Based X-Ray Characterization of Nanomaterials

Mehdi Khodaei and Luca Petaccia

Additional information is available at the end of the chapter

http://dx.doi.org/10.5772/67534

The capability of X-rays to analyze the structure and dynamics of almost all forms of matter has been largely demonstrated by scientific researches. Since X-rays are sensitive to structural features with lengths from 10^{-3} to about 1 nm as well as to dynamic properties with characteristic time scales from about 10^{-16} to 10^{3} s, they are a powerful ingredient for exploring nanomaterials and the frontiers of nanoscale characterizations. Developing in beams and optics to produce appropriate and tunable wavelengths/energies and detecting their interactions with matter create new windows to measure the arrangements of atoms (structure) and to track the movements of atoms or molecules (dynamics). The arrangement of atoms inside objects can be determined using several techniques based on scattering, diffraction, spectroscopy, and imaging. Moreover, X-ray interacts weakly with most materials; it is nondestructive and can penetrate deeply into samples. It can also be used for *in situ* studies of materials during processing and under real or extreme conditions of temperature, pressure, and magnetic or electric fields.

The improvements in X-ray diffraction, scattering, spectroscopy, and imaging methods need an increase in the intensity, collimation, and focusing of the beam as well as tuning of the wavelength. Hence, moving from X-ray laboratories to accelerator-based "light sources" facilities is required to obtain the most powerful analysis and characterization tools.

In a synchrotron, charged particles such as electrons are accelerated and injected into a storage ring, where they get energies from 500 MeV to 8 GeV depending on the size of the ring. As the charged particles are bent around the ring (by magnetic devices), energy is dissipated and electromagnetic radiation is emitted from infrared to X-rays. This radiation is highly intense, highly focused, and strongly polarized. Part of this radiation can emerge with energies from 0.1 keV (corresponding to a wavelength of 12.4 nm, known as "soft" X-rays) to 100 keV (0.0124 nm "hard" X-rays), being well suited to investigations at nanoscale (1–100 nm) [1].

The generation of X-rays by accelerators of electrons goes back to about 70 years ago. The first-generation sources were electron storage rings originally designed and operated for high-energy physics experiments. These facilities were adapted for use as synchrotron radiation sources by adding exit ports for the radiation. In the mid-1970s, facilities totally dedicated to synchrotron light were built. These facilities, in which synchrotron light was produced by bending magnets as well as high magnetic field devices, known as wigglers, are called second-generation sources. Afterwards, the optimization of magnetic structures, like in wigglers and undulators, produced new synchrotron radiation sources (named third generation) characterized by a X-ray more brighter than a conventional X-ray sources used in laboratories. The synchrotron X-rays are captured into beamlines where they can be tailored for scattering, diffraction, spectroscopy, and imaging with tailored resolution, intensity, or *in situ* measurements. While improvements in third-generation synchrotron radiation sources are still possible, *fourth-generation sources* are being developed, based on free electron lasers (FELs) that are able to produce very short coherent light pulses of very high peak intensity and brightness. The improvement of brightness for each generation of synchrotron X-ray sources along with a photograph of a synchrotron light source is shown in **Figure 1**.

The researches in nanomaterials are focused on producing nanoscale materials with unique properties for specific applications. Hence, the advanced characterizing methods for determining the structure, composition, and properties of materials at the nanoscale are needed. There is request on real-time and *in situ* monitoring of the synthesis and processing of nanomaterials to find the mechanisms as well as structure-property-processing relationships, which can be obtained by X-ray–based techniques in the areas of scattering, diffraction, absorption, imaging, reflection, and photoelectron emission as shown schematically in **Figure 2**. X-ray diffraction (XRD), X-ray fluorescence (XRF), X-ray photoelectron spectroscopy (XPS), and X-ray absorption spectroscopy (XAS), which includes X-ray absorption near-edge spectroscopy (XANES) and extended X-ray absorption fine structure (EXAFS), are well suited to probing synthetic processes at the atomic scale that are difficult or impossible to study with traditional electron imaging or spectroscopy techniques. For instance, *in situ* analysis by synchrotron radiations of vapor phase processing methods (chemical vapor deposition and atomic layer deposition), as well as etching methods such as reactive ion etching (RIE), and solution phase growth methods, such as the sol-gel process, has been performed by researchers [2].

Using synchrotron facilities, another analysis capability is the characterization of materials under specific conditions such as applied pressure, temperature, and fields. *Operando* experiments are the new frontier application of synchrotron-based characterizations, which can be pointed to understand energy storage materials research, such as Li-ion battery materials, which is included in the structural transformation during the fabrication of cathode materials and structural changes in the first lithium loading cycle as well as the investigations during the charging and discharging processes of an entire lithium battery. The fine spot size of the synchrotron X-ray beams together with their bulk penetration lead to study the buried layers in different battery components. The BL28XU beamline at SPring-8 in Japan has been recently installed for *in situ* structural and electronic analysis of rechargeable batteries, providing a powerful tool for the investigation of battery reactions. This beamline makes use

http://dx.doi.org/10.5772/67534

of quasi-monochromatic X-ray beams obtained by an in-vacuum tapered undulator, which allows to extend the energy bandwidth to 2 keV [3]. It consists of three hutches: one for the optics allocation and the other two as experimental stations as shown in **Figure 3**.

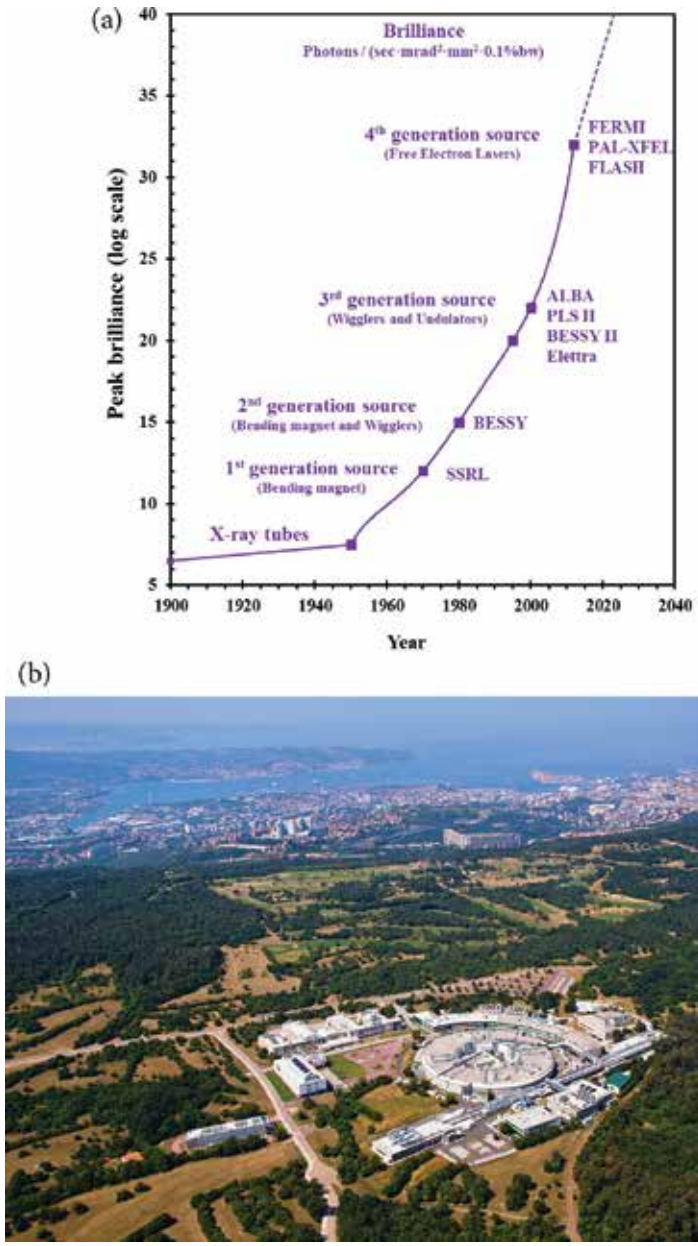

Figure 1. (a) Brightness of different generations synchrotron radiation sources, (b) aerial view of the Elettra synchrotron facility (Courtesy of Elettra Sincrotrone Trieste, ph. Gabriele Crozzoli).

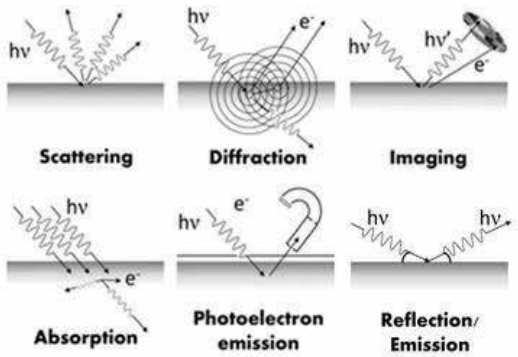

Figure 2. Schematic representation of some X-ray–based techniques due to the interaction of synchrotron radiation with matter (Courtesy of Elettra Sincrotrone Trieste).

At the ESCA, microscopy beamline of the Elettra synchrotron, a dynamic high pressure (DHP) system, has been recently developed. This setup is a solution adaptable to existing synchrotron-based XPS spectroscopes and microscopes, which allows to overcome the pressure constraints of photoemission technique (high vacuum or ultra-high vacuum) and to operate up to mbar range. The success of the first near ambient pressure scanning photoelectron microscopy experiment manifests that the developed novel solutions can pave the road to ambient pressure photoelectron spectromicroscopy, allowing for instance the characterization of catalytic systems near real condition [4].

In this book, five chapters on synchrotron-based characterization of nanostructured materials related to energy applications have been collected.

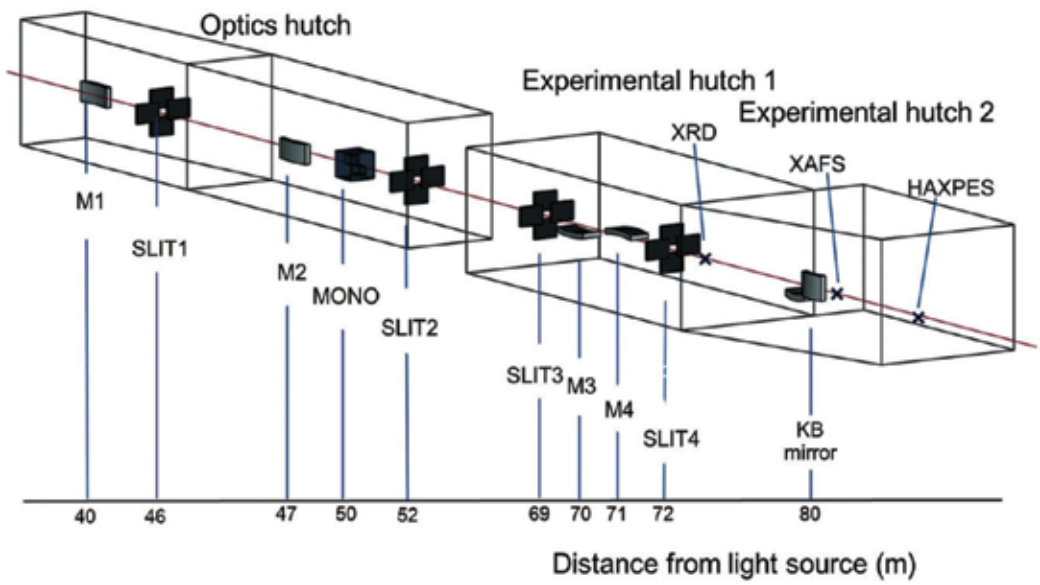

Figure 3. Schematic of beamline BL28XU at SPring-8 in Japan [3].

The chapter "Nanocrystallization of Metallic Glasses Followed by in situ Nuclear Forward Scattering (NFS) of Synchrotron Radiation" is about metallic glass materials, which have applications in energy transformation and sensor devices. Structural transformations in metallic glasses including nanocrystallization are investigated by Nuclear Forward Scattering (NFS) of synchrotron radiation to fine details that are completely hidden when conventional analytical tools are employed. The following chapter illustrates the operando structural characterization by surface X-ray diffraction (SXRD) of the electrochemical atomic layer deposition of semiconductor ultra-thin films, which have applications in nanoelectronics and photovoltaics. Last three chapters are dedicated to energy storage and battery materials, especially on Li-ion batteries, and their synchrotron-based characterization by X-ray absorption spectroscopy and X-ray microscopy.

Author details

Mehdi Khodaei[1]* and Luca Petaccia[2]

*Address all correspondence to: mehdi.khodaii@gmail.com, khodaei@kntu.ac.ir

1 Faculty of Materials Science and Engineering, K. N. Toosi University of Technology, Tehran, Iran

2 Elettra Sincrotrone Trieste, Trieste, Italy

References

[1] National Nanotechnology Initiative. X-rays and Neutrons: Essential Tools for Nanoscience Research. Report of the National Nanotechnology Initiative Workshop, June 16–18, 2005, Washington, DC.

[2] D. Attwood, Soft X-rays and Extreme Ultraviolet Radiation – Principles and Applications, Cambridge University Press New York, NY, USA, 2007.

[3] H. Tanida, et al., RISING beamline (BL28XU) for rechargeable battery analysis, J. Synchrotron Rad. 2014, 21, 268–272.

[4] H. Sezen, B. Aleman, M. Amati, M. Dalmiglio, L. Gregoratti, Spatially resolved chemical characterization with scanning photoemission spectromicroscopy: Towards near-ambient-pressure experiments, ChemCatChem. 2015, 7, 3665–3673.

Chapter 2

Nanocrystallization of Metallic Glasses Followed by *in situ* Nuclear Forward Scattering of Synchrotron Radiation

Marcel B. Miglierini and Vít Procházka

Additional information is available at the end of the chapter

http://dx.doi.org/10.5772/66869

Abstract

A central problem in nanotechnology is the understanding of structure-to-properties relationship. This is essential for tailoring the functionalities, efficiency, and performance of the near-future materials. Here, hyperfine interactions can be employed as they instantly reflect the state of structural arrangement. Examination of the corresponding hyperfine parameters during nanocrystallization through the use of the so-called nuclear forward scattering (NFS) of synchrotron radiation is now possible. One can follow separately structural evolution of different sites of the ^{57}Fe probe atoms. Structural transformations in metallic glasses including nanocrystallization were investigated by NFS to fine details that are completely hidden when conventional analytical tools are employed. Systematic analyses of NFS time-domain patterns provided an opportunity to study independently the role of structurally different regions. The latter comprise amorphous residual matrix, newly formed nanocrystallites, and interface regions. Different amounts of iron atoms located at the nanograins' surfaces and in their core were observed for different crystallization conditions, viz. temperature, time, and/or magnetic field. The application of in situ NFS experiments has a huge potential for observations of the evolution of phase transformations in real time performed on fly during short time intervals.

Keywords: metallic glasses, nanocrystallization, structural transformation, nuclear forward scattering, synchrotron radiation

1. Introduction

Understanding the structure-to-properties relationship is one of the most important problems in materials research. Thorough knowledge on structural arrangement namely in disordered systems like amorphous metallic alloys is essential for tailoring the functionalities, efficiency

and performance of devices based on these materials. Because of their amorphous nature, these metallic alloys are often referred to as metallic glasses (MGs). Their suitable chemical composition ensures formation of crystallites that grow inside the amorphous matrix during thermal annealing and measure only several nanometres in size. Due to these dimensions, they provide beneficial magnetic properties in these the so-called nanocrystalline alloys (NCAs). At the same time, formation of nanograins stabilizes the whole structure against further thermal deterioration.

Changes in microstructure, crystallization behaviour, and magnetic states of NCAs have suggested that interface regions between nanocrystalline grains and the surrounding amorphous matrix play a significant role in propagation of ferromagnetic exchange interactions between the nanograins through the residual amorphous matrix. In order to understand the process of nanocrystallization, it is inevitable to study it in situ, that is, *during* annealing. For this purpose, we use in situ nuclear forward scattering (NFS) of synchrotron radiation. NFS provides information on changes in structural arrangement via hyperfine interactions in real time. In this respect, it is superior to other in situ techniques.

This contribution aims at providing insight into the studies of structural transformations that are taking place in iron-based metallic glasses exposed to elevated temperatures. Evolution of nanocrystalline grains during dynamical increase of temperature and isothermal annealing is discussed by the help of NFS technique. Before doing that, we provide brief description of MGs and NCAs. In addition, a short review of the methods used for their structural characterization is also offered. Prior to introducing the results of NFS investigations, basic principles of this method are presented, too.

2. Metallic glasses and nanocrystalline alloys

Fe-based ferromagnetic MGs possess interesting physical properties that are superior to those of their crystalline counterparts. This is mainly due to lack of any long-range order, that is, periodic atomic arrangement that is particularly important for their magnetic performance [1, 2]. They are often employed as magnetic shielding, transformer cores, sensors, recording media [3] as well as in other technical applications [4].

Structural changes that can occur in MGs when they are exposed to high enough temperatures for extended operational times degrade their working parameters. This becomes particularly important with the onset of crystallization. On the other hand, suitable chemical compositions of some MGs assure formation of crystalline grains with typical sizes of up to several tens of nanometres. The resulting NCAs represent a novel type of materials whose physical properties can be tailored not only by appropriate chemical elements but also by varying the size of the nanocrystalline grains, their morphology, and the composition of nanograins. NCAs all can be prepared from MGs by annealing under well-defined conditions (temperature and time) which ensure controlled temperature treatment and trigger partial crystallization. In opposite to MGs, the magnetic parameters of NCAs do not substantially deteriorate at elevated temperatures [5]. Therefore, a comprehensive understanding of the

http://dx.doi.org/10.5772/66869

evolution of nanograins during nanocrystallization is essential in order to understand, optimize, and conserve the unique magnetic properties exhibited by metallic glasses and/or their nanocrystalline counterparts.

Though studied already for decades, MGs still attract the interest of researchers due to their unique physical properties [6]. A central problem seems to be the understanding of structure-to-properties relationship namely when MGs are transformed into NCAs. This is essential for tailoring the functionalities, efficiency, and performance of these near-future materials. These phenomena are routinely studied in a steady state, that is, once the particular structural arrangement is achieved, it is correlated with the resulting physical properties. Less attention is paid to the investigation of transient states that temporarily exist *for the period of* a structural transformation. Such an approach is, however, a demanding experimental task.

Broad arsenal of diagnostic techniques is applied in order to understand the process of transformation from MG into NCA structural arrangement, that is, the crystallization of MGs [7–9]. Yet, majority of these techniques provide only *ex situ* information as the time needed for acquisition of sufficiently good statistics of the experimental data frequently extends over several tens of minutes or even hours. In addition, some of the imaging techniques require special treatment for sample preparation which can substantially affect their structure. Subsequently, in situ investigation of the induced structural transformations using these techniques is not possible in real time, and the study of dynamics and/or kinetics of crystallization process is not so straightforward.

Methods like DSC or magnetic measurements can examine materials in real time and, thus, provide in situ investigations. However, they scan the whole bulk of the investigated systems. As a result, the obtained information is averaged over all structurally different regions which are present in the studied system. That is why in situ characterization of structural transformations during crystallization of MGs is an experimental challenge.

Along with conventional analytical tools, also sophisticated and advanced techniques like atom probe tomography are employed [10]. The use of in situ characterization techniques is, however, still limited to diffraction of synchrotron radiation [11–13]. Recently, more sophisticated techniques of real-time in situ synchrotron X-ray tomographic microscopy [14] and combination of time-resolved X-ray photon correlation spectroscopy and high-energy XRD [15] were applied. All these studies which make use of very up-to-date synchrotron-based approaches provide valuable information of amorphous structures by revealing complex atomic rearrangements even though no well-defined structural positions exist in MGs.

Though X-ray diffraction based techniques are capable of in situ investigations, they do not provide site-specific information as the signal is averaged over the distribution of electron densities. From this point of view, use of local probe techniques such as Mössbauer spectroscopy offers unique opportunities to access both magnetic properties and structural states of the investigated material [16]. The relatively long acquisition times of a conventional Mössbauer spectrum (up to several hours), however, limit the application of this technique only to samples in steady equilibrium conditions. This substantially disables monitoring of the crystallization process itself.

3. Nuclear forward scattering of synchrotron radiation

Progress in synchrotron sources of radiation has introduced the method of nuclear forward scattering of synchrotron radiation [17]. This method uses ^{57}Fe resonant nuclei as probes of the local magnetic and electronic properties in the investigated samples. Thus, information on hyperfine interactions similar to Mössbauer spectrometry is readily available. Application of NFS is helpful in revealing the mutual relation between the magnetic arrangement and the structure of the studied materials. Due to extremely high brilliance of the latest synchrotron sources, studies can be performed in dynamic in situ regimes. Rapid recording of experimental data allows for direct observation of dynamical processes that are taking place *during* heat treatment [18–22].

In this contribution, we discuss time aspect of NFS which enables time-dependent processes to be followed in real time. We demonstrate them using dynamical and kinetics processes that are taking place during nanocrystallization of selected MGs. Before doing so, let us mention another important technique which exploits nuclear properties of ^{57}Fe resonant nuclei that are activated by synchrotron radiation. It is the so-called nuclear inelastic scattering (NIS) of synchrotron radiation. It enables studies of the dynamics of NCAs via atomic vibrations and densities of phonon states [23, 24]. Because the time needed for acquisition of experimental data is still rather long, time-dependent NIS investigations are only evolving.

NFS belongs to the family of nuclear resonant scattering processes [25]. This technique can be considered as a full analogue of Mössbauer spectrometry [26]. It is especially useful under extreme conditions including high temperature, pressure, and/or magnetic fields when the space with such an environment is very limited, and hence, the sample can be as small as several tens of micrometers. High brilliance of synchrotron sources enables sufficient data counts even from such spatially limited regions. NFS permits on fly inspection of structural and/or magnetic arrangement that continuously evolves with changing temperature/time. In this respect, it is superior to other in situ techniques.

Energetic levels of atomic nuclei are exposed to the so-called hyperfine interactions. The latter are due to an effective field that originates from the presence of surrounding atoms, their electronic shells, and/or external fields. Consequently, nuclear levels are shifted and/or split, and in this way, they sensitively reflect chemical and topological states of the resonant atoms. Effect of the three main types of hyperfine interactions, viz. electric monopole, electric quadrupole, and magnetic dipole interaction upon nuclear levels, is schematically drawn in the upper part of **Figure 1**. Possible transitions among nuclear levels are indicated by arrows.

Electric monopole interaction is proportional to charge density at the nucleus and provides information about valence and spin states of the resonant atom, about its electronegativity and chemical bonding. Electric quadrupole interaction is governed by electric field gradient acting upon the nucleus and reflects the charge distribution. It is related to oxidation state, spin state as well as symmetry of the positions of resonant atoms. Magnetic dipole interaction

http://dx.doi.org/10.5772/66869

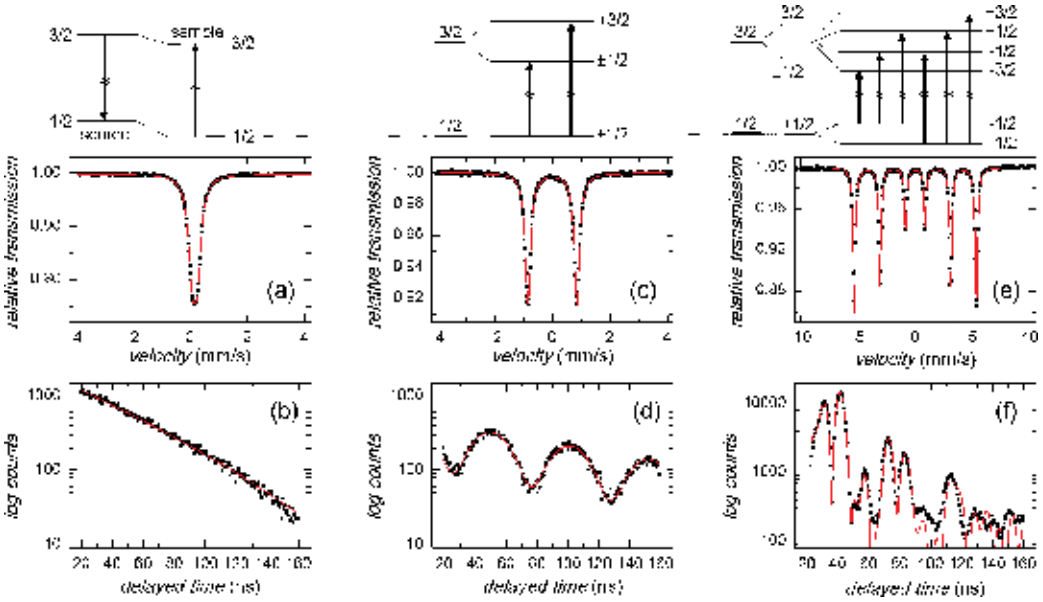

Figure 1. Typical representatives of the basic shapes of Mössbauer spectra recorded in energy domain (middle row) and the corresponding NFS time-domain patterns (bottom row). They demonstrate presence of electric monopole (a and b), electric quadrupole (c and d), and magnetic dipole (e and f) hyperfine interactions that cause the shift/splitting of nuclear levels as drawn in the top row.

originates from coupling between nuclear magnetic moment and effective magnetic field at the nucleus due to spin polarization. Thus, information on magnetic states of the resonant atoms, which is, moreover, temperature-dependent, is readily available. It is noteworthy that resonant atoms located in defined structural positions (e.g., in a crystalline lattice) feature individual set of hyperfine interactions and, hence, corresponding spectral parameters. The latter are like fingerprints which uniquely identify these particular atomic sites and can be derived either from Mössbauer spectra or from NFS experiments. In addition, relative fractions of such structurally different positions in the investigated samples are related to the contribution of the particular spectral components.

Transitions between ground and excited states of the resonant nuclei are accompanied by absorption and emission of photons with precise energy that is typically several tens of keV. In conventional Mössbauer spectrometry, resonance absorption of the emitted gamma photons by a particular absorber (i.e., the investigated sample) is achieved by fine tuning of their energy through a Doppler effect [27]. As a source of radiation, suitable radioactive nuclides are used. Splitting of nuclear energy levels is of the order of several hundreds of neV and is reflected via corresponding hyperfine parameters in the associated Mössbauer spectra that are recorded in energy domain. The resulting basic shapes of Mössbauer spectra are depicted in the middle row of **Figure 1**.

If only electric monopole hyperfine interaction occurs, the corresponding Mössbauer spectrum shows only one line, the so-called singlet as seen in **Figure 1a**. Presence of electric quad-

rupole interaction at the resonating nuclei splits the excited level into two degenerating ones. Consequently, in the case of ^{57}Fe nuclei (nuclear spin 3/2 in the excited state and 1/2 in the ground state), two transitions are possible. Hence, a doublet of absorption Mössbauer lines is formed as seen in **Figure 1c**. Zeeman-split sextet is observed in **Figure 1e** when magnetic dipole interactions act upon the ^{57}Fe resonant nuclei. Presence of sextets in Mössbauer spectra indicates that the corresponding fraction of iron atoms (represented by a spectral area under the absorption lines) is ferro-, ferri-, or antiferromagnetically ordered. In real samples, any combination of the three basic spectral shapes is possible.

With the development of monochromators, synchrotron radiation turned out to be suitable candidate for replacing conventional radionuclide sources of photons. As schematically depicted in the upper part of **Figure 2**, bunches of accelerated particles (electrons) produce flashes of synchrotron radiation when they pass through undulators. Pulses of photons have typical duration of ~50 ps and repetition rate ~200 ns. Their energy is tuned to the requested Mössbauer transition using high-resolution monochromator that provides energies of photons within a bandwidth (ΔE_γ) of several meV. The pulse contains wider range of energies than is needed for excitation of available nuclear levels in the studied sample. It is drawn in the bottom part of **Figure 2** as a broad (blue) arrow and ensures immediate excitation of all nuclear transitions. Energy separation of nuclear levels due to hyperfine interactions is of the order of several hundreds of neV. Thus, not only the different transitions of the same nucleus but also all transitions of different nuclei are excited simultaneously at the *same time* upon an impingement of the synchrotron radiation pulse upon the sample. Let us remind that in Mössbauer spectrometry, nuclear transitions are excited sequentially one by one as the energy of photons varies over specific values.

In the time slot between two subsequent pulses, all excited nuclei emit the excess energy in a form of resonance delayed photons that are registered with a fast detector. The decay of the

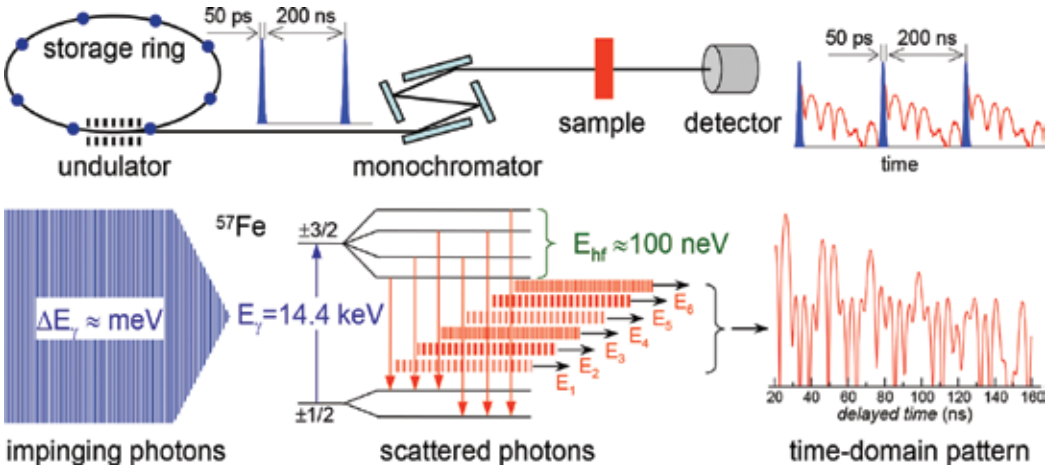

Figure 2. Basic layout of a typical NFS beamline with the major components (upper part). In the bottom part, magnetically split nuclear levels are simultaneously excited by a single pulse of incident synchrotron radiation with an energy spread $\Delta E_\gamma \approx$meV. Subsequent de-excitation provides scattered photons of different energies (E_1–E_6) that sum up to the NFS time domain pattern.

http://dx.doi.org/10.5772/66869

nuclear excited states reflects hyperfine interactions of the resonant nuclei. All de-excitation photons sum up and give rise to interference patterns in time domain as shown in the bottom row of **Figure 1**. In the following, we will call them *NFS time-domain patterns*.[1] The prompt excitation pulse sets the time zero. Due to its extremely high intensity the detector starts to count when only delayed photons are present which usually takes about 10–20 ns after the excitation.

The counts of delayed photons are registered as a function of time that has elapsed after the excitation. That is why NFS is sometimes referred to as Mössbauer spectrometry in time domain. Single transition is characterized by an exponentially decaying signal (linear in semi logarithmic scale, see **Figure 1b**). Multiple photons originating from multiple transitions exhibit characteristic beating of intensities called quantum beats. Their character is unique for particular hyperfine structure as demonstrated in **Figure 1d** and **f** for electric quadrupole and magnetic dipole interactions, respectively.

In general, any NFS time-domain pattern can be represented by some of the basic patterns plotted in the bottom row of **Figure 1** and/or a combination of them. In any case, they carry information on hyperfine interactions that are unique for individual atomic sites of the resonant atoms. Evaluation of experimental NFS data is performed by their fit to a suitably chosen theoretically calculated model. Each model consists of several sets of hyperfine parameters that are each ascribed to one particular atomic site. The obtained resulting parameters identify valence states, symmetry of charge distribution, and magnetic ordering. Phase composition of the material under study can be identified, and relative amount of each phase can be determined. Due to high site selectivity, we can study local electronic arrangement, and its fine distortions can be revealed. Some parameters like, for example, electric field gradient can be compared with the results of ab initio calculations. We can also easily follow magnetization of individual magnetic structures via hyperfine magnetic fields within magnetically active materials. So far, NFS technique was successfully applied to the study of different problems of materials research [28].

In this contribution, we present in situ NFS experiments that provide important information on the early stages of crystallization in MGs. This process can be monitored starting from formation of nucleation centres, their growth, and continuation towards equilibrium nanocrystalline state. Using this approach, the obtained results are not affected by a cooling process which is the case when ex situ experiments are employed.

4. Experimental particulars

4.1. NFS experiments

NFS experiments were performed at The European Synchrotron (ESRF), Grenoble using the Nuclear Resonance ID22N and ID18 stations. Excitation of the ^{57}Fe nuclear levels was accom-

[1] In a literature, one can find the expression 'NFS time spectrum'. However, the term 'spectrum' implies a dependence of counts upon energy. Because of the interference nature of NFS data, we find it physically inconsistent.

plished by a photon beam with the energy of 14.413 keV, flux of ~10^9 photons/s, and bandwidth of ~3 meV. The spot size of the synchrotron beam was of 0.7×0.3 mm^2. The estimated heat load at the sample was ~2 μW. Samples of the investigated MGs were placed in a vacuum furnace. Metallic glasses of $Fe_{90}Zr_7B_3$, $Fe_{81}Mo_8Cu_1B_{10}$, and $(Fe_{2.85}Co_1)_{77}Mo_8Cu_1B_{14}$ were prepared by the method of rapid quenching on a rotating wheel. The chosen compositions of MGs ensure formation of nanocrystalline alloys in which crystalline grains with the size of several nanometres are formed in the early stage of structural transformation. The obtained ribbons of MGs were ~1–2 mm wide and ~20 μm thick.

The maximum annealing temperature (up to ~700 °C) was limited by Kapton windows of the furnace. Nevertheless, this temperature was far behind the first crystallization step of the investigated MGs.

Two types of studies were performed: (i) dynamical time-dependent temperature increase/decrease and (ii) isothermal heat treatment. During the first type of experiments, temperature at the sample was continuously increasing with a ramp of 10 K/min. In the second type of experiments, the set temperature was reached with a ramp of 40 K/min and then maintained for up to 3 h. In both cases, NFS time-domain patterns were continuously recorded every minute during the whole duration of the experiment performed in transmission geometry. Thus, information on the bulk of the samples was obtained.

For the sake of more clear presentation of a high quantity of experimentally acquired time-domain patterns within a single experiment, we use contour plots to display the obtained NFS patterns. The latter are stacked with respect to the duration time of the experiment which constitutes the vertical axes of the contour plots. For dynamical experiments, this axis' scale is eventually converted into temperature values assuming a constant ramp of 10 K/min. The elapsed time is then given on the horizontal axes, and the counts of the registered photons (intensities) are colour coded in a logarithmic scale.

4.2. Physical models for the evaluation of NFS time-domain patterns

Fitting of the experimental data was performed by the CONUSS software package [29, 30] which is suitable for the evaluation of individual NFS time-domain patterns. However, the accomplished NFS experiments have provided a huge number of records. Typically, several tens (up to ~140) of time-domain patterns were obtained during one experiment. In order to process and subsequently evaluate such enormous data quantities, we have developed special software called Hubert [31]. The data evaluation is based on the conventional fitting route using CONUSS software. Hubert is designed for NFS time-domain patterns processing, time calibration, transformation from synchrotron output file format to experimental data file readable by CONUSS, a single time-domain pattern evaluation, large data sets analysis, and generation of hyperfine parameters distributions [32].

The investigated MGs are amorphous in the as-quenched state. Depending upon their composition, they are ferromagnetic ($(Fe_{2.85}Co_1)_{77}Mo_8Cu_1B_{14}$) and paramagnetic ($Fe_{90}Zr_7B_3$, $Fe_{81}Mo_8Cu_1B_{10}$) at room temperature. Consequently, the originally amorphous matrix is reproduced in the NFS time-domain patterns by distributions of hyperfine magnetic fields

http://dx.doi.org/10.5772/66869

and distributions of quadrupole splitting, respectively. With increasing temperature of measurement, magnetic dipole interactions eventually vanish, and only electric quadrupole ones are present. While the latter are fitted by distribution of quadrupole splitting, only this component is used to characterize the amorphous matrix in the particular MG.

After the onset of crystallization, that is, when the temperature of measurement reaches the first crystallization step, nanocrystalline grains emerge within the residual amorphous matrix. Because of the samples' composition, they are bcc-Fe or bcc-(Fe,Co) nanocrystals. Both exhibit rather strong magnetic dipole interactions which are represented by quantum beats with relatively high frequency of oscillations (see also **Figure 1f**). The associated fitting component features well-defined hyperfine magnetic field values, and it is ascribed to the inner part of the nanocrystalline grains with well-established crystalline symmetry. Atoms located at the surfaces of the nanograins exhibit broken symmetry, and they are referred to as interface regions [18]. Though still magnetic, their associated fitting component is represented by distributions of hyperfine magnetic fields with average field values lower by ~2–3 T than those of the core of the nanograins. Presence of this component was confirmed by conventional Mössbauer spectrometry [33].

To recapitulate the fitting models applied for the evaluation of the obtained NFS time-domain patterns, it should be noted that we distinguish three structurally different regions in the investigated samples. The first one is amorphous matrix which corresponds to the whole MG in its original as-quenched state as well as during moderate heat treatment up to the onset of crystallization. When the temperature exceeds the crystallization point, this structural component represents the residual amorphous matrix in the newly formed NCA. Both amorphous regions will be denoted in the following as AM—amorphous. Because AM can be either magnetic or paramagnetic (depending upon the sample's composition and/or temperature), this component is refined by distributions of hyperfine magnetic fields and quadrupole splitting, respectively.

Well-defined structural arrangement of the evolving nanocrystalline grains stands for the second structural region which will be labelled as CR—crystalline. In the NFS time-domain

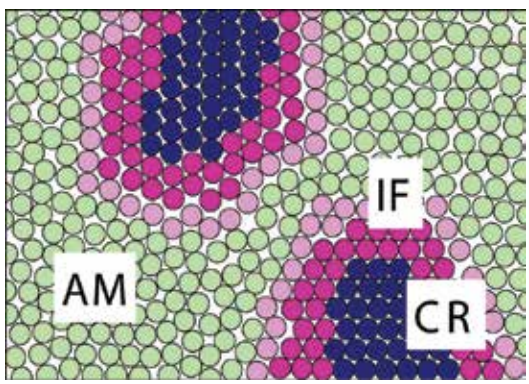

Figure 3. Schematic representation of a nanocrystalline structure that includes the residual amorphous matrix (light green)—AM, inner parts (core) of nanocrystalline grains (dark blue)—CR, and interfacial regions (violet)—IF.

patterns, it is refined by a sharp value of magnetic hyperfine field. The third structural component is interpreted as interface region (IF) between the former two structures. It constitutes a shell of the nanograins with undeveloped crystal symmetry. During the evaluation, it is refined by a distribution of hyperfine magnetic fields. Schematic representation of this concept is presented in **Figure 3**.

Hyperfine parameters of all fitting components evolve with temperature/time of the experiment. Eventually, at certain temperatures (e.g., Curie temperature, onset of crystallization), qualitatively different hyperfine interactions appear. Consequently, the physical model should reflect this situation by the use of appropriate type of distributions of hyperfine parameters (magnetic fields vs. quadrupole splitting). Proper type of distribution in certain temperature/time region is chosen by the help of the Hubert software [32].

5. Structural transformations in metallic glasses

5.1. Dynamical experiments

Effects of continuously changing temperature on magnetic ordering and structural transformation in MGs are demonstrated using the $(Fe_{2.85}Co_1)_{77}Mo_8Cu_1B_{14}$ amorphous alloy. This chemical composition ensures ferromagnetic states of the as-quenched MG at room temperature. Corresponding NFS time-domain patterns are plotted in **Figure 4**.

It should be stressed that the NFS time-domain patterns in **Figure 4** are in fact raw measured data as obtained directly from the experiment. Even without any quantitative evaluation, two qualitative changes in the character of interferograms are clearly observed at ~247 and ~435 °C. They are associated with magnetic and structural transformation, respectively, characterized

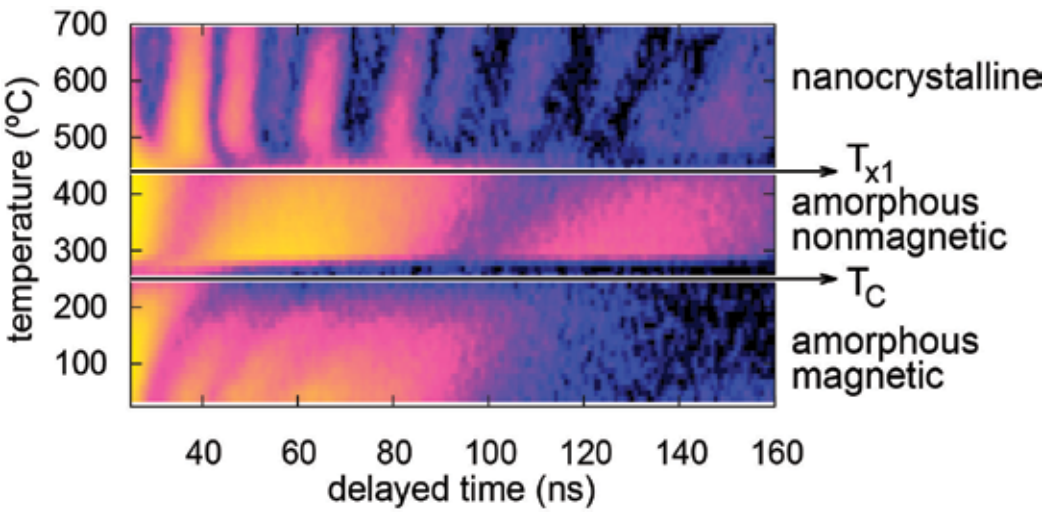

Figure 4. Contour plot of NFS time-domain patterns accumulated during dynamic annealing of the $(Fe_{2.85}Co_1)_{77}Mo_8Cu_1B_{14}$ MG. Heating rate is 10 K/min.

http://dx.doi.org/10.5772/66869

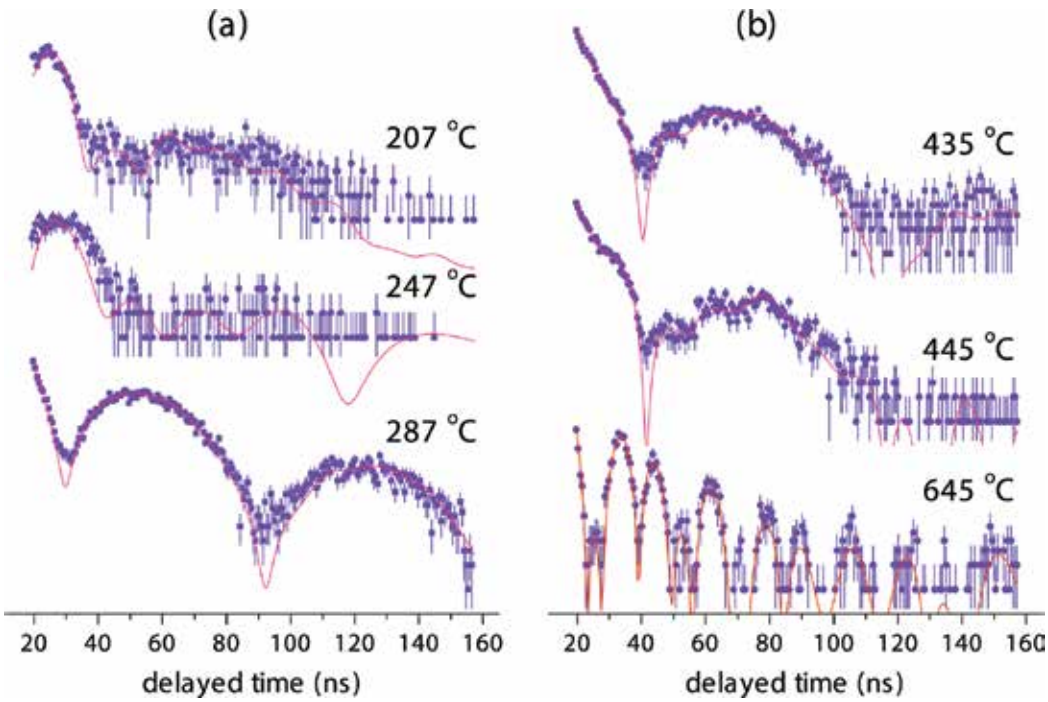

Figure 5. NFS time-domain patterns of the $(Fe_{2.85}Co_1)_{77}Mo_8Cu_1B_{14}$ MG taken at the vicinity of T_C (a) and T_{x1} (b) at the indicated temperatures.

by Curie T_C and crystallization T_{x1} temperatures. Consequently, the whole temperature region can be divided into three areas where the investigated MG exhibits magnetic amorphous, nonmagnetic amorphous, and magnetic nanocrystalline structure as it is shown in **Figure 4**.

In order to illustrate the alternations in the shapes of NFS time-domain patterns, selected individual records are plotted in **Figure 5**. It should be noted that the thickness effect of the sample has an important impact on the time-domain patterns. It results in the so-called hybrid beat character [34] which alternates their shapes.

With increasing temperature during the dynamic experiment, we can observe shift of the quantum beats maxima towards higher delayed times. Simultaneously, their intensities decrease. These effects are connected with vanishing hyperfine magnetic fields as a function of temperature. Magnetic quantum beats eventually fade away when the temperature reaches T_C and the Zeeman sextet collapses. At this temperature, the six de-excitation photons have comparable energies that are moreover overlapped within the line width. The resulting interference pattern in time domain exhibits very fast time decay, and the corresponding NFS time-domain pattern nearly disappears. This situation is demonstrated in **Figure 5a** where selected records taken at the vicinity of T_C~247 °C are plotted.

Formation of nanocrystalline bcc-(Fe,Co) grains during the first crystallization step resumes magnetic interactions that are identified by the corresponding quantum beats in **Figure 5b**.

For comparison, NFS time-domain patterns at 435, 445, and 645 °C were chosen. At 435 °C, the the sample is still fully amorphous and paramagnetic, that is, only electric quadrupole interactions are present (compare **Figure 1d**). With the onset of nanocrystallization, more rapid oscillations, which represent hyperfine magnetic fields, appear in time region 43–83 ns. At 445 °C, they are already satisfactorily visible. Finally, at 645 °C, the NFS time-domain pattern clearly shows well-developed magnetic structure (see also **Figure 1f**) which means that the degree of crystallization is significantly high.

The temperature of the onset of the first crystallization T_{x1} can be, however, accurately determined taking into consideration the whole temperature dependence of relative areas of amorphous (AM) and crystalline (CR) fitted components plotted in **Figure 6**. The total number of counts, that is, the overall area under time-domain patterns, is also provided. Here, the local minimum at ~247 °C indicates T_C of the amorphous matrix. The successive abrupt increase is associated with magnetic transformation inside the amorphous matrix. Further continuous decrease in the total counts is caused by temperature dependence of the f-factor. The onset of nanocrystallization is documented in **Figure 6a** by a notable change in the slope of the curve where the inflection point represents T_{x1} ~435 °C. The same T_{x1} is derived from temperature dependence of relative area of the CR component in **Figure 6b**. Surface crystallization starts at somewhat lower T_{x1} ~410 °C as confirmed by CEMS measurements [35].

The onset of crystallization changes the character of the beats. When new nanocrystalline grains appear, a magnetic order is established among the newly formed bcc-(Fe,Co) grains. This is indicated by an occurrence of dipole magnetic interactions that exhibit themselves by high-frequency oscillations in the corresponding NFS time-domain patterns in **Figures 4** and **5b**. The behaviour of the amorphous matrix with temperature is more complex. It can be followed by evolution of hyperfine magnetic fields in the temperature region where the system is ferromagnetic and by quadrupole splitting values at $T>T_C$. Both parameters are plotted in **Figure 7**.

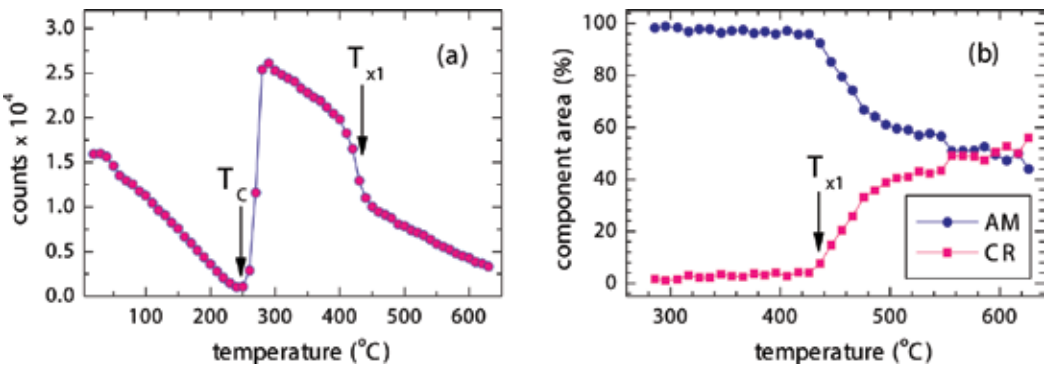

Figure 6. Total number of counts (spectral area) (a) and relative fractions of AM and CR components (b) of NFS time-domain patterns of the $(Fe_{2.85}Co_1)_{77}Mo_8Cu_1B_{14}$ MG plotted against temperature. Transition temperatures T_C and T_{x1} are marked with arrows.

http://dx.doi.org/10.5772/66869

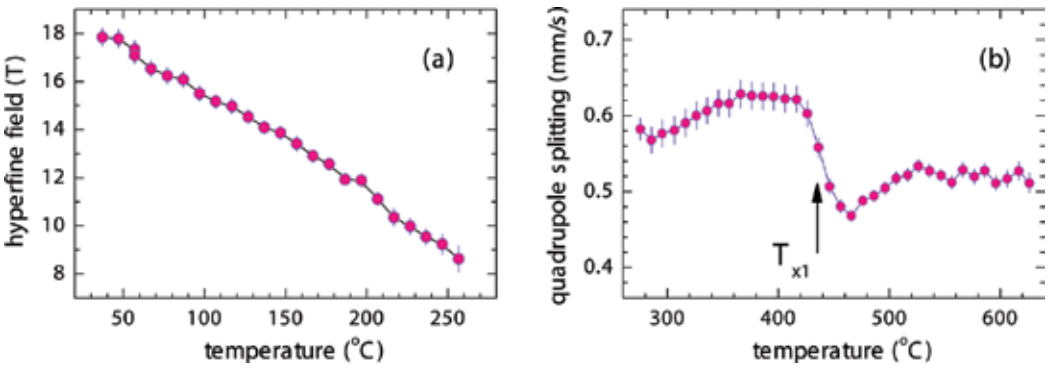

Figure 7. Average hyperfine magnetic field (a) and quadrupole splitting (b) values of the amorphous matrix in the $(Fe_{2.85}Co_1)_{77}Mo_8Cu_1B_{14}$ MG plotted against temperature.

For temperatures up to T_C, the hyperfine magnetic fields continuously decrease till they acquire values that are comparable in strength with electric quadrupole interactions. It should be noted that both types of hyperfine interactions coexist in some temperature range. In fact, it is impossible to distinguish between them also because of low total number of counts in the NFS time-domain patterns (see **Figures 5a** and **6a**). Here, the fitting is accomplished by two qualitatively distinct models, viz. distribution of hyperfine magnetic fields and distribution of quadrupole splitting. They are applied in certain temperature regions that approach T_C from bottom (i.e., $T<T_C$) and from top ($T_C<T$), respectively, with some small overlap [32].

Temperature evolution of quadrupole splitting provides information about bond properties and local symmetry of the iron sites in the AM phase. It shows a local minimum in **Figure 7b**. The associated inflection point indicates T_{x1}. Above this onset of nanocrystallization, the residual AM phase still persists, and when the CR phase is well developed (T>~500 °C), the average quadrupole splitting is stabilized.

To summarize the above discussion, we would like to note that the $(Fe_{2.85}Co_1)_{77}Mo_8Cu_1B_{14}$ MG was intentionally chosen to demonstrate the possibilities of dynamical NFS experiments. It is possible to follow on fly not only the evolution of its structural arrangement but also that of hyperfine magnetic interactions.

5.2. Dynamical experiments in external magnetic field

In order to improve magnetic parameters of nanocrystalline alloys, crystallization of metallic glasses often takes place under external magnetic field, the so-called magnetic annealing [36]. It results in appearance of induced magnetic anisotropy in heat-treated soft MGs. Nevertheless, all studies are performed ex situ after the magnetic annealing. Naturally, a question has arisen how external magnetic field affects the progress of nanocrystallization.

Similar as in the previous experiment, in situ investigations can be effectively performed by dynamical increase of temperature without and with external magnetic field by employing the NFS technique. But now, we have selected MG that is almost purely paramagnetic at

room temperature, namely $Fe_{81}Mo_8Cu_1B_{10}$. Only minute amounts of surface crystallization were unveiled by CEMS [37] on both sides of ribbon-shaped samples.

The reason for choosing this MG was twofold: (i) this chemical composition leads to formation of bcc-Fe nanocrystals, and iron is a calibration material for these studied; hence, its hyperfine parameters are well known, and (ii) the fitting model used for evaluation of the experimental NFS data is more simple because the residual amorphous matrix is paramagnetic, and only distributions of quadrupole splitting are used. On the other hand, formation of bcc-Fe nanograins imposes magnetic dipole interactions that are represented by single hyperfine magnetic field value. As described in the Section 4.2, iron atoms located in interface regions can be also identified via distribution of hyperfine magnetic fields. Consequently, temperature evolution of three structurally different regions in the investigated MG can be studied.

Contour plots of NFS time-domain patterns recorded during continuous increase of temperature in zero-field conditions and with applied external magnetic field (0.652 T) are shown in **Figure 8**. Dramatic impact of this rather small external magnetic field upon dynamics of the crystallization process is clearly seen. The plotted experimental data exhibit obvious modifications of hyperfine interactions that are reflected in the shapes of NFS time-domain patterns. At room temperature, the investigated $Fe_{81}Mo_8Cu_1B_{10}$ MG is amorphous, and in zero-field conditions, it demonstrates prevailing electric quadrupole interactions with hardly visible beatings of magnetic origin (due to surface crystallization). With the onset of nanocrystallization, contribution of magnetic dipole interactions becomes better visible in **Figure 8a** in the vicinity of ~400 °C. Appearance of hyperfine magnetic fields is remarkably accelerated when the annealing is performed in external magnetic field. In **Figure 8b**, the same character of NFS time-domain pattern is observed earlier at a temperature that is by about 100 °C lower.

Quantitative and qualitative description of the time-domain patterns is presented in **Figure 9** as derived from zero-field and in-field NFS experiments. Relative amounts of individual

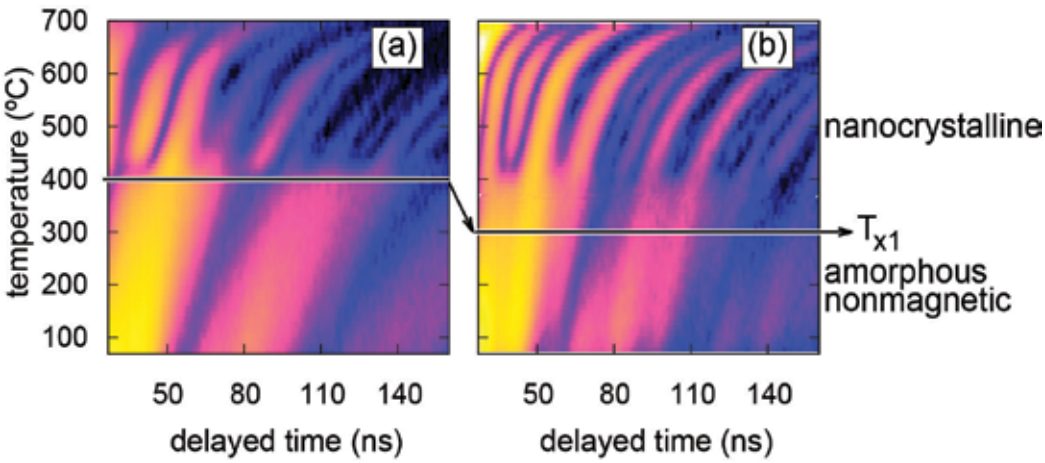

Figure 8. Contour plots of NFS time-domain patterns of the $Fe_{81}Mo_8Cu_1B_{10}$ MG measured without (a) and with external magnetic field of 0.652 T (b).

http://dx.doi.org/10.5772/66869

components comprising relative areas of the amorphous (AM) and total nanocrystalline (CR+IF) phases are shown in **Figure 9a**. It is noteworthy that the onset of crystallization should be determined from the temperature dependences of the relative areas rather than from the contour plots in **Figure 8**. In the latter, intensities of the NFS time-domain patterns are plotted in logarithmic scale, and thus, the applied colour-coded scale is coarse to a certain extent. Consequently, fine details of the particular line shapes might not be properly seen.

Presence of small number of quenched-in nanocrystallites (~10 %) that were formed during the production of the ribbons was unveiled by the help of **Figure 9a**, too. They were accounted for the fitting model by introducing a component with well-defined hyperfine magnetic fields. The obtained temperature dependences are shown in **Figure 9b**. Hyperfine fields corresponding to nanocrystalline grains are compared with those of a polycrystalline bcc-Fe foil. The former exhibit systematically lower values which are caused by small amounts as well as dimensions of quenched-in nanocrystals.

At certain temperature of annealing, additional nanocrystalline grains appear, and all grains begin to grow both in number and in size. This rather abrupt onset of bulk nanocrystallization is clearly seen by a step-like increase in the hyperfine magnetic field value at ~400 °C during annealing in zero-field conditions. Under the influence of external magnetic field, this increase is rather continuous but starts at ~300 °C, that is, much earlier. For T>400 °C, both curves merge together and follow the temperature dependence of hyperfine magnetic fields that correspond to bulk bcc-Fe with almost constant difference of ~2 T. Lower hyperfine magnetic field values are due to small dimensions of the nanocrystals.

It is noteworthy that the decrease of hyperfine magnetic field with temperature as observed in **Figure 9**b is also demonstrated in **Figure 8** by shift of the maxima of time-domain patterns towards higher delayed times. With rising temperature, the magnetic ordering continuously vanishes and eventually disappears at the Curie point.

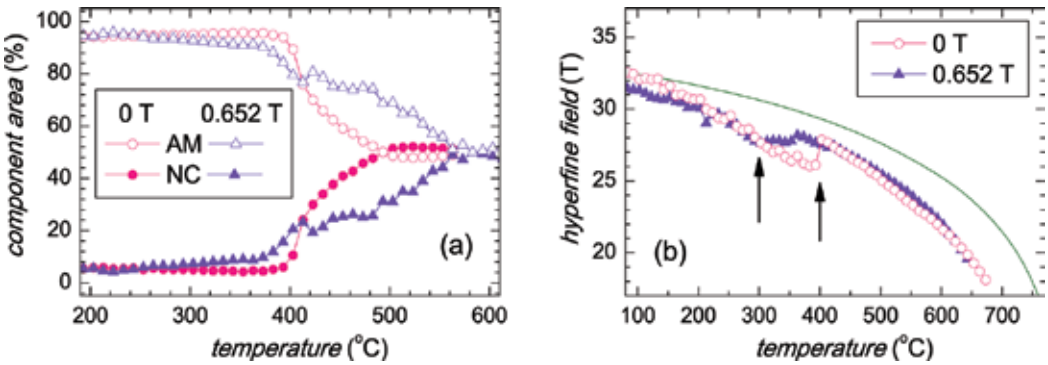

Figure 9. Relative amounts of amorphous (AM) (open symbols) and total nanocrystalline (NC=CR+IF) (solid symbols) components (a) and hyperfine magnetic fields of nanocrystals (b) plotted against temperature of annealing as obtained from NFS time-domain patterns of the $Fe_{81}Mo_8Cu_1B_{10}$. MG measured in zero magnetic field (circles) and in the field of 0.652 T (triangles). Values corresponding to bulk bcc-Fe (green curve) are given for comparison. The arrows indicate T_{x1}.

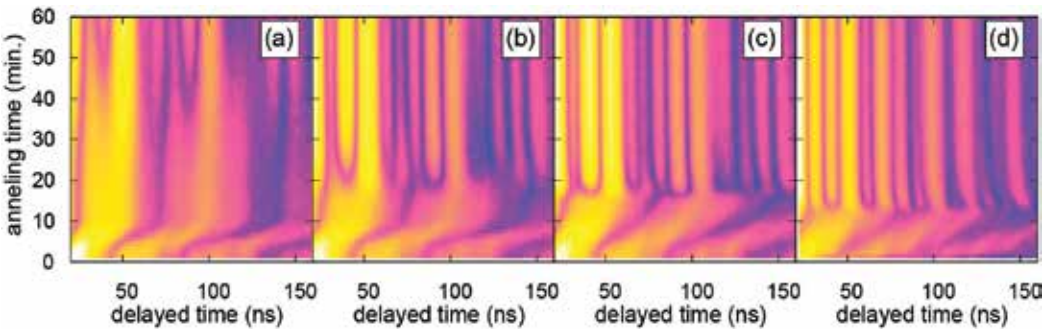

Figure 10. Contour plots of isothermal NFS time-domain patterns of the $Fe_{90}Zr_7B_3$ MG annealed at 470 °C (a), 480 °C (b), 510 °C (c), and at 480 °C under external magnetic field of 0.652 T (d).

In this section, we have demonstrated how NFS experiments can contribute to more detail description of structural as well as magnetic transformations that are taking place in real time upon MGs exposed to dynamically changing temperature. In particular, in situ studies of hyperfine interactions cannot be performed by any other analytical tool. Thus, a possibility to follow separately temperature evolution of individual structural components viz. AM, CR, and IF makes NFS an interesting and competitive method for the investigation of nanocrystallization in MGs *during* its progress. In the following section, other aspects of this technique are presented with a special focus at time-dependent experiments.

5.3. Isothermal experiments

In the above section, we have concentrated on a dynamics of nanocrystallization. For that purpose, a continuous increase of temperature with a constant ramp was ensured. Acquisition of NFS data was accomplished in situ during ongoing progress of temperature. Thus, the investigated system was exposed to change annealing conditions. Here, we focus at the kinetics of crystallization. The studies were performed at constant annealing conditions. In this way, information on various parameters of the crystallization kinetics can be acquired.

NFS experiments were performed on $Fe_{90}Zr_7B_3$ MG prepared by melt spinning technique in a form of thin ribbons. After initial rapid increase of temperature with a ramp of 40 K/min, the annealing temperature was stabilized at its destination value. NFS data were recorded *in situ* with an acquisition time of 1 min. Duration of the experiments was up to 150 min. The annealing temperatures of 470, 480, and 510 °C were chosen. Isothermal experiment at 480 °C was performed also in an external magnetic field of 0.652 T.

Contour plots of NFS time-domain patterns from all experiments are shown in **Figure 10**. Time of annealing under the set conditions is given on the y-axes. The originally as-quenched sample is paramagnetic at room temperature and exhibits quantum beats typical for electric quadrupole interactions (see **Figure 1d**). Depending upon the annealing conditions, newly formed ferromagnetic nanocrystalline grains of bcc-Fe emerge from the amorphous matrix within 10–30 min after reaching the annealing temperature. They are identified through magnetic dipole interactions that give rise to hyperfine magnetic fields. The latter exhibit well-developed high-frequency oscillations in quantum beats similar as those in **Figure 1f**. They

http://dx.doi.org/10.5772/66869

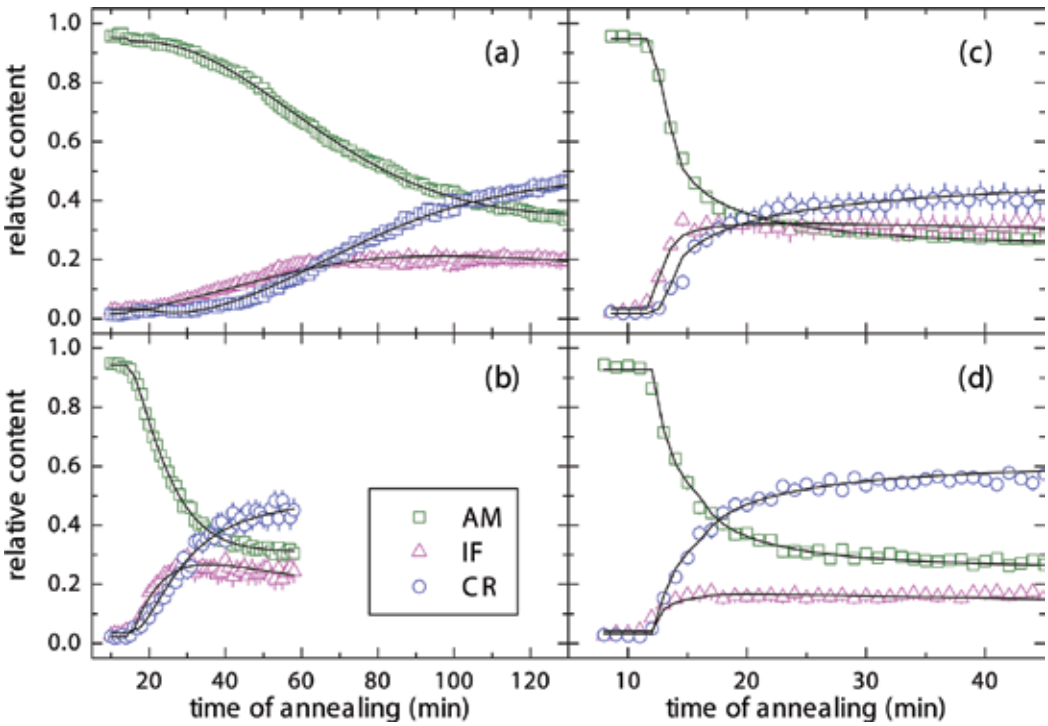

Figure 11. Relative amounts of structural components including amorphous matrix (AM, green squares), crystalline grains (CR, blue circles), and interface regions (IF, magenta triangles) plotted against time of annealing at 470 °C (a), 480 °C (b), 510 °C (c), and at 480 °C under external magnetic field of 0.652 T (d). Solid curves represent fits according to the crystallization model introduced in Ref. [18].

persist over the entire time of the experiments. Because the temperature of annealing does not change, the positions of individual beat maxima are also stable.

Time evolution of individual structural components viz. AM, CR, and IF is presented in **Figure 11**. Relative areas obtained from evaluation of NFS time-domain patterns are displayed by symbols. Subsequently, they were fitted using a crystallization model introduced recently [18]. The resulting theoretical curves are plotted by solid lines. The following observations can be noted. First, as demonstrated by the IF and CR relative contents in **Figure 11a a**nd **b**, the IF component dominates that of the CR one during the first 65 and 30 min of annealing, respectively. This indicates that the grains are rather small and thus exhibit higher contribution of the atoms located at their surfaces. Later, the grains grow in size which is documented by a higher fraction of CR than IF. The latter saturate with time which means that the grains do not grow any further, and only their number increases.

Secondly, increase in temperature of annealing from 470 to 480 °C accelerates formation of nanograins. In order to achieve ~60 % of nanograins, three times shorter time is needed for annealing temperature of 480 °C in comparison with 470 °C. Note different scales on the x-axes. Further temperature increase from 480 to 510 °C expectedly speeded-up the crystallization rate as seen in **Figure 11c**. The same effect is reached, however, by annealing at the

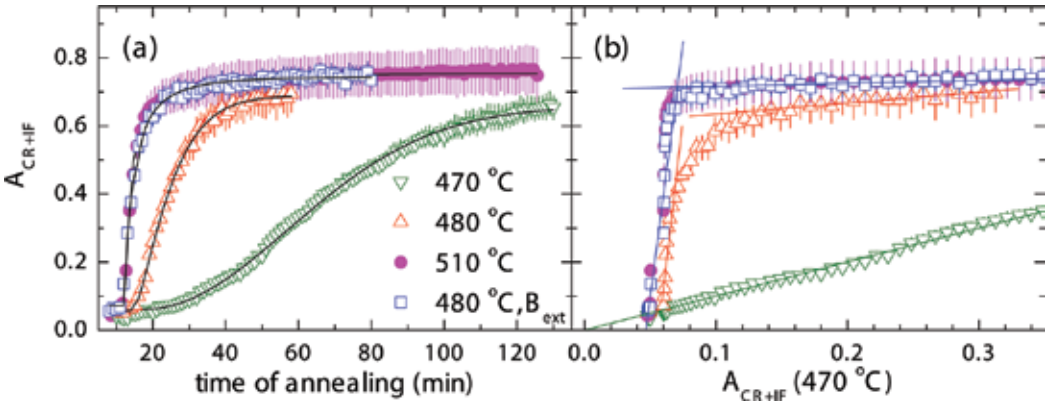

Figure 12. Relative amount of nanograins A_{CR+IF} plotted against time of annealing (a) and relative content of nanograins obtained at 470 °C (b). Black solid curves in (a) represent fit according to the crystallization model introduced in Ref. [18].

lower temperature of 480 °C in external magnetic field of 0.652 T as demonstrated in **Figure 11d**. The time needed for crystallization is by a factor of ~3 less than that without the external magnetic field at the same temperature of annealing.

Relative content of nanocrystals given as a sum of the corresponding crystalline (CR) and interface (IF) components A_{CR+IF} is depicted in **Figure 12**. Formation of nanograins under different annealing conditions is mutually compared in **Figure 12a** with respect to the annealing time. As discussed above, small increase in the annealing temperature from 470 to 480 °C, that is, only by 10 °C causes notable increase in the amount of nanograins that are formed during the same time period. This is due to proximity of the first crystallization temperature. When the annealing temperature is elevated further to 510 °C (i.e., by 30 °C), the change in the character of the A_{CR+IF} dependence is not so dramatic. We stress again, that almost the same contents of nanograins is obtained when annealing at 480 °C proceeds under weak magnetic field. Presumably, this is caused by huge influence of small energetic perturbations of magnetic interactions in comparison with the thermal energy.

Figure 12a shows absolute values of the nanocrystalline content, and as it is more closely discussed elsewhere [19], all processes behave identically from a qualitative point of view. Dramatic differences among them are revealed, however, by the help of **Figure 12b**. Here, the total amount of nanograins A_{CR+IF} is plotted against this parameter obtained from the slowest isothermal experiment performed at 470 °C. Consequently, the experimentally acquired data are distributed along a straight line with the slope equal 1. Dramatic changes in the slopes are observed during annealing at 480, 510, and 480 °C in external magnetic field. The associated rates of nanocrystallization are by a factor of ~30 higher that at 470 °C. They are indicated in **Figure 12b** by straight almost vertical lines. In order to visualize these rapid processes more clearly, the x-axis is reduced to the equivalent of the first ~65 min of the isothermal experiments.

After the initial rapid onset of nanocrystals formation, further increase in A_{CR+IF} is not so steep. In fact, it almost saturates with the slope of 0.1 for annealing at 510 °C and at 480 °C

http://dx.doi.org/10.5772/66869

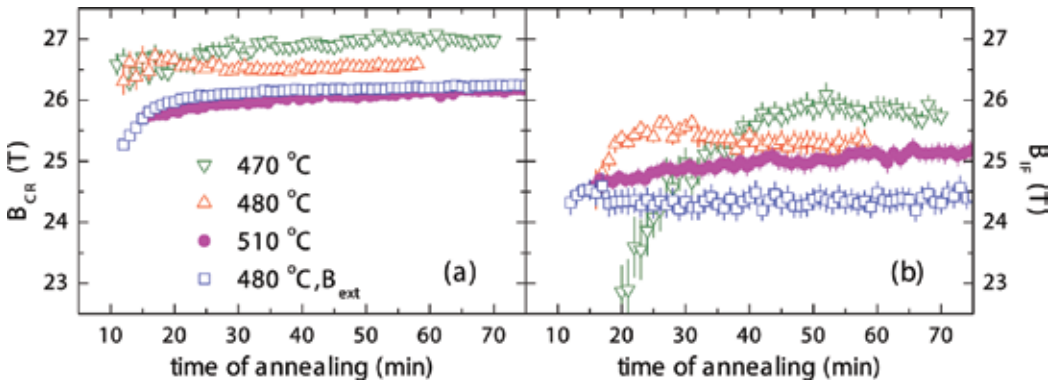

Figure 13. Hyperfine magnetic field of the CR (a) and IF (b) components plotted against time of annealing.

in B_{ext} = 0.652 T. In zero-field annealing at 480 °C, it exhibits only gentle increase towards the same saturation value showing slightly higher slope of 0.32.

Hyperfine magnetic fields obtained from the CR and IF components are depicted in **Figure 13** as a function of annealing time. Depending upon the temperature of annealing, B_{CR} saturates at different values as seen in **Figure 13a**. They are by about 1.5 T smaller than those of polycrystalline bcc-Fe [38] due to nanosized dimensions of the grains. Decrease in B_{CR} at the beginning of annealing especially at 480 °C in B_{ext} indicates that the inner structure of bcc nanograins is still not very well developed during early stages of crystallization. Similar phenomenon is observed in **Figure 13b** where hyperfine magnetic fields of the interface components B_{IF} are presented.

Small dimensions of nanocrystalline grains are also responsible for remarkable time evolution of B_{IF} especially during annealing at 470 °C and to a smaller extent at 480 °C. At the beginning of grain growth, majority of the constituent Fe atoms is located at the surfaces of the nanocrystals. As a result, relative content of the IF component prevails that of the CR one as demonstrated in **Figure 11a** and **b.** Simultaneously, because of symmetry breaking in the interfacial regions, the associated hyperfine magnetic fields exhibit smaller values than the inner parts of the grains.

In this section, we have demonstrated how NFS can be used for the investigations of the kinetics of crystallization. Isothermal experiments performed under different annealing conditions, viz. temperature and presence of external magnetic field provide valuable information on the time evolution of both the content of nanocrystals and on their hyperfine magnetic fields. Moreover, these phenomena can be studied separately for structurally different regions that are found in NCAs.

6. Conclusions

Nanocrystallization of metallic glasses was followed by in situ experiments of nuclear forward scattering (NFS) of synchrotron radiation to fine details that are completely hidden when conventional analytical tools are employed. Detailed analyses of NFS time-domain patterns that were decomposed into contributions stemming from the amorphous residual phase and newly

formed nanocrystallites provided an opportunity to study independently the role of structurally different regions. Moreover, using this approach, it was possible to further differentiate between contributions from the surfaces and the inner parts of nanograins. Different amounts of iron atoms located at the grains' surfaces and in their bulk were observed when different crystallization conditions, viz. temperature and/or external magnetic field, were applied.

The application of in situ NFS experiments has a huge potential for observations of the evolution of phase transformations in real time performed on fly during short time intervals. This was documented by two types of in situ NFS experiments. Namely, dynamical temperature increase and isothermal annealing under constant conditions were applied. It was possible to follow not only structural transformations, but, at the same time, also changes in magnetic arrangement were revealed. The latter is feasible owing to rapid screening of the corresponding hyperfine interactions. In this way, detail information about the nearest neighbourhoods of the resonant atoms is experimentally achievable. Moreover, the local arrangements can be checked in real time thus enabling structural and/or magnetic transformation to be followed on fly. In addition, a possibility of comparing the experimental results with those obtained from simulations and/or theoretical calculations is offered. Such experiments are unique and open new horizons in materials research by employing the technique of nuclear forward scattering of synchrotron radiation.

Acknowledgements

We are grateful to R. Rüffer (Grenoble) and S. Stankov (Karlsruhe) for stimulating discussions. Samples of metallic glasses were provided by a courtesy of D. Janičkovič (Bratislava). The authors would like to thank P. Švec (Bratislava), J. Kohout (Prague), and A. Lančok (Husinec-Řež) for their technical assistance during measurements on the synchrotron and V. Vrba (Olomouc) for his help with data processing. Financial support of the grants GAČR 14-12449S, IGA_PrF_2016_022, and VEGA 1/0182/16 is acknowledged.

Author details

Marcel B. Miglierini[1,2]* and Vít Procházka[3]

*Address all correspondence to: marcel.miglierini@stuba.sk

1 Slovak University of Technology in Bratislava, Faculty of Electrical Engineering and Information Technology, Institute of Nuclear and Physical Engineering, Bratislava, Slovakia

2 Department of Nuclear Reactors, Faculty of Nuclear Science and Physical Engineering, Czech Technical University in Prague, Prague, Czech Republic

3 Department of Experimental Physics, Faculty of Science, Palacky University, Olomouc, Czech Republic

References

[1] Herzer G. Modern soft magnets: Amorphous and nanocrystalline materials. Acta Mater. 2013;**61**,718–734. doi:10.1016/j.actamat.2012.10.040

[2] McHenry ME, Willard MA, Laughlin DE. Amorphous and nanocrystalline materials for applications as soft magnets. Prog Mater Sci. 1999;**44**,291–443. doi:10.1016/S0079-6425(99)00002-X

[3] McHenry ME, Laughlin DE. Nano-scale materials development for future magnetic applications. Acta Mater. 2000;**48**,223–238. doi:10.1016/S1359-6454(99)00296-7

[4] Gutfleisch O, Willard MA, Bruck E, Chen CH, Sankar S, Liu JP. Magnetic materials and devices for the 21st century: stronger, lighter, and more energy efficient. Adv Mater. 2011;**23**,821–842. doi:10.1002/adma.201002180

[5] Hernando A. Magnetic properties and spin disorder in nanocrystalline materials. J Phys: Condens Matter. 1999;**11**,9455–9482. doi:10.1088/0953-8984/11/48/308

[6] Inoue A, Takeuchi A. Recent development and application products of bulk glassy alloys. Acta Mater. 2011;**59**,2243–2267. doi:10.1016/j.actamat.2010.11.027

[7] Miglierini M, Kopcewicz M, Idzikowski B, Horváth ZE, Grabias A, Škorvánek I, Dluzewski P, Daróczi CsC. Structure, hyperfine interactions and magnetic behavior of amorphous and nanocrystalline $Fe_{80}M_7B_{12}Cu_1$ (M = Mo, Nb, Ti) alloys. J Appl Phys. 1999;**85**,1014–1025. doi:10.1063/1.369223

[8] Pavuk M, Miglierini M, Vujtek M, Mashlan M, Zboril R, Jiraskova Y. AFM and Mössbauer spectrometry investigation of the nanocrystallization process in Fe-Mo-Cu-B rapidly quenched alloy. J Phys: Condens Matter. 2007;**19**,216219. doi:10.1088/0953-8984/19/21/216219

[9] Miglierini M., Lančok A, Kohout J. Hyperfine fields in nanocrystalline Fe-Zr-B probed by 57Fe nuclear magnetic resonance spectroscopy. J Appl Phys Lett. 2010;**96**,211902. doi:10.1063/1.3431612

[10] Pradeep KG, Herzer G, Choi P, Raabe D. Atom probe tomography study of ultrahigh nanocrystallization rates in FeSiNbBCu soft magnetic amorphous alloys on rapid annealing. Acta Mater. 2014;**68**,295–309. doi:10.1016/j.actamat.2014.01.031

[11] Mattern N, Stoica M, Vaughan G, Eckert J. Thermal behaviour of $Pd_{40}Cu_{30}Ni_{10}P_{20}$ bulk metallic glass. Acta Mater. 2012;**60**,517–534. doi:10.1016/j.actamat.2011.10.032

[12] Wang G, Mattern N, Bednarčík J, Li R, Zhang B, Eckert J. Correlation between elastic structural behavior and yield strength of metallic glasses. Acta Mater. 2012;**60**,3074–3084. doi:10.1016/j.actamat.2012.02.012

[13] Egami T, Tong Y, Dmowski W. Deformation in metallic glasses studied by synchrotron X-ray diffraction. Metals. 2016;**6**,22.doi:10.3390/met6010022

[14] Puncreobutr C, Phillion AB, Fife JL, Rockett P, Horsfield AP, Lee PD. In situ quantification of the nucleation and growth of Fe-rich intermetallics during Al alloy solidification. Acta Mater. 2014;**79**,292–303. doi:10.1016/j.actamat.2014.07.018

[15] Giordano VM, Ruta B. Unveiling the structural arrangements responsible for the atomic dynamics in metallic glasses during physical aging. Nat Commun. 2016;**7**,10344. doi:10.1038/ncomms10344

[16] Miglierini M, Greneche J-M. Mössbauer spectrometry of Fe(Cu)MB-type nanocrystalline alloys: II. The topography of hyperfine interactions in Fe(Cu)ZrB alloys. J Phys: Condens Matter. 1997;**9**,2321–2347. doi:10.1088/0953-8984/9/10/018

[17] Smirnov GV. General properties of nuclear resonant scattering. Hyperfine Int. 1999;**123/124**,31–77. doi:10.1023/A:1017007520099

[18] Miglierini M, Prochazka V, Stankov S, Svec Sr. P, Zajac M, Kohout J, Lancok A, Janickovic D, Svec P. Crystallization kinetics of nanocrystalline alloys revealed by in-situ nuclear forward scattering of synchrotron radiation. Phys Rev B. 2012;**86**,020202(R). doi:10.1103/PhysRevB.86.020202

[19] Miglierini M, Procházka V, Rüffer R, Zbořil R. In situ crystallization of metallic glasses during magnetic annealing. Acta Mater. 2015;**91**,50–56. doi:10.1016/j.actamat.2015.03.012

[20] Procházka V, Vrba V, Smrčka D, Rüffer R, Matúš P, Mašláň M, Miglierini M. Structural transformation of NANOPERM-type metallic glasses followed in situ by synchrotron radiation during thermal annealing in external magnetic field. J Alloy Compds. 2015;**638**,398–404. doi:10.1016/j.jallcom.2015.03.058

[21] Miglierini M, Pavlovič M, Procházka V, Hatala T, Schumacher G, Rüffer R. Evolution of structure and local magnetic fields during crystallization of HITPERM glassy alloys studied by in situ diffraction and nuclear forward scattering of synchrotron radiation. Phys Chem Chem Phys. 2015;**17**,28239–28249. doi:10.1039/C5CP00245A

[22] Machala L, Procházka V, Miglierini M, Sharma VK, Marušák Z, Wille HCh, Zbořil R. Direct evidence of Fe(V) and Fe(IV) intermediates during reduction of Fe(VI) to Fe(III): a nuclear forward scattering of synchrotron radiation approach. Phys Chem Chem Phys. 2015;**17**,21787–21790. doi:10.1039/c5cp03784k

[23] Stankov S, Yue YZ, Miglierini M, Sepiol B, Sergueev I, Chumakov AI, Hu L, Švec P, Rüffer R. Vibrational properties of nanograins and interfaces in nanocrystalline materials. Phys Rev Lett. 2008;**100**,235503. doi:10.1103/PhysRevLett.100.235503

[24] Stankov S, Miglierini M, Chumakov AI, Sergueev I, Yue YZ, Sepiol B, Svec P, Hu L, Rüffer R. Vibrational thermodynamics of NANOPERM nanocrystalline alloy from nuclear inelastic scattering. Phys Rev B. 2010;**82**,144301. doi:10.1103/PhysRevB.82.144301

[25] Röhlsberger R. Nuclear Condensed Matter Physics with Synchrotron Radiation. Berlin Heidelberg: Springer-Verlag; 2004. 318 p. doi:10.1007/b86125

[26] Seto M. Condensed matter physics using nuclear resonant scattering. J Phys Soc Jpn. 2013;**82**,021016. doi:10.7566/JPSJ.82.021016

[27] Gütlich Ph, Bill E, Trautwein AX. Mössbauer Spectroscopy and Transition Metal Chemistry. Heilderberg Dordrecht London New York: Springer; 2011. 568 p. doi:10.1007/978-3-540-88428-6

[28] Rüffer R. Nuclear resonance scattering. CR Physique. 2008;**9**,595–607. doi:10.1016/j.crhy.2007.06.003

[29] Sturhahn W, Gerdau E. Evaluation of time-differential measurements of nuclear-resonance scattering of x rays. Phys Rev B. 1994;**49**,9285–9294. doi:10.1103/PhysRevB.49.9285

[30] Sturhahn W. CONUSS and PHOENIX: Evaluation of nuclear resonant scattering data. Hyperfine Interact. 2000;**125**,149–172. doi:10.1023/A:1012681503686

[31] Hubert software package [Internet]. 2015. Available from: http://fyzika.upol.cz/cs/vysledky-vyzkumu/software-hubert [Accessed: 2016-08-18].

[32] Vrba V, Procházka V, Smrčka D, Miglierini M. Hubert: Software for efficient analysis of in-situ nuclear forward scattering experiments. In: AIP Conference Proceedings **1781**, 020013 (2016); doi:10.1063/1.4966009

[33] Miglierini M, Greneche J-M. Mössbauer spectrometry of Fe(Cu)MB-type nanocrystalline alloys: I. The fitting model for the Mössbauer spectra. J Phys: Condens Matter. 1997;**9**,2303–2319. doi:10.1088/0953-8984/9/10/017

[34] Shvyd'ko YV, van Burck U. Hybrid forms of beat phenomena in nuclear forward scattering of synchrotron radiation. Hyperfine Int. 1999;**123**,511–527. doi:10.1023/A:1017084209621

[35] Miglierini M, Hatala T, Frydrych J, Šafářová K. Surface crystallization of Co-containing NANOPERM-type alloys. Hyperfine Int. 2012;**205**,125–128. doi:10.1007/s10751-011-0495-1

[36] Škorvánek I, Marcin J, Turcanová J, Kovác J, Švec P. Improvement of soft magnetic properties in $Fe_{38}Co_{38}Mo_8B_{15}Cu$ amorphous and nanocrystalline alloys by heat treatment in external magnetic field. J Alloys Compd. 2010;**504**,S135–S138. doi:10.1016/j.jallcom.2010.04.033

[37] Miglierini M, Hatala T, Bujdoš M. Depth-selective study of surface crystallization in NANOPERM-type alloys. Acta Phys Pol A. 2014;**126**,56–57. doi:10.12693/APhysPolA.126.56

[38] Preston RS, Hanna SS, Heberle J. Mössbauer effect in metallic iron. Phys Rev B. 1962;**128**,2207–2218. doi:10.1103/PhysRev.128.2207

Chapter 3

Operando Structural Characterization of the E-ALD Process Ultra-Thin Films Growth

Andrea Giaccherini, Roberto Felici and
Massimo Innocenti

Additional information is available at the end of the chapter

http://dx.doi.org/10.5772/67355

Abstract

Spanning from nanoelectronics to new solar energy materials, technological development in the recent years requested highly controlled nanostructured surfaces, ultra-thin films, and 2D structured materials. In general, although very favorable from a full life cycle assessment (FLCA) standpoint, electrodeposition hardly allows to obtain the high order required by recent technologies. In particular cases, the electrodeposition enables the deposition of atomic layers by means of surface limited reactions (SLRs). By exploiting SLRs, it is possible to define layer-by-layer deposition scheme of different atomic layers; we refer to these schemes as electrochemical atomic layer deposition (E-ALD) and when the growth of the film is epitaxial with the substrate, the techniques are called electrochemical atomic layer epitaxy (ECALE). Aiming at characterizing structure and growth of materials grown by means of E-ALD, surface analysis techniques apply better. In particular, surface X-ray diffraction (SXRD) with high brilliance synchrotron sources enables the operando structural analysis in electrochemical environment. In recent years, several works on the operando surface characterization by means of SXRD have been reported. Thanks to novelties in the field of operando SXRD experiments, semiconducting systems were studied, such as single and multilayer of CdS and Cu_2S.

Keywords: ECALE, E-ALD, thin films, 2D materials, SXRD

1. Introduction

A fundamental aim of material research and surface science is the development of deposition techniques of compound semiconductors with low impact from either the energetic or environmental points of view. These techniques should ensure a high structural control for the

engineering of nanostructures such as quantum dots, quantum well, superlattices, and thin films still preserving the crystalline properties of the grown material. The bottom-up approach is renowned as very favorable for the synthesis of such materials in the form of dispersed nanoparticles from molecular precursor, usually involving several steps and the addition of surfactants to the reaction environment. Since most of these products, obtained following these pathways, are in form of powders, the production of solid-state devices requires several steps for the deposition of the materials. In this context, electrodeposition has the advantage of the direct production of the films from the molecular precursors. In any case, electrodeposition hardly results in highly ordered materials as requested by recent technologies based on semiconductor. However, in specific conditions, electrodeposition enables the assemblage of atomic layers by means of surface limited reactions (SLRs). SLRs give the opportunity of exploiting layer-by-layer deposition of different atomic layers, leading to one of the most clean and energy saving approaches, electrochemical atomic layer epitaxy (ECALE) [1], for the growth of heterostructures. ECALE could be also referred in general as electrochemical atomic layer deposition (E-ALD) since in some cases the growth, though based on under potential deposition (UPD) processes or on any SLR, cannot be rigorously considered epitaxial. Hence, E-ALD joins highly ordered products with the direct access to the final material in the context of the bottom-up approach in a very clean reaction environment. E-ALD has been proven to be very effective for the electrodeposition of ultra-thin films of semiconducting materials. In recent years, thin films of binary [2–5] and ternary semiconductors [6–9] were successfully obtained. E-ALD requires very low energy consumption, diluted solutions, room temperature, and atmospheric pressures. Thus, it can be employed for the sustainable large-scale production of these materials. This is particularly interesting for photovoltaics application, where the improvements of the full life cycle assessment (FLCA) are considered a crucial aspect for the possible large-scale production of new materials [10]. In this context, it is very crucial to study and understand the growth mechanism together with the detailed analysis of the structural features of the resulting thin films. For this purpose, surface analysis techniques play an important role. Among them, surface X-ray diffraction (SXRD), with high brilliance synchrotron sources, enables the operando structural analysis in electrochemical environment during the E-ALD growth and discloses the structural features of such systems during the deposition process. In recent years, several works on the operando characterization of ultra-thin films have been reported thanks to the development of specifically designed flow cells and automated apparatus to perform 100 or more growth cycles in few hours.

2. E-ALD for semiconducting materials

Materials overcoming the properties of silicon-based semiconducting materials are very widely researched. In particular, the interest is devoted toward materials with optoelectronic and electronic properties, in a broad range, able also to work in severe conditions. In this context, compound semiconductors are promising candidates. They result from the combination of two or more elements. The ones formed by elements of the groups symmetrical to the IV group, namely the III–V compound semiconductors are among the most studied. Epitaxy is

http://dx.doi.org/10.5772/67355

generally expected to enhance their semiconducting proprieties, such as mean free path and charge carrier mobility. Moreover, epitaxial growth is necessary to obtain superlattices, i.e., materials with a periodic modulation of structure or composition and crystallographic coherence with respect to the atomic planes [11]. For example, without the crystallographic coherence, a bilayer ZnSe/CdSe film or a sequence of multiple layers of ZnSe, CdSe is not called a superlattice, but simply a heterojunction or a multilayer system. In this field, superlattices are of increasing interest, since it is possible to tailor their properties even at the nanoscale, where they are exhibiting quantization effects. The growth of perfectly flat, ultrathin, and even 2D sheets of material is a stringent requirement for the functionality of multilayers or superlattices. E-ALD provides a sustainable solution got the growth of high-quality 2D materials with well-controlled periodicities.

E-ALD constitutes an easy way to deposit suitable ultrathin films and 2D materials alternating atomic layer of different elements in a very straightforward manner. For these reasons, since its infancy, the E-ALD study has been carried on compound semiconductors, with a specific focus on compound semiconductors based on elements of the II–VI groups. **Figure 1** depicts a general scheme for the E-ALD of a ternary chalcogenide, this can be obtained by alternating SLR steps of metals (M1, M2) and chalcogenides (C).

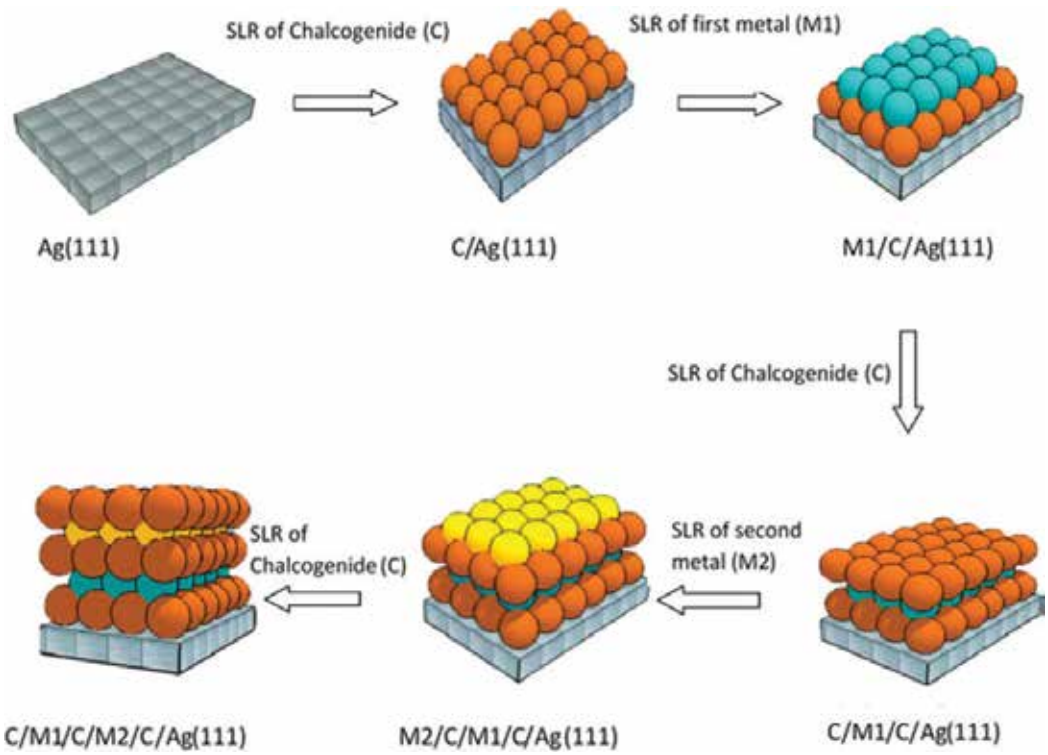

Figure 1. General scheme for an E-ALD process aimed to grow a ternary chalcogenide. C, M1 and M2, respectively, stand for an atomic layer of chalcogenide, first metal in the scheme and second metal in the scheme.

In order to tailor the stoichiometry of the compounds, it is possible to define schemes with different number of steps for the two metals, as will be discussed in Section 2.2.2 for Cu_xZn_yS. The E-ALD procedure requires a thorough knowledge of the separated SLRs (often UPD—under potential deposition) involved in the deposition of the metals over the nonmetals and vice versa. An open issue is the exact definition of the driving force leading these processes. It is very widely accepted that the main contribution to the driving force is the negative free energies change involved in the interaction with the electrodic surface and in the formation of a thermodynamically stable compound. However, the surface can change during the growth due to formation of the crystal, and it is possible to think of a change also in the driving force when a relatively thick crystal is grown. As reported by almost every paper on this topic, it is worth to notice that, usually, the first step of the E-ALD process is the deposition of an atomic layer of chalcogen (or of the nonmetal in general) over the bare metal substrate. Reasonably, the experimental conditions for the deposition change while increasing the thickness of the deposit. For instance, in the growth of crystals, the accumulation of the elastic energy into the lattice is a nonfavorable contribution to the driving force. This is a well-known issue leading to different growth mechanisms and related morphology. Usually, in the case of the E-ALD process, these effects do not prevent the compound formation. Generally speaking, the changes are in the sense of decreasing the amount of deposition and then the total time of the process increases. This can prevent the deposition of some materials, as CdTe and InAs, with a thickness of practical relevance. In other cases (such as the deposition of Cu_2S), the deposition of the copper layer, implying the reduction of copper ions from the solution, may result in more complex reactions implying the formation of some intermediate compounds and the deposition cannot be accounted strictly by the UPD process. Several experimental evidences for these controversial aspects have been reported and they will be discussed in the following pages. It is worth to notice that they reveal a complex mechanism for the formation of chalcogenides by means of E-ALD. The complexity of these processes occurring during the growth is the reason why we prefer to refer to the E-ALD steps with the acronym SLR rather than using UPD.

In this work, we focus on the deposition of chalcogenides on a Ag single crystal, usually on the Ag(111) surface if not specifically indicated. All the potentials repoeted here are referred to the Ag/AgCl(KCl sat.) reference electrode.

2.1. Cadmium-based compound semiconductors

Cadmium chalcogenides have been among the first compound semiconductors to be deposited by means of E-ALD due to their interesting electronic properties and favorable electrochemical characteristics.

2.1.1. CdS

One of the first chalcogenides electrodeposited by E-ALD is the CdS, extensively studied on several different single crystals. The E-ALD process for CdS on Ag(111) has been verified to be epitaxial and does not require the formation of any intermediate compounds [12, 13]. Its deposition can be considered a genuine ECALE process. It starts with the oxidative UPD of the sulfur ions on the metal surface. It is worth mentioning that the structure of the resulting

sulfur layer has been deeply studied by means of scanning tunneling microscopy (STM) measurements. The second step of the ECALE process is the UPD deposition of cadmium on top of the Ag(111)/S. The charge associated with each layer of either Cd or S corresponds to 0.165 monolayers (referred to as the ideal covering of a layer of the Ag(111) substrate). STM measurements confirm that the fractional coverage of the Cd and S cycles on top of the Ag(111)/S from the 3/7 of the first S layer to the 1/7 (consistent with the coulomb-metric measurement). The epitaxial growth is actually confirmed by the STM images of the first four atomic layers, whereas the unit value of the S/Cd ratio for the successive layers strongly suggests that the epitaxial growth is maintained in these further layers. Moreover, the charge deposited was verified to be linear with the number of ECALE cycles [2] for ECALE scheme as long as 50 cycles. Thus, the results are consistent with the layer-by-layer mechanism proposed for the ECALE process. CdS shows a discrepancy between the deposition on Au(111) and Ag(111). Shannon and Demir reported a (333) structure with a Cd–Cd distance of 4.3 Å for the Cd layer on top of the S layer deposited on Au(111) [14]. This structure is much more compact than the one obtained by our group (0.76 nm for both Cd–Cd and S–S distances) and that difference cannot be ascribed to a difference in lattice constants of Ag and Au since they are practically identical. We proposed that the difference could be ascribed to the different structure of the S layer in contact with the metallic substrate. In fact, the S layer on Au(111) forms a structure with a coverage of one-third, while in the experimental condition we defined on Ag(111) forms a site occupied by a triplet of sulfur atom (coverage of 3/7) and is therefore much more compressed. Thus, Ag denotes a higher affinity with S, resulting in a CdS structure, as determined by STM, corresponding to the basal planes of both wurtzite and zinc blende; these two structures are very similar on the basal plane, and it is not possible to distinguish them by means of STM studies of the first E-ALD cycles. SXRD experiment clarified the structure of CdS and showed that high crystalline quality of the CdS films grown on different surfaces [12, 13]. On the Ag(111), the growth films present only the hexagonal wurtzite structure, while on the other low index planes, a mixture of the hexagonal wurtzite and cubic zinc-blende phases is present.

2.1.2. Other Cd-based chalcogenides

It has been shown that a one-step oxidative SLR is not possible for selenides and tellurides. The E-ALD process for CdSe involves the same steps of the CdS, but the experimental conditions are very different [15]. Hence, the deposition of the Se layer is usually obtained by means of a two-step process [15]. The first implying a massive deposition of a Se film on the Ag(111) followed by reduction of all but the adlayer of Se on the Ag(111) surface. A 1:1.3 (Cd:Se) growth on Ag(111) has been achieved, a tentative explanation is that the transition to a less compact Se structure can occur during the stripping of the bulk Se. The peak related to the transition is probably overlapping with the bulk Se reduction peak. Hence, a lower than expected covering of the substrate is achieved, and consequently, a Cd:Se ratio higher than 1.. Regarding CdTe, cyclic voltammetry showed two peaks related to the reductive UPD of the $HTeO_2^+$ on Au(111), and they occur at potential too positive to be easily observed on Ag(111) due to its narrower electrochemical stability window. They are related to a complex chemistry well explained in the literature [16]; hence, it is necessary to use a scheme similar to the CdSe

growth. The charge deposited for the first Te layer on Ag(111) is equal to that found on the first UPD of Te on Au(111), for which a (12 × 12) structure was revealed by STM images as well as by low-energy electron diffraction (LEED) patterns. LEED measurements after emersion at a potential corresponding to the second UPD of Te also showed that the (12 × 12) structure originated from a (3 × 3) structure [17]. The structure formed in correspondence with the sole UPD of Te observed on Ag(111) is expected to have the same structure [18]. However, no morphological or structural analysis has been performed on such substrate in order to confirm the expectation. Eventually, E-ALD also gives the possibility of growing ternary and quaternary compounds, and here we describe the case of ternary chalcogenides $Cd_xZn_{1-x}S$ and $Cd_xZn_{1-x}Se$ grown on Ag(111) [19–21]. The stoichiometry of the ternary chalcogenides grown by E-ALD can be controlled by the ZnX/CdX (X = S, Se) ratio. Still, CdX deposition seems to be favored with respect to ZnX deposition, hence the ratio between Cd and Zn cycles in the E-ALD sequence does not correspond to the stoichiometric ratio of Cd and Zn in the ternary compounds. Zn-deficiency is a general trend in ternary compounds deposited by means of E-ALD. The authors reported that the most likely explanation for the experiments is a lower deposition rate for Zn. However, electrochemical and XPS characterization confirmed the layer-by-layer growth and the 1:1 ratio between metals and sulfide ions. Eventually, the thickness seems to decrease while decreasing the Cd content. Analogous behavior, although referred to films as thick as 1–5 μm, was found for the compounds grown by the dip technique [22].

2.1.3. An overview on thermodynamics and lattice mismatches

The potential shifts exploited by the SLR involved in the E-ALD steps are related to the driving force of the process. As discussed in the first part of this text, the definition of the driving force is an open question for the E-ALD, and we can divide it in three terms:

1. The interaction with the surface.
2. The formation of a compound (ΔE_f related to the free energy of formation).
3. The cumulative elastic energy (ΔE_{mis}).

The first term probably dominates the first stages of the growth, while for films with a thickness of several E-ALD cycles the second and third terms become predominant. Experimental results on similar electrodeposition process reported by Golan showed that the growth of such thin films can be either stopped [23, 24] or develop overgrowing quantum dots due to their cumulative strain. Hence, for a qualitative analysis on thin films of practical interest, we consider the potential shift related to the following energy term:

$$\Delta E = \Delta E_f + \Delta E_{mis} \tag{1}$$

where ΔE_f is the chemical energy related to the formation of the CdX compound, ΔE_{mis} is the cumulative elastic energy of the overgrowth due to the mismatch with the substrate. Considering m:n supercells structure, the mismatch is the following:

$$M = \frac{n a_o - m a_s}{n a_o} \tag{2}$$

where *n* is the index of the supercell for the overgrowth, while *m* is for the substrate. As a rule of thumb, we consider larger supercells energetically less stable, even though their mismatch can be smaller. Eventually, an assessment of the cumulative elastic energy is impossible due to the lack of force constants for the hexagonal phases of the system CdX (*x* = S, Se and Te). Still, **Table 1** reports an overview of the ΔE_f and the mismatch for Ag and Au along selected orientations. Some of these structures have been experimentally verified in literature. Shannon and Demir [14] and Golan et al. [25] reported for CdS over Au(111) a 3:2 supercell with higher mismatch than the 10:7. Despite the lower mismatch of last supercell, we think this is probably related to the lower cumulative elastic energy involved in the latter due to its lower supercell index.

In principle, E-ALD of CdTe should result in a very stable compound. However, the elastic strain induced by the lattice mismatch is higher than the other two chalcogenides, unless we take into considerations very big supercell. On the other hand, CdSe seems to have very favorable chemical and elastic terms for the growth over both the substrates. Still, the experimental condition for a 1:1 growth is not easy to achieve due to the electrochemical behavior of Se. Eventually, Cd and S have a very straightforward electrochemical behavior over Ag(111). The growth of CdS on Ag(111) and Au(111) substrates is quite strained (≈4–5%) unless the substrate and compound are rotated by 30° with respect to the other. Moreover, two structures for the CdS compounds with a very similar stability are known, wurtizte-like (hexagonal—grenockite) and zincblende-like (cubic—hawleyite). Hence, the growth and structure for CdS are suitable for the characterization by SXRD. In conclusion, SXRD is a natural follow-up for the characterization of these films due to its coupled surface and bulk selectivities. In particular, CdS resulted to be an ideal system for performing operando studies of E-ALD growth.

2.2. Copper-based sulfides

Copper sulfides are considered very interesting for their particular transport and electronic proprieties. Several phases in the Cu-S compositional field have been reported to have a band gap suitable for photovoltaics. Moreover, covellite (CuS) is a natural superconductor and chalcocite (Cu_2S) is a superionic conductor. In the attempt to modulate the band gap of Cu_2S, a Zn-doped compound semiconductor (Cu_xZn_yS) has been deposited. Hence, recently, the research focused on Cu_2S and Cu_xZn_yS with some operando SXRD studies. In some cases, the epitaxial growth of thin films or 2D structure has been characterized. Revealing the peculiar structural proprieties of these materials. Moreover, these studies confirmed the advantage in using E-ALD as a production techniques for these systems in terms of growth control and quality of the resulting structure.

	$\Delta G_f°$ (KJ/mol)	M Ag(111)	M Au(111)	M Ag(111)R30°	M Au(111)R30°
CdS	−92.0	3:2 4% (10:7 −0.6%)	3:2 5% (10:7 −0.7%)	5:6 0.5%	5:6 0.3%
CdSe	−148.6	3:2 0.8%	3:2 0.6%	5:6 0.5% (6:7 0.2%)	5:6 −3% (6:7 −0.4%)
CdTe	−156.5	3:2 −5% (8:5 1%)	3:2 −5% (8:5 0.9%)	5:6 −9% (11:12 0.3%)	5:6 −9% (11:12 0.1%)

Table 1. Mismatches for Cd chalcogenides on different epitaxial relationship for Ag(111) and Au(111) substrates.

2.2.1. Copper sulfide (Cu_2S)

Copper sulfide thin films were grown on Ag(111) by means of E-ALD, hence alternating the UPD of S and Cu. A reliable assignment of the structure and stoichiometry for these semiconductor compounds is very difficult because of the variety of stable known structures in the Cu-S compositional field. Moreover, the electrochemical behavior of Cu on the Ag(111) substrate is quite complex. In fact, Cu cannot be deposited by means of UPD on Ag(111), [26], however the compound can be obtained by deposition of Cu on the S covered Ag(111) surface. Moreover, the electrochemistry of Cu(II) in ammonia buffer involves a number of interconnected reactions that must be taken into account [26]. It has been found that there are clearly predominant processes in this set of four possible reactions whose equilibrium changes according to the applied potential. It is reported that on silver Cu(II) is immediately reduced to Cu(I), and the formation of Cu(0) from Cu(I) reduction occurs at less negative potentials than that from Cu(II) [26]. Hence, experimental data reported by Innocenti et al. support the hypothesis of an SLR deposition as a result of the competitive process between these four reactions [26]. Like for CdTe and CdSe, such complex chemistry of the SLR hinders the strict assignment of the E-ALD step as an UPD process. However, even depositing Cu and S using surface-limited depositions, more complex in nature, the electrochemical and compositional analyses confirmed that we succeeded in growing multilayers of Cu_2S. Regarding the valence state of the elements in the compound, Cu(I) is present in both Cu_2S and CuS, which are the endmembers of the Cu-S compositional field. Hence, one cannot easily distinguish the two phases by means of an analysis of the binding energy as measured with XPS. In fact, Cu(I) and Cu(II) have almost coincident energy in the XPS, while both sulfide and disulfide peaks have been found in the spectra [27]. Hence, on this basis, the assessment of the stoichiometry associated with the Cu_2S cannot be safely discussed. Moreover, the short-range structural analysis carried by means of extended X-ray absorption fine structure (EXAFS) reported a first shell compatible with chalcocite structure (Cu_2S) for similar systems (Cu_xZn_yS) [28]. The electrochemical characterization also allows to establish that the same amount of compound is deposited in each deposition cycles, thus indicating the layer-by-layer growth mechanism that was the goal to achieve. Eventually, AFM analysis for 20 E-ALD is able to evidence the low roughness values of our deposits (4 Å), still higher than CdS [26].

2.2.2. Cu_xZn_yS

Although mixed Cu-Zn sulfides are supposed to be obtained as a solid solution [5], just few studies claimed to have synthesized CuZnS and (Cu, Zn)S, respectively [29, 30], without a conclusive proof. It is known that the electrodeposition of alloys and compounds allows to deposit metastable phases, thus the E-ALD approach can be a good way to grow Cu_xZn_yS films. The E-ALD process for Cu_xZn_yS follows the alternate deposition of Cu_xS and ZnS layers. The films obtained applying the general sequence Ag/S/[(Cu/S)/(Zn/S)m)]n with several different (m,n) were fully investigated by means of electrochemical characterizations. Chemical composition of the film obtained with (n,m) = (1,40) E-ALD cycles indicated a Cu/Zn ratio of about 6. Thus confirming the low contribution of Zn in ternary compound already

evidenced in the previous studies [6, 19, 31]. Eventually, Cu_xZn_yS was grown by E-ALD with a stoichiometry changing linearly with m at constant S layers (n x m); hence, the stoichiometry can be tuned by the ZnS/CuS deposition sequence. By means of extrapolation, the authors report that the 1:1 ratio can be achieved with $n = 13$ meaning a strong deficiency of Zn in the sulfides. This could be explained by a partial redissolution of zinc during the deposition of copper, which could also cause a rearrangement in the deposited materials. This is known to happen in similar methods such as the selective electrodesorption-based atomic layer deposition (SEBALD) method [32]. It is worth notice that at least two prevailing morphologies and two different crystal structures were highlighted by SEM-EDX and XAS investigations [28]. If grown alone, the Cu_2S and ZnS films reveal thin film morphology. For Cu_xZn_yS, it is reported that the occurrence of nanowires can be attributed to the lack of miscibility between the Cu and Zn sulfides [28, 33–35]. On the basis of the experimental results, E-ALD is proposed to progressively cover the Ag (111) surface with a nanometric polycrystalline film consisting of oriented microcrystals [2, 5–7, 27, 31]. However, in some case, it is possible to obtain polycrystalline phases when depositing ternary compounds or solid solutions of binary compounds that are not completely miscible [28].

2.2.3. CdS/Cu_xZn_yS

Recently, it has been reported that the first successful deposition of a CdS layer on the top of Cu_xZn_yS deposits was over a Ag(111) electrode by means of E-ALD [36]. This is a remarkable achievement despite the process resulted as highly complex. Thus, the final attribution of a SLR deposition for Cd has been achieved in an unconventional way due to the overlap of the oxidative stripping potential of Zn and Cd. This conundrum has been overcome taking into account two deposition processes that were different with respect to the potential related to a small bump in the CVs: (1) potentiostatic in underpotential conditions and (2) potentiostatic in slightly overpotential conditions. The charge deposited by means of the two procedures to the deposition of the partial atomic layer of Cd over a sulfide substrate [8, 37] confirming the process as an effective SLR Cd deposition. Moreover, thanks to the XPS investigations, the occurrence of a complex sample composition (including the eventual presence of ZnS oxidation and/or the alloying between CdS and ZnS) is revealed. Finally, XPS measurements suggest that the structure is layered as expected from the E-ALD process applied to the growth of a p-n junction.

3. Experimental setups for operando experiments

3.1. Solutions

Both metal ions and chalcogenides solutions for the process are prepared with analytical reagent grade without further purification. Buffer solutions are prepared with double-distilled water and analytical reagent-grade acid and bases. Commonly, a buffer of $HClO_4$ (65%) and NH_4OH (33%) is used to freshly prepare solutions of the metal and chalcogenides ions at very small concentration (typically 0.5 mM).

3.2. Electrodes

Several works report E-ALD of semiconducting materials over a polycrystalline substrates, although very interesting, this films cannot be analyzed by means of the SXRD technique. In this context, very common substrates are Au or Ag single crystal with almost every low index facets as electrodic surface. We focus on the last, which is less noble, but less expensive, even though it requires a specific treatment of the surface to enable its use as a substrate. Moreover, as shown by our group, it is possible to correctly orient its crystals to low index planes with an easy and inexpensive procedure. Silver single crystal spheres can be grown in a graphite crucible according to the Bridgman technique. The crystal is strongly etched exposing the low index facets with a good contrast at the macroscale and a visual detection of the crystal orientation can be made [38]. These procedure is quite reliable, and most common problems are related to the growth step with the Bridgman technique. This step leads to very pure materials, but the resulting silver single crystal could have a concentration of defects unsuitable for the SXRD setups. So, the growth of the crystal needs to be carried very carefully in order to ensure the necessary quality of the electrodes. After the cut, the electrodic surface is polished with emery paper and successively finer grades of alumina powder down to 0.05 μm. Before each measurement, the electrodes are cleaned with water in an ultrasonic bath for 15 min and chemically polished using a patented procedure based on CrO_3. The surface roughness can be improved in ultra-high vacuum by performing several sputtering-annealing cycles.

3.3. Automated system

An automated system for the exchange of solution in the electrochemical cell was first built at the University of Florence and European synchrotron radiation facility (ESRF) workshops, enabling the deposition of several layers, up to 120 E-ALD, in few hours. The automated system has been implemented at the ID03 and ID32 beamlines of the European synchrotron radiation facility (ESRF) in Grenoble, France. The apparatus consists of pyrex solution reservoirs, solenoid valves, a distribution valve, and a flow-cell. The whole is under fully automatic computer control [12].

3.4. The flow cell

Improvements with respect to thin-layer cells have been made designing a cell with suitable windows and flow channels enabling the fast exchange of the solutions [12]. The working electrode is placed at the bottom part of the cell that is directly fastened to the sample holder of the diffraction beamline front end. This position is particularly convenient for the alignment of the electrode surface and for exposure to the X-ray radiation. Although a careful choice of the material has to be done, the electrochemical cell can be built with Teflon, Kelef, or other chemically resistant plastics. Among others, PEEK is gaining favor in the field of operand SXRD measurement due to its resistance to hard X-ray radiation. However, the PEEK suffers for the presence of some crystalline domains, and without an adequate design of the cell walls, the powder and amorphous patterns from the cell windows can hinder with the X-ray signal from the sample itself. We report the design defined by the joint work of the University of Florence and ESRF workshops in **Figure 2**.

http://dx.doi.org/10.5772/67355

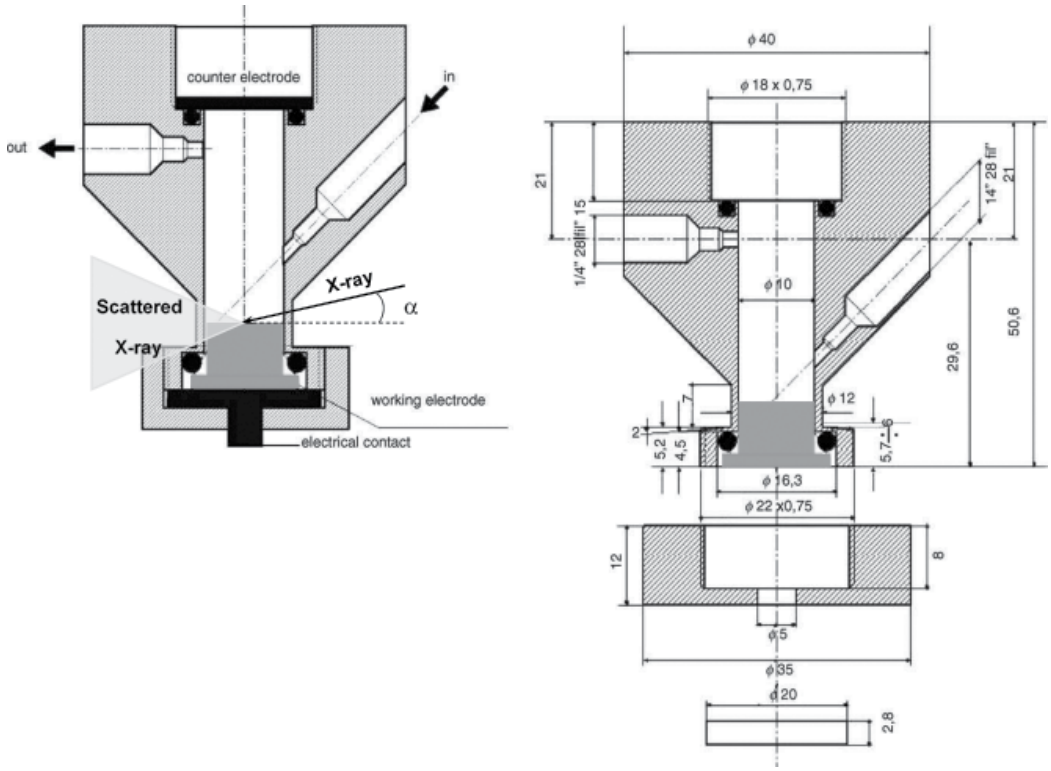

Figure 2. Technical specification for an electrochemical flow cell used in operando SXRD experiments.

The internal vessel is a cylinder with an internal diameter of 6.7 mm and a height of 40 mm. The electrochemical cell volume (1.5 mL) was delimited by the working electrode on one side and the counter electrode on the other side. The inlet and the outlet for the solutions were placed on the side walls of the cylinder. The counter electrode was a gold foil, and the reference electrode made of a small Ag/AgCl (KCl sat.) is placed in the outlet pipe. The attenuation of the X-rays along the typical path for an SXRD experiment can be estimated considering the absorbed radiation through a typical optical path as reported in **Figure 2**. Considering an incident angle with the wall and the electrolyte very close to 90°, **Figure 3** reported different thickness and material for the X-ray window in the cell, while the optical path in the electrolyte does not change in the different setups taken into consideration. The X-ray beam propagates through two walls 100 μm–1 mm thick and roughly 10 mm of water. In the following paragraphs we report two SXRD setups, one involving a Teflon cell (for CdS experiments, Section 4.1) and then a PEEK cell (for Cu_2S experiment, Section 4.2). For the first CdS experiment, it has been reported that a cell was made of Teflon, with a wall of 1 mm. At 20 keV, for this setup, **Figure 3** reports an overall transmission across the X-ray windows and electrolyte of roughly 40%, which is well matching the data reported in the literature (50%) [12]. PEEK ensures a lower attenuation of diffracted signal. Moreover, PEEK windows can be reduced to 100 μm thanks to its better mechanical proprieties. Hence, as depicted in **Figure 3**, this setup ensures a transmission very close to 70% at 24 keV. It is worth noticing that PEEK has a strong X-ray diffraction, reducing the thickness of the X-ray window by a factor of 10, makes completely undetectable the signal diffracted by PEEK.

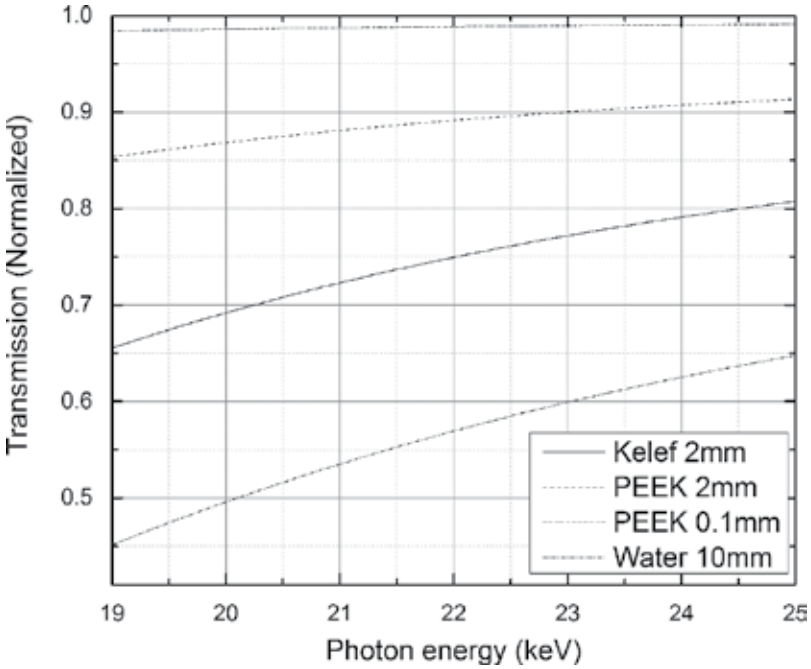

Figure 3. Transmission of X-ray at different energy through different surface.

We should report that the state-of-the-art E-ALD systems are also commercially available for the deposition of bigger electrode up to 4 cm^2, mainly used for polycrystalline substrates.

4. E-ALD and the sulfides structure

In this work, we report the intensity with respect to a coordinate system referred to as the pseudohexagonal surface unit cell of the Ag(111) substrate, in which the surface unit-cell parameters (a, b, c, α, β, γ) are defined so that the a and b vectors lay on the sample surface along the standard fcc [1 −1 0] and [−1 1 0] directions, while the c vector is perpendicular to the surface and parallel to the fcc [111] direction. The amplitude of the three vectors is given by the following relation together with the main surface cell angles.

$$\alpha = \beta = 90°, \gamma = 120°, |c| = \sqrt{3}\, a_0, |a| = |b| = \frac{a_0}{\sqrt{2}} \quad (3)$$

where a_0 is the lattice parameter of the cubic fcc cell of Ag. In the following, we adopted a reciprocal space metrics where *h*, *k*, and l are parallel to the a*, b*, and c* vectors of the reciprocal surface cell. In the following, we present two case studies on the CdS and Cu_2S comparing the results and the different applications of the SXRD due to different scientific questions that have to be answered for a better understanding of the E-ALD growth of these two materials.

4.1. CdS

E-ALD (or in this case ECALE) of CdS on Ag(111) has been involved in the testing of the experimental setup for in situ experiments by means of comparison of the structural results with theory and STM measurements. Moreover, the setups enabled structural determinations of the deposited film at different growth stages. In the first experiments at 20 kV performed by Giusti et al. [12], the reported attenuation is 50%, well matching with the attenuation curves reported in this work. The in situ diffraction measurements at controlled potential allowed the analysis of the CTRs for both the Ag(111) substrate and the Ag(111)/S surface. The fit of the CTRs showed that the last Ag layer on the bare metal has a contraction of 0.013 ± 0.008 nm toward the bulk. A vertical relaxation of the surface layer is observed in several (111) surfaces of noble metals and is due to the lack of bonding electrons at one side of low index surfaces [39]. Experimental works carried out on surfaces with a small roughness show an undetectable contraction of the surface layer [40, 41]. However, Ag(111) the contraction of the top layer is expected to strongly depend on the surface roughness [42]. A β-model has been involved in the fitting of the CTRs in order to take into account the surface roughness by means of fractionally occupied layers residing above the topmost complete one. In order to directly express the roughness in a length unit and not with a probability number, we can calculate the root-mean-square roughness σ, which can be calculated on the base of the Robinson model [43]. The oxidative absorption of S onto the Ag(111) surface induces strong modification on the shape of the CTRs. In fact, the best fit confirmed the top Ag layer with a site occupancy of 0.47 ± 0.07, in very good agreement with an S monolayer forming the $(\sqrt{7} \times \sqrt{7})R19.1$ supercell as determined by STM images under electrochemical control at the same applied potential [44].

Hence, this setup for SXRD measurement has been successfully compared with literature data. In this context, this setup enabled the structural analysis in a straightforward manner. Wurtzite and zincblende have a very similar diffraction pattern, and they differ by the (200) reflection for zincblende and the (101) and (103) reflections for wurtzite. On this ground, X-ray diffraction data collected either in situ or ex situ, revealed that the films always present an ordered wurtzite structure with the *c*-axis perpendicular to the surface, confirming the epitaxial growth of CdS by means of ECALE on the Ag(111) substrate. In plane, different privileged orientations have been observed indicating that the first S layer structure might play a crucial role for the structural order of the grown films. Moreover, the X-ray reflectivity measurements collected in situ during the ECALE deposition of the CdS film, pointed out the correct 1:1 stoichiometric ratio between Cd and S and showed that the film thickness increases proportionally to the number of deposition cycles. Recent in situ SXRD experiment about the growth of CdS on Ag(100) and Ag(110) has been reported by Carlà et al. [13] confirming the epitaxial growth also on these substrates. On Ag(100), CdS has been found to be wurtzite-like, with two domain rotated by 30° with respect to the other and rotated by 15° and 45° with respect to the quadratic surface cell of the Ag(100) facet. While on Ag(110), the growth of CdS involves both zincblende (one domain) and wurtzite structures (two domains). The wurtzite domains on the Ag(110) are rotated by 30° with respect to the other and aligned with the substrate's main axis. Besides, for Ag(111), a different relative orientation of the two wurtzite domains is reported. These works clearly showed the influences of the substrate orientation on the CdS structure. Moreover, electrochemical measurements on Ag(100)

and Ag(110) indicate that the charge associated with each CdS and S layer has an average value comparable to that found for films grown on Ag(111). In this context, the XRR data were fitted including a roughness factor in the fitting parameter calculated according to the Névot and Croce formalism [45–47]. The resulting film thickness has been found to be 52.5 ± 0.5 Å on Ag(110) and 46.5 ± 0.5 Å for Ag(100), while the theoretical value is 100.7 Å. To better explain the experiments, the authors suggest that the UPD process can be considered a dynamic process occurring in steps where rearrangements and reordering of the atoms can take place. For a detailed description of this interpretation, the reader should refer to Ref. [13]. Still, these experiments constitute another confirmation that the film thickness and stoichiometry can be controlled by the number of ECALE cycles, even on different facets.

4.2. Cu_2S

As reported in Section 2, chemical composition, local structure, and stacking sequence suggest that the E-ALD process would require numerous reorganization steps. SXRD experiments showed no Bragg peaks or Debye rings during the first deposition cycles for Cu_2S. A clear difference with respect to the CdS, probably related to the lower scattering factor of Cu with respect to Cd and the more structural complexity that can be found in the Cu-S compositional field. The Cu-S mineralogical system is structurally and compositionally highly complex including five different structures between the two endmembers, CuS (Covellite) and Cu_2S (Chalcocite). Thus, for this material, it is more difficult, though crucial, to understand its crystalline structure. In a recent paper, our group took into consideration the more stable and geometrically suitable structures in this system. Thus, the published structural results are not conclusive, and other experiments and analysis are in progress. However, recent operando SXRD data acquired for a sample of 80 E-ALD cycles show a hexagonal structure, although a low symmetry structure has been reported. Hexagonal planes are present in the structures of both the possible candidates for the interpretation of the SXRD data. Moreover, in both cases, the *c*-axis of the substrate and of the film coordinate system is parallel. Chalcocite structure has layers (not planes) made of distorted hexagons, a perturbation of these distorted hexagons to make them proper hexagons gives a plane with a hexagonal pattern of sulfur atom. In contrast, Covellite has a hexagonal plane with a much shorter bond length than the Ag hexagonal plane leading (see **Table 2**); the expected strain is compressive of −1.1% along the main Ag(111)R30 –3 × 4 reconstruction directions, while for chalcocite, the strain is expansive of 1.0% along the Ag(111)R30 –4 × 5 reconstruction direction. It is also worth noticing that chalcocite is far more stable than Covellite.

We proposed an attempt to map the indices of a chalcocite structure (Cu_2S) grown on Ag(111), based on two different orientation (Ag(111) and Ag(111)R30) with respect to the substrate. Although the chalcocite structure constitutes a suitable model for the Cu_2S, deposited by means of E-ALD, the transformation between the two crystallographic coordinates systems lead to unsatisfactory results.

Ag(111)	Covellite (CuS)	Chalcocite (Cu_2S)
2.889 Å	3.794 Å	~3.963 Å (mean of S–S distance of the hexagonal plane)

Table 2. Characteristic length of possible CuS /Ag(111) and Cu_2S /Ag(111) surfaces.

The periodicity along the zonal axis (Ag[111]) is reported in **Figure 4** by means of experimental l-scan in situ and ex situ. The periodicity along Ag[111] corresponding to an interplanar distance of 6.75 Å, very close to the half of the periodicity along c is as observed for the chalcocite [48]. The simulated l-scan correspond to a model constituted by the hexagonal compact packing of sulfur atoms with the same periodicity. The comparison between experimental and simulated l-scans confirmed the correspondence between the chalcocite structure and the structure of the sample along the Ag[111] axis when measured in situ, revealing the presence of another structure in the sample when measured ex situ. In order to highlight the origin of this structural evolution, the Bragg peak at (0.73 0.73 1.04) has been acquired in real time. The structure seems to change in a partially reversible manner while reaching the open circuit potential from the last applied potential. Comparing the data with the covellite structure, the periodicity along the *c* axis of the covellite is found to be not matching (16.34 Å). Moreover, the periodicity presented in **Figure 4** corresponds to a distance of 3.37 Å between two adjacent sulfur layer. Since the S–S distance is "modulated" by the presence of copper atoms (Cu:S ratio) in the Cu-S compositional field, according to Bolge, the measured distance should correspond to a stoichiometric ratio of 2:1(Cu:S) [49]. Although the periodicity of the sample along Ag[111] is well reproduced by chalcocite, on the plane covellite and chalcocite have similar expected strains (1%) for Ag(111)R30°. These data suggest chalcocite (Cu_2S) as a better model than covellite (CuS) for Cu_2S. However, the definition of a new structure forming the chalcocite one is needed to be able to conclusively describe the structure of this material. Even though the crystallographic structure of the sample is not clarified, the diffracted intensity on selected Bragg peaks during the in situ experiment increases monotonically as shown in **Figure 5**, thus confirming the growth of the films during the whole process.

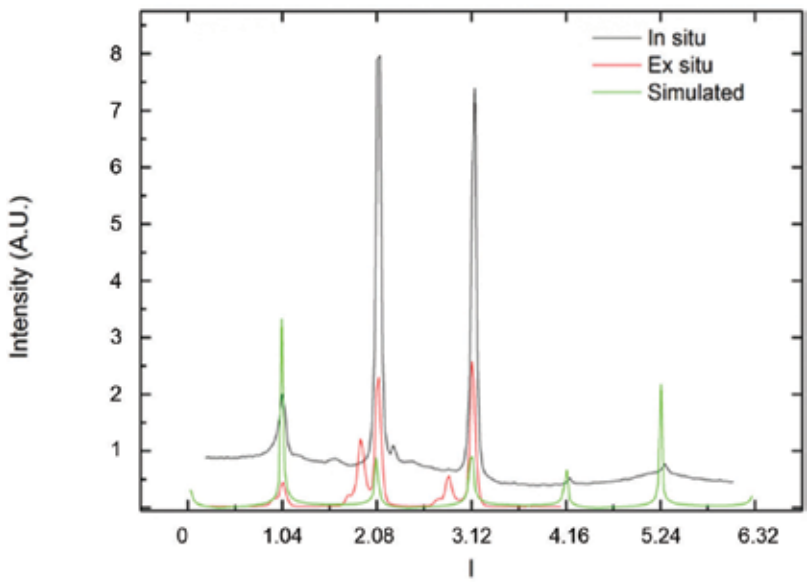

Figure 4. Operando (in situ), ex situ, and simulated l-scans (0.73, 0.73, l).

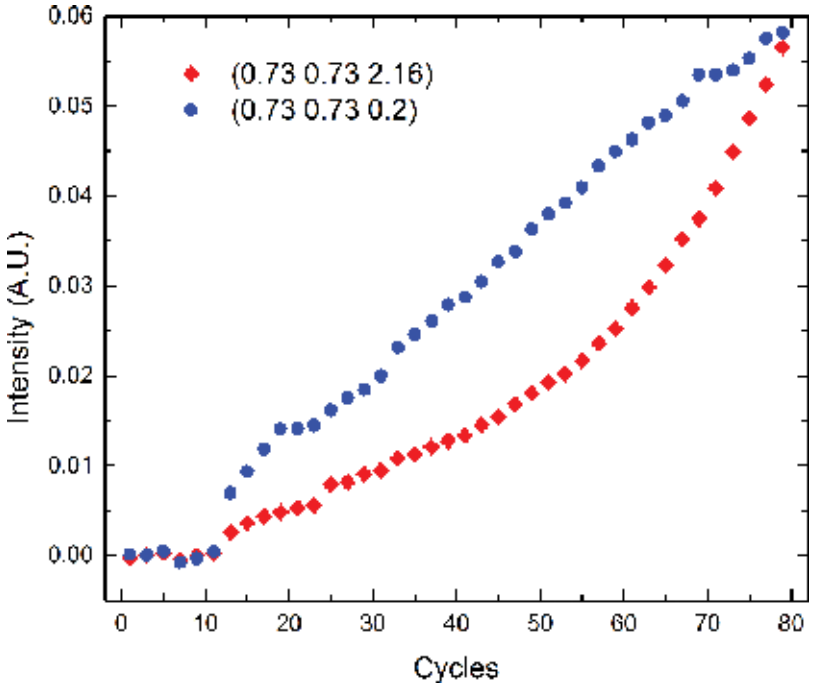

Figure 5. Diffracted intensity during the growth of Cu_2S ultra-thin film.

5. Conclusion

The first systems studied with operando SXRD has been chosen for their simple chemistry and because they had already been widely characterized with standard electrochemical and spectroscopical characterizations. By performing the operando SXRD, we have been able to address several open questions dealing with the effective growth process, the structures, the thicknesses, and the stoichiometry. SXRD has also successfully employed in the case of ultra-thin films grown by E-ALD, allowing to detect the surface reconstructions present in the first stages of the growth for CdS. The determination of thickness by means of the crystal truncation rods and reflectivity analysis revealed a very clear picture regarding the growth process of CdS, which is substantially different with respect to a mere layer-by-layer growth. In the case of Cu_2S, operando SXRD has revealed that the film crystallographic structure evolves as soon as the control potentials are removed from the cell with a time dynamics of few seconds. This structural transition is partially reversible if the applied potential is restored. Eventually, scanning along some selected reciprocal directions and taking advantage of the real-time acquisition of the diffraction intensity during the electrochemical evolution of the system allowed to understand both the structure and the stability of the Cu_2S. This gives the possibility of gathering information concerning the stoichiometry and its assessment by other techniques. In fact, for the Cu-S system, there is a very well-defined relationship between the structure and the Cu:S ratio; its stability revealed why the stoichiometry is coming from

ex situ XPS or why stripping voltammetry is not comparable with the stoichiometry coming from operando structural investigations. The unexpected stoichiometry of the film for Cu_2S raises several questions about the stability of this system. In conclusion, the operando SXRD results concern both CdS and Cu_2S while confirming the possibility of growing highly ordered ultra-thin films with high reproducibility, and they set a new interesting challenge for the fundamental surface science in explaining the complex mechanism, which is behind the growth of crystal by means of E-ALD.

Author details

Andrea Giaccherini[1]*, Roberto Felici[2] and Massimo Innocenti[1]

*Address all correspondence to: andrea.giaccherini@unifi.it

1 Department of Chemistry, University of Florence, Sesto Fiorentino, Italy

2 Istituto SPIN - CNR, Rome, Italy

References

[1] B.W. Gregory, J.L. Stickney. Electrochemical atomic layer epitaxy (ECALE). J. Electroanal. Chem. 1991;**300**:543–561.

[2] M. Innocenti, G. Pezzatini, F. Forni, M.L. Foresti. CdS and ZnS deposition on Ag (111) by electrochemical atomic layer epitaxy. J. Electrochem. Soc. 2001;**148**:C357–C362.

[3] M. Innocenti, F. Forni, G. Pezzatini, R. Raiteri, F. Loglio, M.L. Foresti. Electrochemical behavior of As on silver single crystals and experimental conditions for InAs growth by ECALE. J. Electroanal. Chem. 2001;**514**:75–82.

[4] F. Loglio, M. Innocenti, A. Jarek, S. Caporali, I. Pasquini, M.L. Foresti. Nickel sulfur thin films deposited by ECALE: Electrochemical, XPS and AFM characterization. J. Electroanal. Chem. 2010;**638**(10):15–20.

[5] M. Innocenti, L. Becucci, I. Bencistà, E. Carretti, S. Cinotti, L. Dei, F. Di Benedetto, A. Lavacchi, F. Marinelli, E. Salvietti, F. Vizza, M.L. Foresti. Electrochemical growth of Cu-Zn sulfides. J. Electroanal. Chem. 2013;**710**:17–21.

[6] F. Loglio, M. Innocenti, G. Pezzatini, M.L. Foresti. Ternary cadmium and zinc sulfides and selenides: Electrodeposition by ECALE and electrochemical characterization. J. Electroanal. Chem. 2004;**562**(1):17–125.

[7] M. Innocenti, L. Becucci, I. Bencistà, E. Carretti, S. Cinotti, L. Dei, F. Di Benedetto, A. Lavacchi, F. Marinelli, E. Salvietti, F. Vizza, M.L. Foresti. Ternary cadmium and zinc sulfides and selenides: Electrodeposition by ECALE and electrochemical characterization. J. Electroanal. Chem. 2013;**70**:17–21.

[8] M. Innocenti, S. Cinotti, I. Bencistà, E. Carretti, L. Becucci, F. Di Benedetto, A. Lavacchi, M.L. Foresti. Electrochemical growth of Cu-Zn sulfides of various stoichiometries. J. Electrochem. Soc. 2014;**161**(1):D14–D17.

[9] F. Di Benedetto, S. Cinotti, A. Guerri, A. De Luca, A. Lavacchi, G. Montegrossi, F. Carlà, R. Felici, M. Innocenti. Physical characterization of thin films of $Cu_xZn_yS_z$ for photovoltaic applications. ECS Trans.. 2013;**58**(11):59–65.

[10] M. Innocenti, F. Di Benedetto, A. Lavacchi, N. Cioffi, R. Felici and L.A. Pardi. Fabricating energy devices with low environmental impacts. SPIE Newsroom. 11 January 2016.

[11] K Rajeshwar. Electrosynthesized thin films of group II–VI compound semiconductors, alloys and superstructures. Adv. Mater. 1992;**4**:23–29.

[12] M.L. Foresti, A. Pozzi, M. Innocenti, G. Pezzatini, F. Loglio, E. Salvietti, A. Giusti, F. D'Anca, R. Felici, F. Borgatti. In situ X-ray analysis under controlled potential conditions: An innovative setup and its application to the investigation of ultrathin films electrodeposited on Ag(111). Electrochim. Acta 2006;**51**:5532–5539.

[13] F. Carlà, F. Loglio, A. Resta, R. Felici, E. Lastraioli, M. Innocenti, M.L. Foresti. Electrochemical atomic layer deposition of CdS on Ag single crystals: Effects of substrate orientation on film structure. J. Phys. Chem. C 2014;**118**:6132–6139.

[14] U. Demir, C. Shannon. Langmuir. 1994;**10**:2794.

[15] F. Loglio, M. Innocenti, G. Pezzatini, F. Forni, M.L. Foresti. Experimental conditions for CdSe layer-by-layer growth. In: P.C. Andriacos, P.C. Searson, C. Reidsema-Simpson, P. Allongue, J.L. Stickney, G.M. Oleszek. Electrochemical Processing in ULSI Fabrication III. Pennington, New Jersey: The Electrochemical Society; 2000. pp. 28–40.

[16] F. Forni, M. Innocenti, G. Pezzatini, M. Foresti. Electrochemical aspects of CdTe growth on the face (111) of silver by ECALE. Electrochim. Acta 2000;**45**:3225–3231.

[17] D.W. Suggs, J.L. Stickney. Studies of the surface structures formed by the alternated electrodeposition of Cd and Te on the low-index planes of Au: II. STM studies. Surf. Sci. 1993;**290**:375.

[18] B.E. Hayden, I. Nandhakumar. J. In-Situ STM Study of Te UPD Layers on Low Index Planes of Gold. Phys. Chem. B 1997;**101**:7751.

[19] F. Loglio, A. Telford, E. Salvietti, M. Innocenti, G. Pezzatini, S. Cammelli, F. D'Acapito, R. Felici, A. Pozzi, M. Foresti . Ternary $Cd_xZn_{1-x}Se$ nanocrystals deposited on Ag(111) by ECALE: AFM and EXAFS characterization. Electrochim. Acta 2008;**53**:6978–6987.

[20] F. Loglio, M. Innocenti, G. Pezzatini, M. Foresti. Electrochemical and morphological characterization of $Cd_xZn_{1-x}S$ electrodeposited on Ag(111) by ECALE. In: K. Kondo, D.P. Barkey, J.C. Bradley, F. Argoul, P.C. Andriacacos, J.L. Stickney, editors. Morphological Evolution of Electrodeposits-and-Electrochemical Processing in ULSI Fabrication and Electrodeposition of and on Semiconductors IV. New York, Washington: Kluwer Academic/Plenum Publishers; 2001. pp. 365–380.

[21] F. Loglio, M. Innocenti, G. Pezzatini, M. Foresti. Ternary cadmium and zinc sulphides and selenides: Electrodeposition by ECALE and electrochemical characterization. J. Electroanal. Chem. 2004;**562**:117–125.

[22] S.C. Ray, M.K. Karanjai, D. DasGupta. Deposition and characterization of ZnxCd1− xS thin films prepared by the dip technique. Thin Solid Films. 1998;**322**:117.

[23] Y. Golan, B. Alperson, I. Rubinstein, G. Hodes, J. L. Hutchison. Extended Abstracts-Electrochemical Society Meeting; May 1994; San Francisco. p. 94-1, 874, 1350.

[24] Y. Golan, L. Margulis, I. Rubinstein, G. Hodes, J.L. Hutchison. Proceedings of the 13th International Congress on Electron Microscopy. In: B. Jouffrey, C. Colliex, editors. July 1994; Paris. p. 2A, 345.

[25] Y. Golan, G. Hodes, I. Rubinstein. Electrodeposited Quantum Dots. 3. Interfacial Factors Controlling the Morphology, Size and Epitaxy. J. Phys. Chem. 1996;**100**:2220–2228.

[26] M. Innocenti, I. Bencistà, S. Bellandi, C. Bianchini, F. Di Benedetto, A. Lavacchi, F. Vizza and M.L. Foresti. Electrochim. Acta. 2011;**58**:599– 605

[27] I. Bencistà, F. Di Benedetto, M. Innocenti, A. De Luca, G. Fornaciai, A. Lavacchi, G. Montegrossi, W. Oberhauser, L.A. Pardi, M. Romanelli, F. Vizza and M.L. Foresti. Phase composition of Cu_2S thin films: Spectroscopic evidence of covellite formation. Eur. J. Miner. 2012;**24**:879–884.

[28] F. Di Benedetto, S. Cinotti, F. D'Acapito, F. Vizza, M.L. Foresti, A. Guerri, A. Lavacchi, G. Montegrossi, M. Romanelli, N. Cioffi, M. Innocenti . Electrodeposited semiconductors at room temperature: An X-ray Absorption Spectroscopy study of Cu-, Zn-, S-bearing thin films. Electrochim. Acta 2015;**179**:495–503.

[29] C.C. Uhuegbu, E.B. Babatunde, C.O. Oluwafemi. The Study of Copper Zinc Sulphide (CuZnS2) Thin Films. Turk. J. Phys. 2008;**32**:39-47.

[30] K.A. Aduloju, A.I. Mukolu. Optical absorption and transmission in CuZnS alloys. Glob. J. Pure Appl. Sci. 2009;**15**(3):421–425.

[31] M. Innocenti, S. Cattarin, F. Loglio, T. Cecconi, G. Seravalli, M.L. Foresti. Electrochim. Acta 2004;**49**:1327–1337.

[32] M. Innocenti, S. Bellandi, E. Lastraioli, F. Loglio, M.L. Foresti. Selective electrodesorption based atomic layer deposition (SEBALD): A novel electrochemical route to deposit metal clusters on Ag(111). Langmuir 2011;**27**(18):11704–11709.

[33] J.R. Craig, G. Kullerud. The Cu-Zn-S System. Miner. Depos. 1973;**8**:81–91.

[34] M. Miyauchi, T. Hanayama, D. Atarashi, E. Sakai. Photoenergy conversion in p-type Cu_2ZnSnS_4 nanorods and n-type metal oxide composites. J. Phys. Chem. C 2012;**116**:23945–23950.

[35] I.D. Olekseyuk, I.V. Dudchak, L.V. Piskach. Phase equilibria in the Cu_2S–ZnS–SnS_2 system. J. Alloys Compd. 2004;**368**:135–143.

[36] E. Berretti, S. Cinotti, S. Caporali, N. Cioffi, A. Giaccherini, F. Di Benedetto, M.L. Foresti, G. Montegrossi, A. Lavacchi, F. Vizza, R.A. Picca and M. Innocenti. Electrodeposition and characterization of p and n sulphide semiconductors composite thin film. J. Electrochem. Soc. 2016;**163**(12):D3034–D3039 .

[37] S. Caporali, A. Tolstogouzov, O.M.N.D. Teodoro, M. Innocenti, F. Di Benedetto, S. Cinotti, R.A. Picca, M.C. Sportelli, and N. Cioffi. Sn-deficiency in the electrodeposited ternary CuxSnySz thin films by ECALE. Sol. Energ. Mater. Sol. Cells. 2015;**138**:9.

[38] M.L. Foresti F. Capolupo, M. Innocenti, F. Loglio. Visual detection of crystallographic orientations of face-centered cubic single crystals. Cryst. Growth Des. 2002;**2**(1):73–77.

[39] R.J. Needs, M.J. Godfrey, M. Mansfield. Theory of surface stress and surface reconstruction. Surf. Sci. 1991; **242**: 215.

[40] M.F. Toney, J.N. Howard, J. Richer, G.L. Borges, J.G. Gordon, O.R. Melroy, D.G. Wiesler, D. Yee, L.B. Sorensen. Voltage-dependent ordering of water molecules at an electrode–electrolyte interface. Nature 1994;**368**:444.

[41] E.A. Soares, V.B. Nascimento, V.E. de Carvalho, C.M.C. de Castilho, A.V. de Carvalho, R.Toomes, D.P. Woodruff. Structure determination of Ag(111) by low-energy electron diffraction. Surf. Sci. 1999;**419**:89.

[42] N.H. de Leeuw, C.J. Nelson. A Computer Modeling Study of Perfect and Defective Silver (111) Surfaces. J. Phys. Chem. B 2003;**107**:3528.

[43] I.K. Robinson. Crystal truncation rods and surface roughness. Phys. Rev. 1986;**B33**:3830.

[44] M.L. Foresti, G. Pezzatini, M. Cavallini, G. Aloisi, M. Innocenti, R. Guidelli. Electrochemical Atomic Layer Epitaxy Deposition of CdS on Ag(111): An Electrochemical and STM Investigation. J. Phys.Chem. B 1998;**102**:7413.

[45] Software Reflectivity Tool Parratt 32; HMI: Berlin, 1999.

[46] L.G. Parratt . Surface studies of solids by total reflection of X-rays. Phys. Rev. 1954;**95**:359–369.

[47] L. Névot, P. Croce . Caractérisation des Surfaces par Réflexion Rasante de Rayons X. Application à l'Etude du Polissage de Quelques Verres Silicates. Rev. Phys. Appl. 1980;**15**:761–780.

[48] H.T. Evans. Crystal structure of low chalcocite. Nature Phys. Sci. 1971;**232**:19.

[49] R.J. Goble. The relationship between crystal structure, bonding and cell dimensions in the copper sulphides. Can. Miner. 1985;**23**:61–76.

Chapter 4

X-Ray Absorption Spectroscopy Study of Battery Materials

Marco Giorgetti and Lorenzo Stievano

Additional information is available at the end of the chapter

http://dx.doi.org/10.5772/66868

Abstract

X-ray absorption spectroscopy (XAS) as a local structural tool for the study of the electrochemical processes in battery materials is highlighted. Due to its elemental specificity and high penetration of the X-rays in the 4–35 keV range, XAS is particularly suited for this, allowing the study of battery materials using specifically developed *in situ* electrochemical cells. This energy is required to dislodge one core electron from transition metal or p-group atoms, which are commonly used as redox centers in positive and negative electrode materials. In such a simple picture, the ejected photoelectron is scattered by the surrounding atoms, producing characteristic traces in the X-ray absorption spectrum. Both positive and negative electrode materials (intercalation, alloy and conversion electrodes) can be studied. The chapter starts with an introduction of the context around battery studies, followed by a short explanation of the photoelectric effect at the basis of the X-ray absorption phenomenon and to specific features of XAS. A selection of XAS experiments conducted in the field of batteries will be then outlined, also emphasizing the effects due to nanoscale dimension of the material studied. Finally, a perspectives section will summarize the specific role that this spectroscopy has played in the battery community.

Keywords: X-ray absorption spectroscopy, lithium batteries, energy materials, electrode materials

1. Introduction

One of the most challenging difficulties that our planet has to face in the next decades is the sustainable use of energy. In particular, the demand for advanced energy storage devices has increased significantly, motivated by a variety of different needs of our technologically driven, highly mobile, energy challenged society. For instance, batteries are the devices that can solve the problems inherent to the intrinsic intermittency of renewable energy sources, since they can store the energy surplus produced in excess when the plant is operating and then feed it to the power grid when

there is a peak of consumption. Moreover, they are also targeted to fulfill the ever growing demand of energy for portable applications (mobile phones and computers, and nowadays cars and trucks). The excellent performance and the well-established technology of lithium-ion batteries (LIBs) put them in a crucial position for supporting this new energy revolution. Several post-LIB systems, such as lithium-sulfur batteries (LSBs), lithium-oxygen batteries (LOBs) or sodium-ion batteries (NIBs), have also been proposed in the last years, as sustainable performing alternatives to LIBs.

Differently from other well-established battery technologies, such as alkaline or lead-acid batteries, LIBs (as well as the other post-LIB systems) are based on the famous "rocking chair" mechanism [2], where the Li^+ cations are exchanged alternatively between the positive and the negative electrode during the discharge and the charge process, as shown in **Figure 1**. In such a system, the two electrodes can be any sort of material that are able to undergo reversibly to a reduction/oxidation process at a specific high or low potential (for the positive or negative electrode, respectively) with the concomitant addition/elimination of Li^+ cations. For this reason, many materials able to form lithiated phases have been proposed for playing the role of electrode materials.

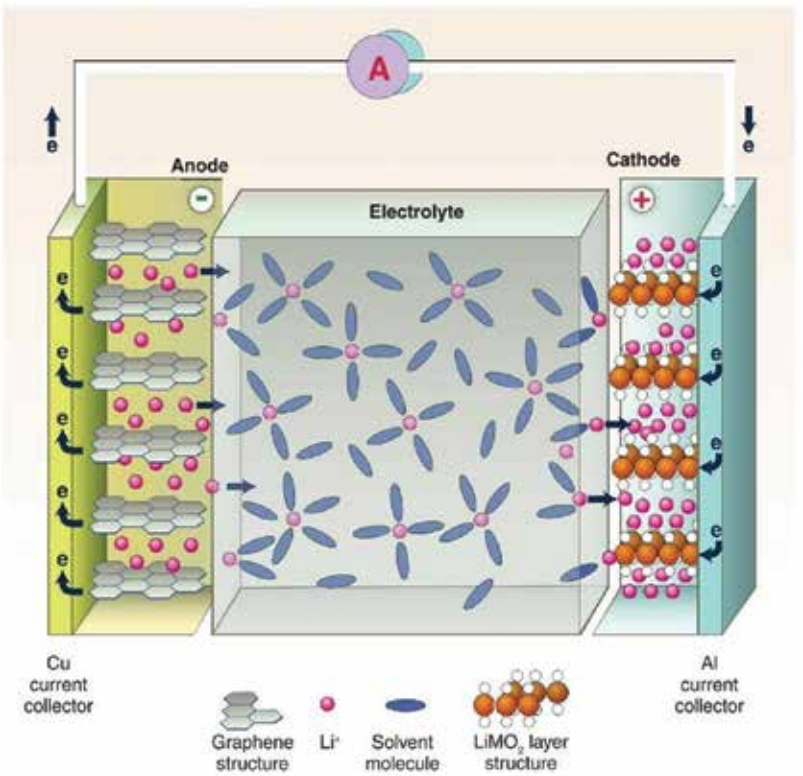

Figure 1. Schematic representation of the discharge of a Li^+-ion battery: a graphite-based negative electrode undergoes Li^+ deintercalation, according to the following reaction:.

$$\mathbf{Li_xC} \leftrightarrows \mathbf{C} + x\ Li^+ + x\ e^-$$

Li^+ ions migrate toward the $Li_{1-x}CoO_2$ positive electrode forming the reduced $LiCoO_2$:

$$Li_{1-x}CoO_2 + x\ Li^+ + x\ e^- \leftrightarrows LiCoO_2$$

Typical electrolytes are based on a lithium salt (*e.g.* $LiPF_6$) dissolved in a mixture of liquid carbonates (Ethylene carbonate, propylene carbonate, etc.) Reproduction from Ref. [1].

http://dx.doi.org/10.5772/66868

The very large number of possible host materials for Li^+ have generated a great deal of works on potential LIBs electrode materials, from the micro to the nanosized range, which may accommodate lithium via different reaction mechanisms, including intercalation [3–5], alloying [6–8] and conversion [9] reactions. In addition to the reaction mechanisms at the electrodes, other features concerning the electrolytes and their interaction with the electrodes, including the formation of the solid-electrolyte interphase (SEI) [10], which is of primordial importance for the stability and the cycle life of the battery, have been thoroughly studied.

In such a picture, many characterization methods have been proposed and efficiently used, either simply *ex situ*, *in situ* or under even *operando* conditions for the characterization of the starting materials and of their reaction mechanisms such as X-ray diffraction (XRD) [11], infrared [12], Raman [13], Mössbauer [14] and X-ray photoelectron spectroscopy [15, 16].

X-ray absorption spectroscopy (XAS) can also be counted among the characterization tools used in the field of batteries. Indeed, it is one of the techniques of choice for retrieving structural and electronic information, especially when the materials or some of the species formed through the electrochemical reactions are not crystalline and cannot be studied by diffraction techniques. The main important characteristics of XAS are: (i) its element specificity, which allows the study of a particular element by concentrating on its K (or in some cases L) absorption edge; (ii) the possibility of tuning it to different sites (for instance Fe and P in $LiFePO_4$), thus providing sources of complementary information on the same compound; (iii) the physico-chemical information contained in the near-edge structure of the XAS signals, which can be used to reveal the formal oxidation state and the local symmetry of the probed atom; (iv) the possibility of doing *operando* measurements by collecting XAS spectra during electrochemical cycling using specifically developed *in situ* cells. In this case, the physico-chemical properties and the local structure of the studied element can be monitored at all moments during the charge and discharge processes.

To the best of our knowledge, the first use of XAS in the field of batteries dates back to the paper of Mc Breen *et al.* [17]. Several reviews have appeared more recently, resuming the principal advances allowed by the application of XAS in this research field [18–21]. In this chapter, after a short presentation of the techniques and of the relative experimental methods, a selection of XAS experiments conducted in the field of batteries will highlight the potentiality of the technique in the *in situ* characterization of nanosized, nanostructured and badly organized materials. This knowledge is necessary to obtain a precise description of the electrochemical mechanisms governing battery's chemistry.

2. X-ray absorption spectroscopy (XAS)

XAS, also known as X-ray absorption fine structure (abbreviated as XAFS) spectroscopy, is a powerful tool that provides information on a very local scale (4–5 Å) around a selected atomic species and is well suited for the characterization of not only crystals but also materials that possess little or no long-range translational order. It is based on the absorption: when a sample

is exposed to X-rays, it will absorb part of the incoming photon beams, which is mainly generated by the photoelectric effect for energy in the hard X-rays regimes (3–50 KeV). XAS is even selective for the atomic species and also allows us to tune the X-rays beam selectively to a specific atomic core (the absorption energy of next elements are sufficiently spaced), and therefore it probes the local structure around only the selected element that are contained within a material. The element-specific characteristic of XAS, providing both chemical and structural information at the same time, differentiates it from other techniques, such as the X-ray scattering. In this respect, it serves as a unique tool for the investigation of battery materials during charge-discharge cycles.

XAS experiment measures the absorption coefficient μ as a function of energy E: as E increases, μ generally decreases ($\mu \sim E^{-3}$), that is matter becomes more transparent and X-rays more penetrating, save for some discontinuities, where μ rapidly rises up. These exceptions correspond to particular energies, the so-called absorption edges E_0, which are the characteristic of the material, where the amount of energy exactly matches the core electron binding energy. The edge energies vary with atomic number approximately as a function of Z^2 and both K and L levels can be used in the hard X-ray regime (in addition, M edges can be used for heavy elements in the soft X-ray regime), which allows most elements to be probed by XAS with X-ray energies between 4 and 35 keV. Because the element of interest is chosen in the experiment, XAFS is element-specific.

XAS (or XAFS) is generally used to refer to the entire spectrum, which is constituted by the edge region called X-ray absorption near edge spectroscopy (XANES), which is limited at the first 80–100 eV above the edge, and a post-edge region extended X-ray absorption fine structure (EXAFS), which is extended up to 1000 eV above the absorption edge. The distinction between XANES and EXAFS remains arbitrary, but some important approximations in the theory allow us to interpret the extended spectra in a more quantitative way than is currently possible for the near-edge spectra. The XANES region, comprising the pre-edge and the absorption edge itself, is strongly sensitive to oxidation state and coordination chemistry of the absorbing atom of interest. The EXAFS region has been largely exploited to gain quantitative structural information such as first shell distance of the metal site and the coordination number. EXAFS comprises periodic undulations in the absorption spectrum that decay in intensity as the incident energy increases well over (~1000 eV) the absorption edge. These undulations arise from the scattering of the emitted photoelectron with the surrounding atoms. A striking feature of XAFS is that this technique can be applied to all states of matter, and for both crystalline and amorphous materials, it has been used with great success in many research fields, such as liquids [22], catalysis [23–25], biology [26], inorganic metal complexes [27] and electrochemical interfaces [28]. Several excellent books are also available [29–32]. The website of the International XAFS society is reachable at http://www.ixasportal.net/ixas/.

When discussing XAS, we are primarily concerned with the absorption coefficient μ, which gives the probability that X-rays will be absorbed according to Beer's Law:

$$\mu \cdot x = \ln(I_0/I) \tag{1}$$

$$\left(\frac{\mu}{\rho}\right) \cdot \rho \cdot x = \ln\left(I_0/I\right) \tag{2}$$

being I_0 is the intensity of X-ray incident on a sample, x is the sample thickness and I is the intensity transmitted through the sample, as shown in **Figure 2**. The measured quantity, μ (cm^{-1}), is the linear X-ray absorption coefficient which is closely related to its inverse $1/\mu$ called the absorption length (cm). The absorption length is defined as the linear distance of the material over which the X-ray intensity results attenuated by a factor $1/e$ ~ 37%. This quantity is important in planning the experiment, as it sets the scale for choosing an appropriate sample thickness.

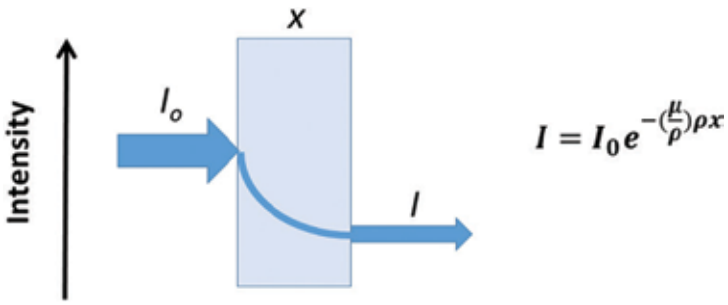

Figure 2. Sketch for the X-Ray absorption measurement in transmission mode.

Normalization to the density of the material results quite convenient, as different states of matter may be analyzed: the mass absorption coefficient μ_m (cm^2/g) is the linear absorption coefficient divided by the density of the absorber.

X-rays ionize and the absorbing atom turns to an excited ion after the electron liberation. Relaxation may occur in two different ways: (i) the core-hole may be filled by a higher-energy electron and the energy difference is released as a second photon, whose energy is smaller compared to that of the primary absorption, for an inner transition occurs (the detection of which is at the basis of another x-ray analytical technique, X-ray Fluorescence Spectroscopy—XFS) or (ii) an Auger secondary electron may be freed, after having absorbed the second photon. The measurement of these electrons is made possible by Auger spectrometers. In the soft X-ray region (<2 keV), the Auger process is more likely to occur, unlike for higher energies where X-ray fluorescence dominates.

2.1. Extended X-ray absorption fine structure (EXAFS)

When X-ray is absorbed by a core-level electron, a photoelectron with wavevector k is created and propagates away from the atom as a spherical wave as seen from the blue lines of **Figure 3**. The wavevector k is related to the excess of the energy $\hbar\omega$-E_0 of the incoming X-ray beam by:

$$k = \sqrt{\frac{2m}{\hbar^2}\left(\hbar\omega - E_0\right)} \tag{3}$$

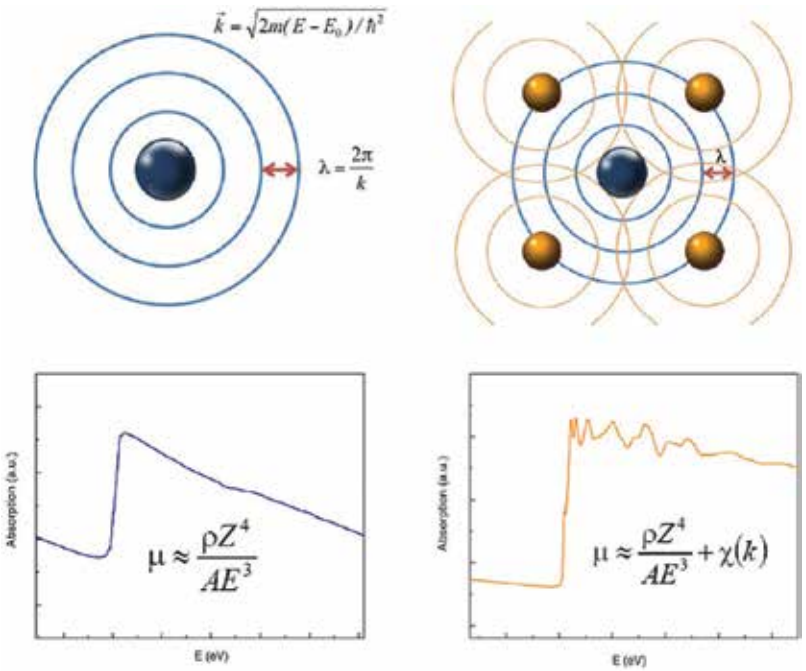

Figure 3. Emission of a photo-electron for an isolated (left) and a coordinated (right) atomic species. In the latter the absorption coefficient measured at a central atom threshold shows a fine structure due to the presence of neighboring atoms. Reproduced from Ref. [18].

where E_0 is the binding energy of the core-electron that is excited and $E = \hbar\omega$ is the energy of the absorbed x-ray photon. Thus, the excess of energy rules out the optical property of the photo-electron created by the photoabsorption process. In case of isolated atoms, the propagation is simply described by one wave going away from the atom and the absorption coefficient μ is described by a smooth function of energy, indicated in the lower panel of **Figure 3**. Its value depends on the sample density ρ, atomic number Z, atomic mass A and the X-ray energy E, roughly expressed as:

$$\mu_0 \approx \frac{\rho Z^4}{A E^3} \tag{4}$$

The appendix 0 indicates the value for an isolated atom. It is remarkable here that due to its Z^4 dependence, the absorption coefficients of different elements exhibit big discrepancies, (spanning several orders of magnitude) so a good contrast between different materials can be achieved for any sample thickness and concentrations by selecting the X-ray energy. This fact is at the origin of the X-rays imaging techniques based on contrast.

If other atoms are located in the vicinity of the absorber (the central atom), the photoelectron is scattered by the neighbors (yellow atoms) and so does every atom in the material. The incoming and the scattered wave interferes either constructively or destructively as a function of the energy of the X-ray beam. Therefore, the observed absorption coefficient is expected to vary periodically as a function of the energy as depicted at the bottom right of **Figure 3**. In the latter

http://dx.doi.org/10.5772/66868

case, the total absorption coefficient μ can be expressed as the isolated atomic absorption μ_0, modulated by a correction factor $\chi(E)$, the oscillation, which is also defined as the EXAFS signal:

$$\mu(E) = \mu_0(E)\,[1 + \chi(E)] \tag{5}$$

This allows one to extract the oscillations from a raw experimental spectrum:

$$\chi = \left[\left(\mu(E) - \mu_0(E)\right]\right/ \mu_0(E) \tag{6}$$

For practical purpose, the denominator is often replaced by $\mu_0(E_0)$, which is the atomic absorption evaluated at the edge energy. $\chi(k)$ can be considered as the fractional change in absorption coefficient induced by the presence of neighboring atoms.

Within this simple description, the EXAFS can be represented by an oscillation, which of course can be described by terms of amplitude and phase. In a first approximation, the amplitude term depends on the nature and the number of near neighbors around the central atoms and the phase on the mutual distance photoabsorber scatterer. This leads to a simple expression for EXAFS in terms of different parameters affecting the fine structure:

$$\chi(k) \sim \sum_{\mathrm{j}} \frac{N_j F_j(k)}{k\, r_j^2} \sin\left[2k\, R_j + \delta(k)\right] \tag{7}$$

where N_j represents the coordination number of identical atoms at approximately the same distance r_j from the central atom. This group of atoms is called as a coordination shell and contributes to one components of the EXAFS signal. The peculiar $F_j(k)$ term is called the backscattering amplitude and depends on the nature of the scatterer atom. Different atom types have different backscattering amplitude. A crucial issue is given by the inverse quadratic dependence of the oscillation to the distance. This is due to the decay of the photoelectron as a function of time and distance and thus making the EXAFS a short-range structural probe. The first term of the phase $2kR_j$ is due to the geometrical phase shift suffered by the photoelectron with wavevector k on its trajectory twice the distance r_j between the photo absorber and the scatterer. In addition, as the electron is not moving in a constant potential, a phase shift $\delta(k)$ has to be added to this expression to account for the interaction of the electron with the varying potential of the absorbing and backscattering atom.

Several effects have to be taken into account to complete the description of real systems, and they all can be considered damping terms. They are (i) the structural and thermal disorder; (ii) the limited mean free path of the photoelectron; and (iii) the relaxation of all the other electrons in the absorbing atom in response to the hole in the core level. The first term is due to the fact that atoms in matter vibrate around their equilibrium position depending on temperature. This atomic motion reduces the EXAFS amplitude, and a term called the EXAFS Debye-Waller factor σ^2 is introduced. In EXAFS, this term corresponds to the mean square average of the difference of the displacement of the backscatterer relative to the displacement of the absorber. The second term is due to inelastic scattering processes of the photoelectron with other electron and thus an additional damping factor is introduced, where $\Lambda(k)$ is the

photoelectron mean free path (how far the electron travels before scattering inelastically). Finally, the amplitude reduction term S_0^2 accounts for the shake-up/shake-off processes of the central atom. Those processes (multi-excitations) refer to the excitations of the remaining $Z - 1$ "passive" electrons of the excited atom. This is a scale factor, and it is usually in the 0.7–1 range. By taking in consideration with these effects, the EXAFS equation becomes:

$$\chi(k) = \sum_j \frac{N_j F_j(k)}{k r_j^2} e^{-2k^2\sigma^2} e^{-2R_j/\lambda(k)} S_0^2 \sin\left[2k R_j + \delta(k)\right] \tag{8}$$

This is valid for the plane wave approximation, *K* threshold, single scattering, single electron approximation and "sudden" approximation. A similar equation valid for the other edges (L_{III}, etc.) must be considered. The structural and non-structural parameters appearing in the equation sum up to compose the EXAFS spectrum. To access these parameters in an experimental EXAFS spectrum, a data analysis has to be performed. This procedure is time consuming and it should be considered the slow step of the overall XAFS methodology.

EXAFS data analysis is normally done by using code programs, which permit to calculate the theoretical EXAFS spectrum based on *ab initio* calculations, followed by a further step which compares the experimental signals to the theoretical ones (fitting procedures). A rather complete list of the available software can be found at: http://www.esrf.eu/Instrumentation/software/data-analysis/Links/xafs. Typical widely used computer programs are GNXAS [33], FEFF [34, 35] and EXCURV [36]. EXCURV is a program, which simulates EXAFS spectra using rapid curved-wave theory. GNXAS package is based on multiple-scattering (MS) calculations and a fitting procedure of the raw experimental data, also allowing multiple edge fittings and a non-Gaussian distribution models for the atoms pair distribution. FEFF allows MS calculations of both EXAFS and XANES spectra for atomic clusters. The code yields scattering amplitudes and phases used in many modern XAFS analysis codes. It is also linked to the IFEFFIT package [37, 38], a suite of interactive code for XAFS analysis, combining high-quality and well-tested XAFS analysis algorithms, tools for general data manipulation and graphical display of data.

Two more considerations should be made on EXAFS data analysis. The first is that XAS (and therefore the results obtained by an EXAFS analysis) is a bulk technique and thus all the atoms irradiated by the beam contribute to the overall XAS spectrum. The same is true in the case of a multicomponent system (for instance two phases in equilibrium of a polymorphic species). Each component or phase gives its contributions. An example to disclose the simple component of a species, such as in the case of gold nanoparticles and its precursors, appeared [39]. Alternatively, an efficient use of chemometry has been proposed for the analysis of XAS data in such cases [40]. This approach has interesting implication for the interpretation of spectra recorded during an *operando* acquisition and an example will be presented in the next section.

The second consideration concerns the EXAFS data analysis of nanoparticles and nanostructures [41, 42]. This issue has been addressed for metal nanoparticles first [43], evidencing that

http://dx.doi.org/10.5772/66868

by decreasing the size of the material there is a significant effect on the observed coordination number, due to the increased surface/bulk ratio. A specific example of this effect on a battery material will be presented in the case study section.

2.2. X-ray absorption near edge spectroscopy (XANES)

The XANES region is sensitive to the geometrical structure of the metal center but also probes its effective charge. It turns out that the position of the edge (which can be evaluated by the edge inflection point) is shifted to higher energies when the formal valence of the photo-absorber increases. Below the absorption edge, the presence of pre-edge structures can be observed [44]. The occurrence of this peak in a metal (first raw transition metal) K-edge is due to 1s-3d electronic transition [45] that is electric-dipole forbidden but quadrupole allowed. Its intensity can be used as a probe for geometry, as the geometrical distortion of the metal core from centrosymmetric coordination favors the transition, while the energy position is relative to the metal core formal oxidation state. This fact is frequently used for investigating the charge associated to positive- and negative-electrode materials during reduction and oxidation reactions in batteries.

If we now consider the form of the absorption edge, it can be seen that it reflects the empty density of states and it strongly depends on the coordination, while the forms of the absorption traces up to 60–80 eV are due to the multiple scattering resonances of the ejected photoelectron. Several computer codes can simulate the XANES spectrum, such as above-mentioned FEFF, MXAN [46], FDMNES [47] and CTM4XAS [48], which are useful for the analysis of metal L-edges.

3. Investigating a battery at work: *ex situ* and *in situ (operando)* studies

The simplest way to study the structural end electronic modification of a cathode or anode material is by *ex situ* XAS. XANES and EXAFS spectra at a selected K-edge are collected at a specific state of charge (or discharge) of the battery. In this case, the battery is stopped at the chosen state of charge (or discharge) and disassembled; the recovered material, protected from air in adapted sample holders, is transported to a synchrotron to perform the experiment in a suitable XAS beamline [32]. Basically, two geometries are used for this purpose, namely transmission and fluorescence. In transmission geometry, the sample is placed between I_0 and I detectors and the absorption is measured according to the Beer's law exponential decay, as mentioned before. The fluorescence detection is carried out by tilting the sample at 45 degrees and collecting the fluorescence X-rays by using a solid-state detector at the right angle with respect to I_0.

Such *ex situ* XAS studies of electrode materials are now extensively completed by *operando* measurements, *i.e.*, performed during a discharge or charge process. Such an approach allows one to avoid several drawbacks due to the sample transfer needed for the *ex situ* measurements. Alteration of air- or moisture-sensitive species is avoided, as well as the occurrence of relaxation reactions which might show up when the electrical circuit is open,

inducing a transformation of the unstable cycled material [49]. The effects of sampling deviations are also eluded since the sample remains in the same position during the whole measurement series. Finally, the whole study can be performed on a single test cell suppressing the effects of uncontrolled differences in a set of cells which are needed for a stepwise *ex situ* study of the electrochemical mechanism. To perform such an experiment, a special *in situ* electrochemical cell, obeying to the specific requirements of XAS, has to be used. This cell consists of an electrode containing the active material, a lithium foil, a separator, which is typically a polymeric membrane such as Celgard, and an electrolyte, usually based on organic carbonate solvents such as propylene carbonate (PC), dimethyl carbonate (DMC) and ethylene carbonate (EC).

Figure 4 displays two different types of *in situ* electrochemical cells. The first one (left) is a typical pouch cell which is characterized by a large dimension of the cathode. In this case, a film containing the active material is previously deposited on a square Al (or Cu) current collector of 4 cm^2 and assembled in a glove box together with a Li (Na) counter-electrode, a separator and the electrolyte. The mass loading varies between 2 and 15 g/cm^2 of active material, depending on the energy of the X-ray. Sometimes, a small tube (visible in the right part of the cell) can be used as a sink for the gas, which may be released during the electrochemical processes and which can be analyzed in line, if necessary. The figure on the right displays a typical stainless steel cell [50], which uses self-supported films or pellets of electrode material of smaller dimension (1 cm diameter). The versatility of this second approach is testified by the successfully use of this cell in transmission and fluorescence geometry, as well as in other techniques including *in situ* XRD [51], Mössbauer [52] and Raman spectroscopy [53] measurements.

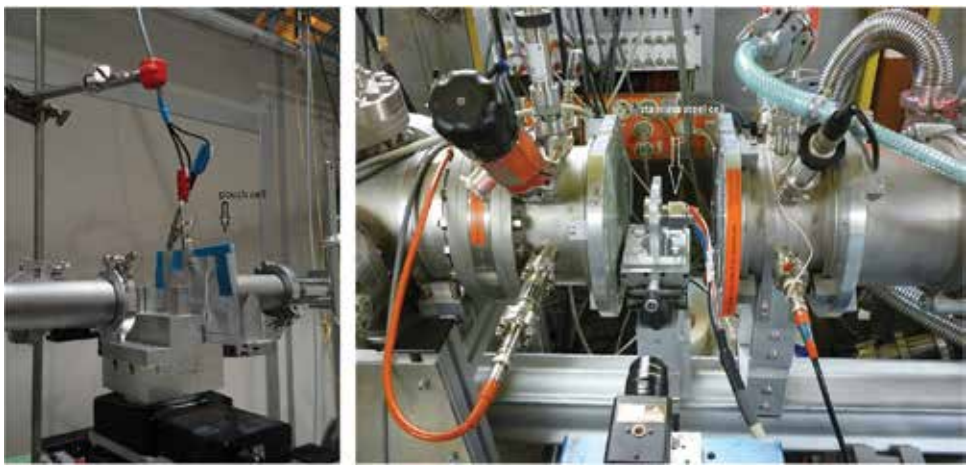

Figure 4. Typical *in situ* electrochemical cells used for *operando* XAS studies of batteries: A pouch cell (left) and a stainless steel cell (right) mounted on different XAS beamlines.

4. Case studies in battery materials

Given the large amount of physico-chemical information that it usually carries, already mentioned in the previous sections, XAS has been largely applied to the study of battery materials [18, 19]. A few particular case studies, specifying specific features of this technique in particular cases involving nanostructured species, are presented in the following paragraphs. It will be stressed, in particular, the importance of performing *in situ* studies compared to more simple, but also often less reliable, *ex situ* measurements.

4.1. *Ex situ* studies of lithium-excess manganese layered oxides

The relative abundance of manganese coupled with their variety of oxides structures, which provides generally a three-dimensional array of edge-shared MnO_6 octahedra for the lithium insertion and release, has aroused the interest of developing positive-electrode materials based on manganese oxide. Due to the well-known poor cycling capability of the spinel structure $LiMn_2O_4$, where a cooperative Jahn-Teller distortion of the Mn^{3+} ion causes a cubic-to-tetragonal phase transition leading to a rapid degradation of the electrode, an intensive research has been focused on alternative materials. Solid solutions of layered cathode materials such as the combination of Li_2MnO_3 and $LiMO_2$ (M = Mn, Co, Ni, etc.) have been proposed as promising candidates for cheaper, higher capacity and safer positive electrode for lithium batteries. However, the occurrence of an initial activation process during the first delithiation step (first charge) is always accompanied by a large irreversibility in terms of specific capacity. To gain a deeper understanding of the initial activation step and to study the following delithiation-lithiation process, an electronic and local structural characterization of the host material is required and the XAS is the technique of choice. A series of electrodes with different lithium concentration (state of charge, SOC) were studied in a series of lithium-rich, cobalt-poor $Li[Li_{0.2}Ni_{0.16}Mn_{0.56}Co_{0.08}]O_2$ electrode material (NMC), as an examples of *ex situ* XAS investigation [54, 55]. Due to the strong sensitivity of the XAS to the metal site, spectra at the three different metal edges can be measured, allowing the study of the evolution of the physico-chemical properties and of the local structure of each metal site.

Figure 5 shows the voltage profile of the cell during charge-discharge operation. The numbered points in the curve indicates predetermined states of charge (SOC) at which cells were prepared for the XAS measurements. **Figure 6** summarizes the XAS analysis conducted on the materials, where all the several portions of the X-ray absorption spectrum carry valuable information on the local and electronic structure: pre-edge, XANES and EXAFS. The pre-edge analysis (the Mn K-edge is displayed in the figure, showing two components) allowed the authors to check the variation of the Mn local site, in terms of symmetry and charge. XANES traces can provide the identification of the electroactive sites at different SOC and the EXAFS analyses the local structural information of the selected metal site. This information is complementary with respect to XRD which probes the long-range order in crystalline materials.

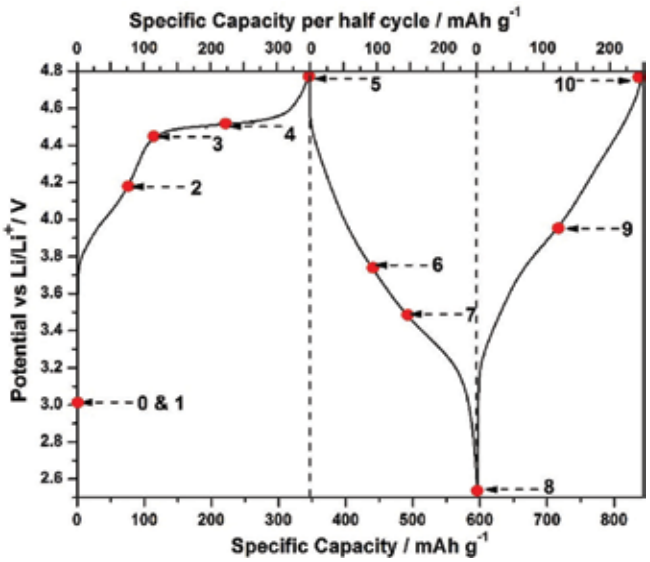

Figure 5. Voltage profile of two successive charge and discharge curves of Li-rich NCM at 20 mA/g. Representative points of 1–10 in the process of XAS measurements are indicated. Reference and counter electrode: Li. electrolyte: 1 M $LiPF_6$ in EC/DMC. Temperature: 20°C ± 2°C. On the upper X axis the capacity detected in each step is reported. Reproduced from Ref. [54].

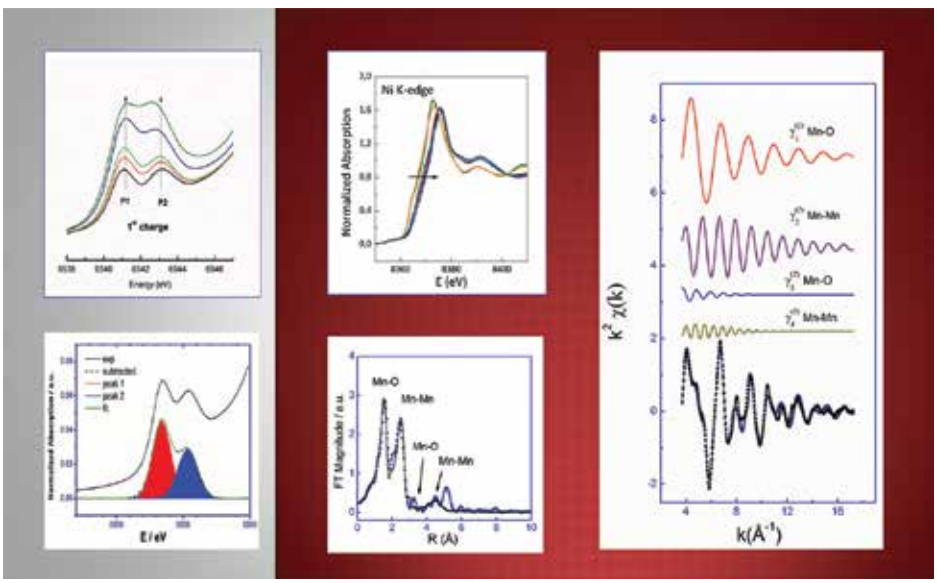

Figure 6. XAS data analysis for the cathode material. The picture displays analysis of the pre-edge data obtained at the Mn K-edge (left panel) including the fitting of the observed peaks (at the bottom). These data provide both charge and symmetry information around the investigated metal. Data at the right panel refer to XANES behavior at the Ni K-edge (up) and the best-fit of the EXAFS data in terms of single contribution to the total EXAFS oscillation (right). At the bottom the fourier transform (FT) behavior of the corresponding EXAFS is displayed. Reproduced from ELETTRA Highlights 2014–15, page 12.

The study here highlighted demonstrates that the manganese is not taking part of the initial electrochemical oxidation process, but a complete $Ni2^{+}/Ni^{4+}$ and a partial Co^{3+}/Co^{4+} redox processes occur during the first charge of the battery. The electrochemical performance of the material, considering the full and partial redox inactivity of Mn and Co, also reveals the participation of oxygen in the overall electrochemical redox process. Analysis of EXAFS at the three metal edges has revealed that the first charge of the lithium-rich cathode can be described by two separate reactions occurring at the two components, Li_2MnO_3 and $LiMO_2$: an activation of the Li_2MnO_3 component with a phase transition to an *hexagonal* layered structure and the oxidation/reduction of both Ni and Co which is not only demonstrated by pre-edge/XANES data but also corroborated by the first shell M-O distances behavior and their corresponding Debye-Waller factors.

4.2. Study of the conversion reaction in electrode materials: the case of $NiSb_2$

A particularly interesting case for the application of *operando* XAS is that of electrode materials undergoing a so-called conversion reaction, which was reviewed a few years ago by Cabana *et al.* [9]. In a conversion reaction, lithium reacts with a binary compound containing a transition metal (M = Ti, Mn, Fe, Co, Ni, etc.) and a group *p* element (X = O, P, Sb, Sn, etc.), according to the following equation:

$$M_a X_b + (b \cdot n)Li \leftrightarrows M + b \cdot Li_n X \tag{9}$$

Conversion reactions were first verified for transition metal oxides [56], but are rather common also for other chalcogenides, pnictogenides and carbon group semimetals. Conversion materials, *i.e.*, materials reacting through the conversion reaction allow reversible capacities as high as 1500 mAh/g, exceeding that of graphite (372 mAh/g), the negative electrode material commonly used in commercial Li-ion batteries. They have thus been considered as possible alternatives for the development of new high-energy storage devices. Recent studies have shown that, for conversion reactions, due to the formation of nanosized species, the composites obtained at the end of discharge are particularly unstable [49] and therefore the use of *operando* techniques for the study of reaction mechanisms is essential. Transition metal antimonides of general formula M_aSb_b form a family of conversion materials providing capacities between 450 and 600 mAh/g and can easily stand up to about 20 cycles at stable capacity before fading. The very large volume expansion (of about 300%) experienced during the reaction with lithium is probably at the origin of the rapid fading, causing the pulverization of the active material particles, with further degradation of the electronic wiring at high-rate and agglomeration of the active mass at low rate [57]. Several methods were used to improve the cycling life of antimonides such as nanostructuration of the electrodes [58], carbon coating and optimization of the formulation [59].

M_aSb_b compounds are expected to react with lithium by forming a matrix of Li_3Sb in which nanoparticles of the transition metal M are embedded. Actual reaction mechanisms, however, can be more complex and often dependent on the specific compound. For instance, several conversion pnictogenides, such as $FeSb_2$ [60] and MnSb [61], form intermediate lithiated insertion phases before starting the veritable conversion reaction, while additional phases could

also form throughout the whole electrochemical cycle. An example of a complicated reaction mechanism is that of $NiSb_2$, which reacts reversibly with lithium to form nickel metal and Li_3Sb providing a theoretical capacity of 532 mAh/g [62].

In this material, the possible formation of an intermediate ternary insertion solid solution was suggested by a slight shift of the XRD reflections during the first part of the discharge [62]. The complete amorphisation of the system during the conversion, however, made it impossible to follow the reaction by XRD. In particular, the formation of Ni nanoparticles at the end of discharge, which are expected for typical conversion reactions, could not be verified. *Operando* Ni K-edge XAS was thus used to address this issue [63].

The EXAFS data collected during the first discharge are shown in **Figure 7**. The fourier transform (FT) signal of pristine $NiSb_2$ exhibits a main contribution with a dominant peak at about 2.4 Å and a second smaller peak slightly below 2 Å, and a second contribution with a dominant peak at 4.2 Å. During lithiation, the first contribution is gradually replaced by a peak pointing at about 2.2 Å, while the peak at 4.2 Å gradually disappears. The spectrum of the fully lithiated material was fitted using 12 Ni neighbors at 2.47(1) Å. This result agrees well with the Ni − Ni distance of 2.491 Å in the *fcc* lattice of Ni metal. Such a fit, however, gives an amplitude reduction factor $S_0^2 = 0.34$, *i.e.*, less than half of the usually observed value. Since S_0^2 is directly correlated to the coordination number, such a low value indicates that the effective number of Ni neighbors is much smaller than 12, in line with the formation of Ni nanoparticles with a significant fraction of surface atoms. Such reduced coordination numbers are often observed for supported metal nanoparticles in heterogeneous catalysts with sizes below about 2 nm [64]. The nanosized nature of the Ni particles is also confirmed by the absence of the following coordination shells in the FT signal. The presence of Ni nanoparticles at the end of lithiation and their following (partial) reaction during delithiation to reform a nanosized form of $NiSb_2$, allowed the author to confirm that $NiSb_2$ is a veritable conversion material.

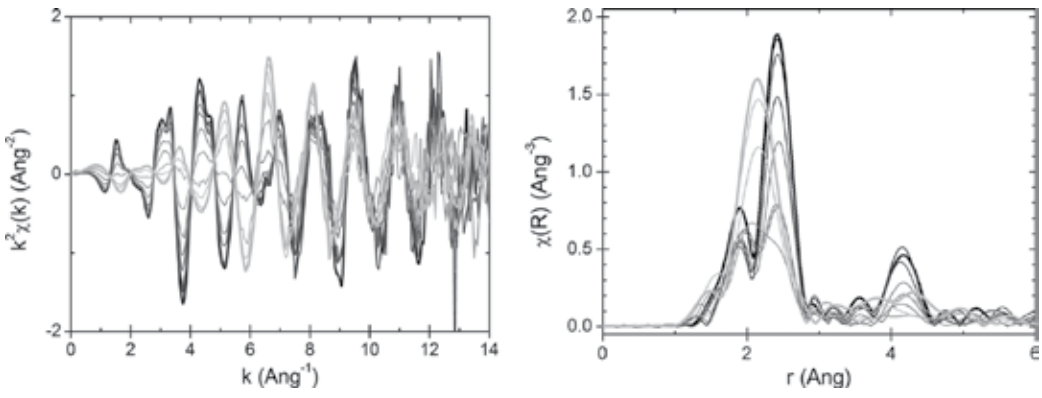

Figure 7. *Operando* evolution of the Ni K-edge EXAFS spectra (left) and corresponding phase-uncorrected FT signals (right) during the first galvanostatic lithiation of $NiSb_2$ vs. Li metal. Evolution with lithiation is shown on going from darker to brighter spectra (only selected spectra are shown for the sake of clearness). Reproduced from Ref. [63].

At the end of this paper, the authors compared the *operando* spectra with those of *ex situ* samples cycled vs. Li about 5 days prior to the XAS measurement campaign, which turned out to be rather different in spite of the precautions taken in order to avoid the decomposition of the latter materials. This comparison underlines the importance of performing *in situ* measurements to get a realistic view of the reaction mechanism of battery materials. In fact, especially in the case of conversion materials, such investigations can be very complex because the species formed in cycling electrodes are usually very reactive and/or unstable.

4.3. Study of Li-sulfur batteries by S K-edge XAS

One of the most interesting recent applications of XAS to electrochemical energy storage concerns the study of lithium-sulfur batteries (LSBs). Since the work of Jie *et al*. [65], many groups have developed first the use of XANES and more recently that of EXAFS for the study of such systems. In LSB, the positive electrode material is elemental sulfur, which can react with lithium to produce Li_2S for a theoretical capacity of 1672 mAh/g at about 2.5 V [66]. The practical capacity of such systems is unfortunately much lower, never exceeding 1200 mAh/g. Moreover, LSB suffer from several other drawbacks: the main one is surely the diffusion of polysulfides (Li_2S_n), produced during the first steps of the reduction of sulfur and highly soluble in the electrolyte, which cause the well-known "shuttle" phenomenon strongly limiting the capacity [67]. Second, solid Li_2S and elemental sulfur are both insulating and cannot be used as such in normal composite electrodes, fabricated as mixtures of sulfur and carbon powder on aluminum foil current collectors, since their continuous dissolution/precipitation during cycling gradually disconnects part of the active mass, making sulfur progressively electrochemically inactive [68, 69]. All these disadvantages cause rapid capacity fading and low columbic efficiency of LSB.

Several improvements have been suggested in the last years to tackle these drawbacks: one of them consisted in infiltrating molten sulfur into porous conductive carbon materials [70]. This approach, however, does not allow large sulfur loadings, nor does it prevent the diffusion of polysulfides outside the pores. Moreover, it requires large amounts of electrolyte to wet the large volume of porous carbon and to solubilize the polysulfides, which greatly reduces the volumetric energy density of LSB. Most recently, multifunctional positive electrodes, enhancing the sulfur loading and promoting the interaction of polysulfides with the electrode host to prevent their diffusion in the electrolyte have been successfully proposed and studied [71]. In all these studies, XAS has been largely used at different levels to investigate in detail the electrochemical mechanism and the diffusion (or retention) of polysulfides as well as the possible different failure paths.

Sulfur K-edge XANES, for instance, can be used as a semiquantitative analytical tool for LSB [72–81]. *Operando* XANES spectra fitted by linear combinations of reference XANES spectra of pure sulfur, synthetic polysulfides and Li_2S allowed following both the evolution of the sulfur species and of their relative ratio along the discharge and the charge process, as well as the variation of the concentration of sulfur in both the cathode and the electrolyte, in line with the diffusion of the polysulfides in the whole battery. More recently, it was also used for the detection of the formation of sulfur radical species [82–84], which were confirmed also by *operando* Raman spectroscopy [53].

A particularly interesting approach was, however, the application of EXAFS to the study of the electrochemical mechanism [85]. Such study was possible only due to the use of a specific sulfur-free electrolyte salt, which usually hindered the EXAFS contribution of the sulfur species evolving during cycling (cf. **Figure 8**). In this way, it was possible to clearly identify the type of polysulfides (long- or short-chain) formed in the electrode during the high-voltage and the low-voltage discharge plateaus and to confirm the formation of Li_2S only from the beginning of the low-voltage plateau and to follow its concentration in the electrode.

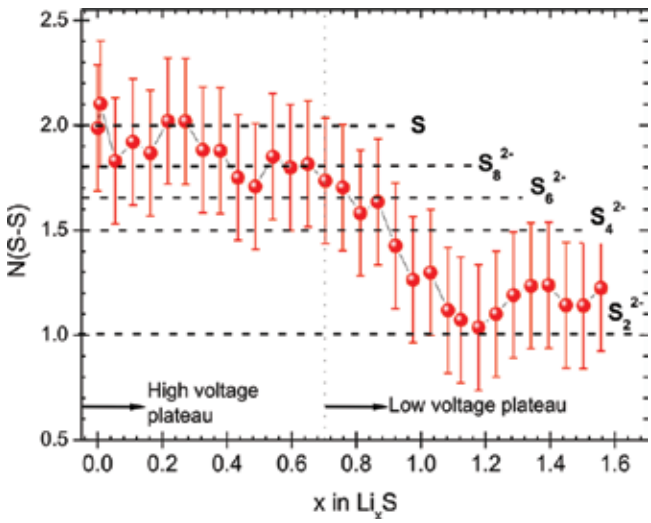

Figure 8. Variation of the average *S* coordination number during the first discharge. The average coordination of the most important polysulfides is reported for comparison. The vertical line represents the end of the high-voltage plateau. From Ref. [85].

Finally, XAS was very recently used for detecting the interaction of sulfur precursors with appropriately modified graphene oxide nanocomposites, leading to the immobilization of the sulfur species in the electrode, improving the overall cycling performance of the cell [86].

All these examples underlined the powerful properties of XAS for the *operando* study of electrochemical mechanisms in batteries even at low energies (sulfur K-edge is at only 2.47 keV).

5. The chemometric approach to the interpretation of XAS data

Due to the increasing performance of many synchrotron beamlines specialized in *in situ* XAS studies, extremely large dataset containing many tens or hundreds of spectra associates to a single experiment are currently collected. This huge amount of data is calling for a suitable strategy for their treatment in reasonable time. For instance, the study of the charge or the discharge process of a battery produces something like 100–300 spectra, depending on the experimental conditions (data acquisition protocol and battery discharge rate). In similar cases, the

use of chemometrics may be applied [87]. Specifically, the application of multivariate curve resolution (MCR) to large datasets of *in situ* XAS experiments (where the samples undergo continuous evolution during the reaction path) allows one to interpret their modification in terms of sums of pure spectra with variable concentration profiles, without needing any pre-existing model or *a priori* information about the system. To our knowledge, the first application of MRC to a XAS study of battery materials concerns the investigation of the evolution during charge of a positive electrode based on a $Cu_{0.1}V_2O_5$ xerogel [40]. This study, which is performed using the alternate least square (ALS) algorithm, allowed obtaining relevant information on the cell charging dynamics. In particular, the data treatment evidenced for the first time the occurrence of three species during the battery charging, which were further identified with a common EXAFS analysis. This successful chemometric approach to XAS has further been used for other *operando* studies, mostly by the catalysis community [88]. MCR was also applied to analyze XAS data from Fischer-Tropsch reaction [89] and to infer about the speciation and the evolution of ruthenium in Co − Ru/SiO2 systems by looking at quick-XAS data [90].

6. Perspectives

With the increasing demand of energy resources for both portable and storage purposes, there has been an extensive and increasingly diversification of materials and technology for the electrochemical power sources in the last five years. Not only lithium-ion technology but also sodium or even trivalent ions, also in aqueous media, are currently studied to obtain a good balancing between cost, safety, abundance and electrochemical performances. This chapter has underlined the strength of the XAFS probe to understand the dynamic of the both anode and cathode materials during the battery functioning, at atomic level. We feel that this core-level spectroscopy can even meet the increasing demand of deep understanding of different technologies and of new materials for batteries. This extraordinary versatility is due to: (i) the extremely selective local structure probe of XAS for the atomic species in crystalline, amorphous solid and liquid electrolyte; (ii) the unprecedented quality and speed of for data recording in synchrotron beamlines dedicated to *in situ* studies, coupled with a suitable and unbiased data analysis such as the chemometric approach to XAFS data presented above; (iii) the new generations of software for EXAFS data analysis, which are capable of analyzing multiple scattering contributions with great efficiency and to perform simultaneous multiple edge fits; (iv) the development of reliable spectrometers at synchrotron radiation light sources enabling high resolution recording, allowing the collection of complementary information with ancillary advanced techniques such as resonant inelastic X-ray scattering (RIXS) [91].

Moreover, new advanced synchrotron-based techniques are expected to be at the forefront of battery research in the future; among them, there will surely be X-ray transmission microscopy, which allows the simultaneous imaging and spatially resolved XAS study of electrode materials in batteries [92].

Finally, a personal consideration: in XAS, data analysis is usually considered as the bottleneck of the whole spectroscopic study. This holds true regardless of the simplicity or the difficulty of the oscillatory portion of the spectrum to be analyzed. Indeed, as long as a suitable struc-

tural model has not been established, an oscillation can be interpreted in several different ways. It is then recommended to newcomers not only to learn how to conduct XAS experiments, but also to perform appropriate data analyses by seeking the advice and collaboration of experts who are willing to share their knowledge and their experience.

Acknowledgements

Work supported by RFO funding (University of Bologna). Thanks are due to staff at both Sincrotrone Trieste and Synchrotron SOLEIL for assistance during the experiments and for providing synchrotron radiation.

Author details

Marco Giorgetti[1]* and Lorenzo Stievano[2]

*Address all correspondence to: marco.giorgetti@unibo.it

1 Department of Industrial Chemistry "Toso Montanari", University of Bologna, Bologna, Italy

2 Institut Charles Gerhardt – AIME, University of Montpellier, Montpellier, France

References

[1] Dunn, B., Kamath, H., Tarascon, J.-M.: Electrical Energy Storage for the Grid: A Battery of Choices. Science. 334, 928–935 (2011).

[2] Vincent, C.A., Scrosati, B.: Modern Batteries—An Introduction to Electrochemical Power Sources—2nd Edition. Butterworth-Heinemann, Oxford, UK (1997).

[3] Wagemaker, M., Mulder, F.M.: Properties and Promises of Nanosized Insertion Materials for Li-Ion Batteries. Acc. Chem. Res. 46, 1206–1215 (2013).

[4] Masquelier, C., Croguennec, L.: Polyanionic (Phosphates, Silicates, Sulfates) Frameworks as Electrode Materials for Rechargeable Li (or Na) Batteries. Chem. Rev. 113, 6552–6591 (2013).

[5] Whittingham, M.S.: Lithium Batteries and Cathode Materials. Chem. Rev. 104, 4271–4302 (2004).

[6] Obrovac, M.N., Chevrier, V.L.: Alloy Negative Electrodes for Li-Ion Batteries. Chem. Rev. 114, 11444–11502 (2014).

[7] Kim, H., Jeong, G., Kim, Y.-U., Kim, J.-H., Park, C.-M., Sohn, H.-J.: Metallic Anodes for Next Generation Secondary Batteries. Chem. Soc. Rev. 42, 9011–9034 (2013).

[8] Park, C.-M., Kim, J.-H., Kim, H., Sohn, H.-J.: Li-Alloy Based Anode Materials for Li Secondary Batteries. Chem. Soc. Rev. 39, 3115–3141 (2010).

[9] Cabana, J., Monconduit, L., Larcher, D., Palacín, M.R.: Beyond Intercalation-Based Li-Ion Batteries: The State of the Art and Challenges of Electrode Materials Reacting Through Conversion Reactions. Adv. Mater. 22, E170–E192 (2010).

[10] Peled, E.: The Electrochemical Behavior of Alkali and Alkaline Earth Metals in Nonaqueous Battery Systems—The Solid Electrolyte Interphase Model. J. Electrochem. Soc. 126, 2047–2051 (1979).

[11] Sharma, N., Pang, W.K., Guo, Z., Peterson, V.K.: In Situ Powder Diffraction Studies of Electrode Materials in Rechargeable Batteries. ChemSusChem. 8, 2826–2853 (2015).

[12] Li, J.-T., Zhou, Z.-Y., Broadwell, I., Sun, S.: In-Situ Infrared Spectroscopic Studies of Electrochemical Energy Conversion and Storage. Acc. Chem. Res. 45, 485–494 (2012).

[13] Baddour-Hadjean, R., Pereira-Ramos, J.-P.: Raman Microspectrometry Applied to the Study of Electrode Materials for Lithium Batteries. Chem. Rev. 110, 1278–1319 (2010).

[14] Lippens, P.-E., Jumas, J.-C.: Mössbauer Spectroscopy Investigation of Batteries. Mössbauer Eff. Ref. Data J. 33, 31 (2010).

[15] Martha, S.K., Markevich, E., Burgel, V., Salitra, G., Zinigrad, E., Markovsky, B., Sclar, H., Pramovich, Z., Heik, O., Aurbach, D., Exnar, I., Buqa, H., Drezen, T., Semrau, G., Schmidt, M., Kovacheva, D., Saliyski, N.: A Short Review on Surface Chemical Aspects of Li Batteries: A Key for a Good Performance. J. Power Sources. 189, 288–296 (2009).

[16] Verma, P., Maire, P., Novák, P.: A Review of the Features and Analyses of the Solid Electrolyte Interphase in Li-Ion Batteries. Electrochim. Acta. 55, 6332–6341 (2010).

[17] McBreen, J., O'Grady, W.E., Pandya, K.I.: EXAFS: A New Tool for the Study of Battery and Fuel Cell Materials. J. Power Sources. 22, 323–340 (1988).

[18] Giorgetti, M.: A Review on the Structural Studies of Batteries and Host Materials by X-Ray Absorption Spectroscopy. ISRN Mater. Sci. 2013, 938625 (2013).

[19] Shearing, P., Wu, Y., Harris, S.J., Brandon, N.: In Situ X-Ray Spectroscopy and Imaging of Battery Materials. Electrochem. Soc. Interface. 20, 43–47 (2011).

[20] Croy, J.R., Balasubramanian, M., Kim, D., Kang, S.-H., Thackeray, M.M.: Designing High-Capacity, Lithium-Ion Cathodes Using X-ray Absorption Spectroscopy. Chem. Mater. 23, 5415–5424 (2011).

[21] Balasubramanian, M., Sun, X., Yang, X.Q., McBreen, J.: In Situ X-Ray Diffraction and X-Ray Absorption Studies of High-Rate Lithium-Ion Batteries. J. Power Sources. 92, 1–8 (2001).

[22] Filipponi, A.: EXAFS for liquids. J. Physi.: Condens. Matter. 13, R23–R60 (2001).

[23] Niemantsverdriet, J.W.: Spectroscopy in Catalysis. Wiley-VCH, Weinheim (1995).

[24] Nelson, R.C., Miller, J.T.: An Introduction to X-Ray Absorption Spectroscopy and its In Situ Application to Organometallic Compounds and Homogeneous Catalysts. Catal. Sci. Technol. 2, 461–470 (2012).

[25] Carrier, X., Marceau, E., Carabineiro, H., Rodríguez-González, V., Che, M.: EXAFS Spectroscopy as a Tool to Probe Metal–Support Interaction and Surface Molecular Structures in Oxide-Supported Catalysts: Application to Al_2O_3-Supported Ni(II) Complexes and ZrO_2-Supported Tungstates. Phys. Chem. Chem. Phys. 11, 7527–7539 (2009).

[26] Ascone, I., Fourme, R., Hasnain, S.S.: Introductory Overview: X-Ray Absorption Spectroscopy and Structural Genomics. J. Synchrotron Radiat. 10, 1–3 (2003).

[27] Solomon, E.I.: Synchrotron Radiation in Inorganic and Bioinorganic Chemistry: Preface. Coord. Chem. Rev. 249, 1–2 (2005).

[28] Dewald, H.D.: Use of EXAFS to Probe Electrode-Solution Interfaces. Electroanal. 3, 145–155 (1991).

[29] Teo, B.K.: EXAFS: Basic Principles and Data Analysis. Springer Berlin-Heidelberg, Berlin, Heidelberg, Germany (1986).

[30] Koningsberger, D.C., Prins, R.: X-Ray Absorption : Principles, Applications, Techniques of EXAFS, SEXAFS, and XANES. Wiley Interscience, New York, USA (1988).

[31] van Bokhoven, J.A., Lamberti, C.: X-Ray Absorption and X-Ray Emission Spectroscopy : Theory and Applications. John Wiley & Sons Ltd., Chichester, UK (2016).

[32] Bunker, G.: Introduction to XAFS, A Practical Guide to X-Ray Absorption Fine Structure Spectroscopy. Cambridge University Press, Cambridge, UK (2010).

[33] Filipponi, A., Di Cicco, A.: X-Ray-Absorption Spectroscopy and N-Body Distribution Functions in Condensed Matter. II. Data Analysis and Applications. Phys. Rev. B. 52, 15135–15149 (1995).

[34] Ankudinov, A.L., Ravel, B., Rehr, J.J., Conradson, S.D.: Real-Space Multiple-Scattering Calculation and Interpretation of X-Ray-Absorption Near-Edge Structure. Phys. Rev. B. 58, 7565–7576 (1998).

[35] Rehr, J.J., Kas, J.J., Vila, F.D., Prange, M.P., Jorissen, K.: Parameter-Free Calculations of X-Ray Spectra with FEFF9. Phys. Chem. Chem. Phys. 12, 5503–5513 (2010).

[36] Tomic, S., Searle, B.G., Wander, A., Harrison, N.M., Dent, A.J., Mosselmans, J.F.W., Inglesfield, J.E.: New Tools for the Analysis of EXAFS: The DL EXCURV Package. (2004).

[37] Newville, M.: IFEFFIT : Interactive XAFS Analysis and FEFF Fitting. J. Synchrotron Radiat. 8, 322–324 (2001).

[38] Ravel, B., Newville, M.: ATHENA, ARTEMIS, HEPHAESTUS: Data analysis for X-Ray Absorption Spectroscopy Using IFEFFIT. J. Synchrotron Radiat. 12, 537–541 (2005).

[39] Giorgetti, M., Aquilanti, G., Ballarin, B., Berrettoni, M., Cassani, M.C., Fazzini, S., Nanni, D., Tonelli, D.: Speciation of Gold Nanoparticles by Ex Situ Extended X-ray Absorption Fine Structure and X-Ray Absorption Near Edge Structure. Anal. Chem. 88, 6873–6880 (2016).

[40] Conti, P., Zamponi, S., Giorgetti, M., Berrettoni, M., Smyrl, W.H.: Multivariate Curve Resolution Analysis for Interpretation of Dynamic Cu K-Edge X-Ray Absorption Spectroscopy Spectra for a Cu Doped V_2O_5 Lithium Battery. Anal. Chem. 82, 3629–3635 (2010).

[41] Boscherini, F.: Applications of XAFS to Nanostructures and Materials Science. In: Settimio Mobilio, Federico Boscherini, C.M. (ed.) Synchrotron Radiation. pp. 485–498. Springer Berlin-Heidelberg, Berlin, Heidelberg (2015).

[42] Guda, A.A., Soldatov, M.A., Soldatov, A. V.: Group III–V and II–VI Quantum Dots and Nanoparticles. In: Schnohr, C.S. and Ridgway, M.C. (eds.) X-Ray Absorption Spectroscopy of Semiconductors. pp. 247–268. Springer Berlin-Heidelberg, Berlin, Germany (2015).

[43] Frenkel, A.I., Hills, C.W., Nuzzo, R.G.: A View from the Inside: Complexity in the Atomic Scale Ordering of Supported Metal Nanoparticles. J. Phys. Chem. B. 105, 12689–12703 (2001).

[44] de Groot, F., Vankó, G., Glatzel, P.: The 1s X-Ray Absorption Pre-Edge Structures in Transition Metal Oxides. J. Phys. Condens. Matter. 21, 104207 (2009).

[45] Westre, T.E., Kennepohl, P., DeWitt, J.G., Hedman, B., Hodgson, K.O., Solomon, E.I.: A Multiplet Analysis of Fe K-Edge 1s → 3d Pre-Edge Features of Iron Complexes. J. Am. Chem. Soc. 119, 6297–6314 (1997).

[46] Benfatto, M., Della Longa, S., Natoli, C.R.: The MXAN procedure: a new method for analysing the XANES spectra of metalloproteins to obtain structural quantitative information. J. Synchrotron Radiat. 10, 51–57 (2003).

[47] Joly, Y.: X-Ray Absorption Near-Edge Structure Calculations Beyond the Muffin-Tin Approximation. Phys. Rev. B. 63, 125120 (2001).

[48] Stavitski, E., de Groot, F.M.F.: The CTM4XAS Program for EELS and XAS Spectral Shape Analysis of Transition Metal L Edges. Micron. 41, 687–694 (2010).

[49] Johnston, K.E., Sougrati, M.T., Stievano, L., Darwiche, A., Dupré, N., Grey, C.P., Monconduit, L.: Effects of Relaxation on Conversion Negative Electrode Materials for Li-Ion Batteries: A Study of TiSnSb Using 119 Sn Mössbauer and 7 Li MAS NMR Spectroscopies. Chem. Mater. 28, 4032–4041 (2016).

[50] Leriche, J.-B., Hamelet, S., Shu, J., Morcrette, M., Masquelier, C., Ouvrard, G., Zerrouki, M., Soudan, P., Belin, S., Elkaïm, E., Baudelet, F.: An Electrochemical Cell for Operando Study of Lithium Batteries Using Synchrotron Radiation. J. Electrochem. Soc. 157, A606–A610 (2010).

[51] Conte, D.E., Mouyane, M., Stievano, L., Fraisse, B., Sougrati, M.T., Olivier-Fourcade, J., Willmann, P., Jordy, C., Artus, M., Cassaignon, S., Driezen, K., Jumas, J.-C.: A Combined Mössbauer Spectroscopy and X-Ray Diffraction Operando Study of Sn-Based Composite Anode Materials for Li-Ion Accumulators. J. Solid State Electrochem. 16, 3837–3848 (2012).

[52] Sougrati, M.T., Fullenwarth, J., Debenedetti, A., Fraisse, B., Jumas, J.-C., Monconduit, L.: TiSnSb a New Efficient Negative Electrode for Li-Ion Batteries: Mechanism Investigations by Operando-XRD and Mössbauer Techniques. J. Mater. Chem. 21, 10069–10076 (2011).

[53] Hannauer, J., Scheers, J., Fullenwarth, J., Fraisse, B., Stievano, L., Johansson, P.: The Quest for Polysulfides in Lithium-Sulfur Battery Electrolytes: An Operando Confocal Raman Spectroscopy Study. ChemPhysChem. 16, 2755–2759 (2015).

[54] Buchholz, D., Li, J., Passerini, S., Aquilanti, G., Wang, D., Giorgetti, M., Capacity, H.: X-Ray Absorption Spectroscopy Investigation of Lithium-Rich, Cobalt-Poor Layered-Oxide Cathode Material with High Capacity. ChemElectroChem. 2, 85–97 (2015).

[55] Giorgetti, M., Wang, D., Aquilanti, G., Buchholz, D., Passerini, S.: Local Structure Modification in Lithium Rich Layered Li-Mn-O Cathode Material. J. Phys.: Conf. Ser. 712, 12130 (2016).

[56] Poizot, P., Laruelle, S., Grugeon, S., Dupont, L., Tarascon, J.-M.: Nano-Sized Transition-Metal Oxides as Negative-Electrode Materials for Lithium-Ion Batteries. Nature. 407, 496–499 (2000).

[57] Marino, C., Fullenwarth, J., Monconduit, L., Lestriez, B.: Diagnostic of the Failure Mechanism in $NiSb_2$ Electrode for Li Battery through Analysis of its Polarization on Galvanostatic Cycling. Electrochim. Acta. 78, 177–182 (2012).

[58] Villevieille, C., Ionica-Bousquet, C.M., De Benedetti, A., Morato, F., Pierson, J.-F., Simon, P., Monconduit, L.: Self Supported Nickel Antimonides Based Electrodes for Li Ion Battery. Solid State Ionics. 192, 298–303 (2011).

[59] Sivasankaran, V., Marino, C., Chamas, M., Soudan, P., Guyomard, D., Jumas, J.-C., Lippens, P.-E., Monconduit, L., Lestriez, B.: Improvement of Intermetallics Electrochemical Behavior by Playing With the Composite Electrode Formulation. J. Mater. Chem. 21, 5076–5082 (2011).

[60] Villevieille, C., Fraisse, B., Womes, M., Jumas, J.-C., Monconduit, L.: A New Ternary Li_4FeSb_2 Structure Formed upon Discharge of the $FeSb_2$/Li Cell. J. Power Sources. 189, 324–330 (2009).

[61] Fransson, L.M.L., Vaughey, J.T., Edström, K., Thackeray, M.M.: Structural Transformations in Intermetallic Electrodes for Lithium Batteries. J. Electrochem. Soc. 150, A86 (2003).

[62] Villevieille, C., Ionica-Bousquet, C.M., Ducourant, B., Jumas, J.-C., Monconduit, L.: $NiSb_2$ as Negative Electrode for Li-Ion Batteries: An Original Conversion Reaction. J. Power Sources. 172, 388–394 (2007).

[63] Marino, C., Fraisse, B., Womes, M., Villevieille, C., Monconduit, L., Stievano, L.: At the Heart of a Conversion Reaction: An Operando X-Ray Absorption Spectroscopy Investigation of $NiSb_2$, a Negative Electrode Material for Li-Ion Batteries. J. Phys. Chem. C. 118, 27772–27780 (2014).

[64] Greegor, R.B., Lytle, F.W.: Morphology of supported metal clusters: Determination by EXAFS and chemisorption. J. Catal. 63, 476–486 (1980).

[65] Gao, J., Lowe, M.A., Kiya, Y., Abruña, H.D.: The Effects of Liquid Electrolytes on the Charge-Discharge Performance of Rechargeable Lithium/Sulfur Batteries: Electrochemical and In-Situ X-Ray Absorption Spectroscopic Studies. J. Phys. Chem. C. 115, 25132–25137 (2011).

[66] Bruce, P.G., Freunberger, S.A., Hardwick, L.J., Tarascon, J.-M.: Li–O_2 and Li–S Batteries with High Energy Storage. Nat. Mater. 11, 19–29 (2011).

[67] Mikhaylik, Y.V., Akridge, J.R.: Low Temperature Performance of Li/S Batteries. J. Electrochem. Soc. 150, A306–A311 (2003).

[68] Cheon, S.-E., Ko, K.-S., Cho, J.-H., Kim, S.-W., Chin, E.-Y., Kim, H.-T.: Rechargeable Lithium Sulfur Battery: I. Structural Change of Sulfur Cathode During Discharge and Charge. J. Electrochem. Soc. 150, A796–A799 (2003).

[69] Cheon, S.-E., Ko, K.-S., Cho, J.-H., Kim, S.-W., Chin, E.-Y., Kim, H.-T.: Rechargeable Lithium Sulfur Battery: II. Rate Capability and Cycle Characteristics. J. Electrochem. Soc. 150, A800–A805 (2003).

[70] Choi, N.-S., Chen, Z., Freunberger, S.A., Ji, X., Sun, Y.-K., Amine, K., Yushin, G., Nazar, L.F., Cho, J., Bruce, P.G.: Challenges Facing Lithium Batteries and Electrical Double-Layer Capacitors. Angew. Chem. Int. Ed. 51, 9994–10024 (2012).

[71] Pang, Q., Liang, X., Kwok, C.Y., Nazar, L.F.: Advances in Lithium–Sulfur Batteries Based on Multifunctional Cathodes and Electrolytes. Nat. Energy. 1, 16132 (2016).

[72] Patel, M.U.M., Arčon, I., Aquilanti, G., Stievano, L., Mali, G., Dominko, R.: X-Ray Absorption Near-Edge Structure and Nuclear Magnetic Resonance Study of the Lithium-Sulfur Battery and its Components. ChemPhysChem. 15, 894–904 (2014).

[73] Cuisinier, M., Cabelguen, P.-E., Evers, S., He, G., Kolbeck, M., Garsuch, A., Bolin, T., Balasubramanian, M., Nazar, L.F.: Sulfur Speciation in Li–S Batteries Determined by Operando X-ray Absorption Spectroscopy. J. Phys. Chem. Lett. 4, 3227–3232 (2013).

[74] Pascal, T.A., Wujcik, K.H., Velasco-Velez, J., Wu, C., Teran, A.A., Kapilashrami, M., Cabana, J., Guo, J., Salmeron, M., Balsara, N., Prendergast, D.: X-ray Absorption Spectra of Dissolved Polysulfides in Lithium–Sulfur Batteries from First-Principles. J. Phys. Chem. Lett. 5, 1547–1551 (2014).

[75] Cuisinier, M., Cabelguen, P.-E., Adams, B.D., Garsuch, A., Balasubramanian, M., Nazar, L.F.: Unique Behaviour of Nonsolvents for Polysulphides in Lithium–Sulphur Batteries. Energy Environ. Sci. 7, 2697–2705 (2014).

[76] Lowe, M.A., Gao, J., Abruña, H.D.: Mechanistic Insights into Operational Lithium–Sulfur Batteries by In Situ X-Ray Diffraction and Absorption Spectroscopy. RSC Adv. 4, 18347–18353 (2014).

[77] Yu, X., Pan, H., Zhou, Y., Northrup, P., Xiao, J., Bak, S., Liu, M., Nam, K.-W., Qu, D., Liu, J., Wu, T., Yang, X.-Q.: Direct Observation of the Redistribution of Sulfur and Polysulfides in Li-S Batteries During the First Cycle by In Situ X-Ray Fluorescence Microscopy. Adv. Energy Mater. 5, 1500072 (2015).

[78] Pang, Q., Kundu, D., Cuisinier, M., Nazar, L.F.: Surface-Enhanced Redox Chemistry of Polysulphides on a Metallic and Polar Host for Lithium-Sulphur Batteries. Nat. Commun. 5, 4759 (2014).

[79] Vijayakumar, M., Govind, N., Walter, E., Burton, S.D., Shukla, A., Devaraj, A., Xiao, J., Liu, J., Wang, C., Karim, A., Thevuthasan, S.: Molecular Structure and Stability of Dissolved Lithium Polysulfide Species. Phys. Chem. Chem. Phys. 16, 10923–10932 (2014).

[80] Zhu, P., Song, J., Lv, D., Wang, D., Jaye, C., Fischer, D.A., Wu, T., Chen, Y.: Mechanism of Enhanced Carbon Cathode Performance by Nitrogen Doping in Lithium–Sulfur Battery: An X-Ray Absorption Spectroscopic Study. J. Phys. Chem. C. 118, 7765–7771 (2014).

[81] Gorlin, Y., Siebel, A., Piana, M., Huthwelker, T., Jha, H., Monsch, G., Kraus, F., Gasteiger, H.A., Tromp, M.: Operando Characterization of Intermediates Produced in a Lithium-Sulfur Battery. J. Electrochem. Soc. 162, A1146–A1155 (2015).

[82] Pascal, T.A., Pemmaraju, C.D., Prendergast, D.: X-Ray Spectroscopy as a Probe for Lithium Polysulfide Radicals. Phys. Chem. Chem. Phys. 17, 7743–7753 (2015).

[83] Wujcik, K.H., Pascal, T.A., Pemmaraju, C.D., Devaux, D., Stolte, W.C., Balsara, N.P., Prendergast, D.: Characterization of Polysulfide Radicals Present in an Ether-Based Electrolyte of a Lithium-Sulfur Battery During Initial Discharge Using In Situ X-Ray Absorption Spectroscopy Experiments and First-Principles Calculations. Adv. Energy Mater. 5, 1500285 (2015).

[84] Cuisinier, M., Hart, C., Balasubramanian, M., Garsuch, A., Nazar, L.F.: Radical or Not Radical : Revisiting Lithium—Sulfur Electrochemistry in Nonaqueous Electrolytes. Adv. Energy Mater. 5, 1401801 (2015).

[85] Dominko, R., Patel, M.U.M., Lapornik, V., Vizintin, A., Koželj, M., Novak Tušar, N., Arcon, I., Stievano, L., Aquilanti, G.: Analytical Detection of Polysulfides in the Presence of Adsorption Additives by Operando X-Ray Absorption Spectroscopy. J. Phys. Chem. C. 119, 19001–19010 (2015).

[86] Ye, Y., Kawase, A., Song, M.-K., Feng, B., Liu, Y.-S., Marcus, M.A., Feng, J., Fang, H., Cairns, E.J., Zhu, J., Guo, J.: X-Ray Absorption Spectroscopic Characterization of the Synthesis Process: Revealing the Interactions in Cetyltrimethylammonium Bromide-Modified Sulfur–Graphene Oxide Nanocomposites. J. Phys. Chem. C. 120, 10111–10117 (2016).

[87] de Juan, A., Jaumot, J., Tauler, R.: Multivariate Curve Resolution (MCR). Solving the Mixture Analysis Problem. Anal. Methods. 6, 4964 (2014).

[88] Cassinelli, W.H., Martins, L., Passos, A.R., Pulcinelli, S.H., Santilli, C. V., Rochet, A., Briois, V.: Multivariate curve resolution analysis applied to time-resolved synchrotron X-ray Absorption Spectroscopy monitoring of the activation of copper alumina catalyst. Catal. Today. 229, 114–122 (2014).

[89] Voronov, A., Urakawa, A., van Beek, W., Tsakoumis, N.E., Emerich, H., Rønning, M.: Multivariate Curve Resolution Applied to In Situ X-Ray Absorption Spectroscopy Data: An Efficient Tool for Data Processing and Analysis. Anal. Chim. Acta. 840, 20–27 (2014).

[90] Hong, J., Marceau, E., Khodakov, A.Y., Gaberová, L., Griboval-Constant, A., Girardon, J.-S., La Fontaine, C., Briois, V.: Speciation of Ruthenium as a Reduction Promoter of Silica-Supported Co Catalysts: A Time-Resolved In Situ XAS Investigation. ACS Catal. 5, 1273–1282 (2015).

[91] Ament, L.J.P., van Veenendaal, M., Devereaux, T.P., Hill, J.P., van den Brink, J.: Resonant Inelastic X-Ray Scattering Studies of Elementary Excitations. Rev. Mod. Phys. 83, 705–767 (2011).

[92] Olivares-Marín, M., Sorrentino, A., Lee, R.-C., Pereiro, E., Wu, N.-L., Tonti, D.: Spatial Distributions of Discharged Products of Lithium-Oxygen Batteries Revealed by Synchrotron X-ray Transmission Microscopy. Nano Lett. 15, 6932–6938 (2015).

Chapter 5

Synchrotron Radiation-Based X-Ray Study on Energy Storage Materials

Shoaib Muhammad, Hyunchul Kim and
Won-Sub Yoon

Additional information is available at the end of the chapter

http://dx.doi.org/10.5772/67029

Abstract

Understanding the electrochemical processes responsible for energy storage in batteries is critical for designing of next-generation batteries. The conventional laboratory-scale characterization instruments provide limited information required for better understanding of electrochemical reaction mechanisms. Synchrotron radiations have very high brilliance and broad energy range extending from far-IR through the hard X-ray region. The availability of synchrotron radiation is driving technical and theoretical advances in scattering and spectroscopic techniques from last couple of decades. These advances in synchrotron radiation-based characterization techniques have made it possible to study the underpinning issues of energy storage materials. An electrochemical road map based on much more knowledge-driven approach can be drawn by utilizing synchrotron-based element-specific spectroscopic as well as scattering techniques. Herein, we introduce various scenarios where synchrotron radiation-based characterization methods provide inherent advantages and flexibility in obtaining detailed mechanistic information along with structural studies.

Keywords: synchrotron radiation, energy storage material, Li-ion battery, XRD, nanostructures, XAS, local structure

1. Introduction

Synchrotron radiation is emitted by charged particles, traveling at speeds relative to the speed of light when accelerated by magnetic fields. The major advantages of synchrotron radiation include very high intensity, tunable energy range, and inherently linear polarization [1]. However, one major drawback is the limited availability of the national and international

synchrotron radiation facilities. The availability of synchrotron radiation, with its characteristics of high brilliance, particular collimation, and multi-wavelength accessibility, continues to drive technical and theoretical advances in scattering and spectroscopy techniques. An exciting area being developed is the exploitation of these advances in synchrotron radiation surface and bulk-specific probe techniques to study the underpinning issues of energy storage materials.

The long-term endurance of batteries and other electrochemical devices, used in highly demanding applications like electric vehicles, is closely related to the ability of the cathode and anode materials to accommodate and release guest ions without any structural damage. A challenge in developing the understanding of energy storage process in batteries is in the direct study of the electrochemical reactions involved during battery operation. The characterization tool required needs to provide element-specific as well as overall structural information with high resolution. Synchrotron radiation-based measurements under operating conditions of batteries are critical in order to map the mechanistic causality between the local and atomic structure of functional components of batteries and their electrochemical characteristics. In this chapter, we will examine various scenarios where synchrotron radiation-based X-ray methods provide inherent advantages and flexibility in obtaining detailed mechanistic information along with structural studies.

2. Synchrotron radiation-based X-ray scattering techniques

2.1. Wide-angle X-ray scattering (WAXS)

X-ray photons interact with matter in different ways including coherent scattering, Compton scattering, photoelectric interaction, and pair production. If the interaction of the X-ray photons is coherent and elastic, the interaction is called X-ray diffraction (XRD) or Bragg scattering. A distribution of electrons in matter will interact with a photon wave to produce an interference-modulated scattering pattern, called a diffraction pattern. If multiple identical electron distributions are periodically placed in space, the scattering from each of them will interact with that from the others and will result in destructive interference in most of the direction other than a few allowed directions. These allowed directions can be calculated by considering the lattice, and hence a crystalline structure can be fully resolved by using diffraction pattern. Bragg's law is a useful model to describe the relation between the allowed scattering angles (2θ), the photon wavelength (λ), and an inter-planar distance (d) between parallel planes; see Eq. (1):

$$2d \sin\theta = n\lambda \tag{1}$$

The recorded diffraction peak from a sample will have an angular width due to the broadening from the instrument. Additionally, the peaks can be broadened by the finite size of the crystallites. The peak broadening does not correlate with the particle size, but with the coherent domain length where long-range order is preserved [2]. Synchrotron radiation covers a large range of energies and that allows for superior data acquisition. In the case of XRD, it enables

http://dx.doi.org/10.5772/67029

the ability to probe many different crystallographic planes at the same time, resulting in fast and rich data acquisition. The use of high energy, sometimes referred to as hard X-rays, is advantageous because these X-rays are not absorbed well in a solid material and therefore allow for deep penetration. These properties of synchrotron radiation, coupled with overall high intensities, allow for rich data collection and experimentation that were previously not possible. Experimental setup for synchrotron radiation-based high-energy XRD is shown in **Figure 1**. As the high-energy photons are able to fully penetrate the cell, these measurements are conducted in the transmission mode in order to obtain 2D diffraction patterns. This also means that the cathode and anode can be investigated simultaneously.

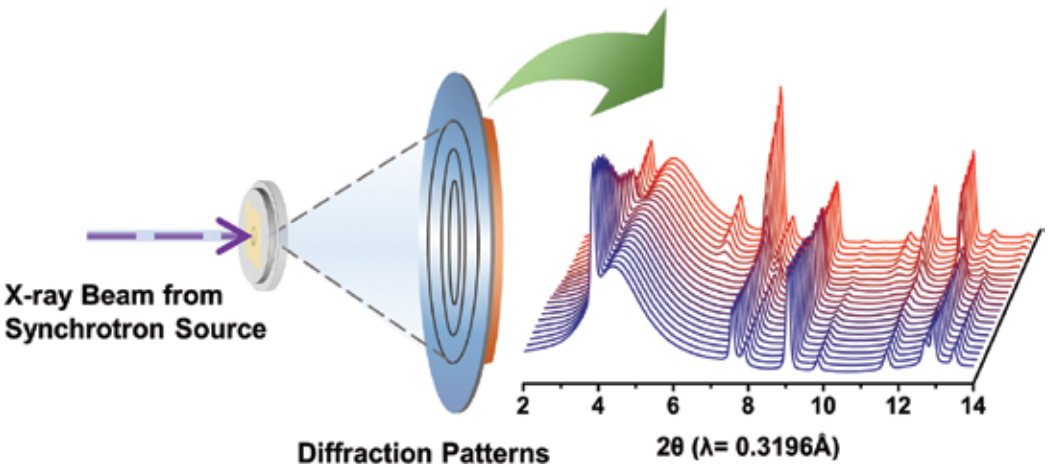

Figure 1. Schematic diagram of synchrotron radiation-based X-ray scattering technique.

2.1.1. Case study

Rechargeable Li-ion batteries are electrochemical energy storage devices of choice in portable electronics due to their high-specific energy density and now becoming increasingly popular for grid storage and electrical vehicles. In Li-ion battery, electrodes operate by reversible Li-ion insertion and extraction during charge and discharge. High-rate Li-ion battery electrode materials usually make solid solutions with Li over a large composition range in order to avoid phase transformation during (de)lithiation. Phase transformations, during cycling, are associated with small or negligible volume changes. For example, the layered compound $LiNi_{1/3}Mn_{1/3}Co_{1/3}O_2$ makes a solid solution and shows moderate volume changes; however, the high-voltage spinel $Li_x(Ni_{0.5}Mn_{1.5})O_4$ ($0 < x < 1$) shows only a small volume change (3%) for the two-phase region [3]. $LiFePO_4$, however, displays excellent high-rate performance when nanosized, despite undergoing a two-phase transformation to $FePO_4$ during delithiation, along with small volume change of 6.8% [4]. The limited Li solubility in $LiFePO_4$ and $FePO_4$ indicates that (de)lithiation occurs via a two-phase reaction, where the relative $LiFePO_4$ and $FePO_4$ amount is changed by a moving phase boundary, and not via a solid solution. The Li solubility increases by decreasing particle size, as a result of the increased interfacial energy per unit volume. By considering this interfacial energy, *ex situ*

diffraction studies of $LiFePO_4$ nanoparticles suggest that once an energetically unfavorable $LiFePO_4$-$FePO_4$ interface is formed, this interface quickly moves through the particle so as to return to the most stable $LiFePO_4$ or $FePO_4$ state, so only $LiFePO_4$ and $FePO_4$ particles are observed by *ex situ* characterization techniques.

Recently published *in situ* XRD investigations performed on micrometer-sized $LiFePO_4$ show the emergence of a metastable crystalline phase with an intermediate Li composition of $Li_{0.6-0.75}FePO_4$ when cycled at high rates [5]. Whereas, studies on nanometer-sized $LiFePO_4$ particles are limited to low [6] and moderate [7] current rates, and only small deviations in stoichiometry from $LiFePO_4$ and $FePO_4$ were observed during cycling. Due to the faster transport kinetics of nanoparticles, a high current rate is required to reach the kinetic limit of a phase transformation including an *in situ* XRD setup with high X-ray intensity and a fast read detector so that the reaction can be probed with high time resolution. By studying the nanoparticles under high current rates, Liu et al. [8] were able to force enough particles to transform simultaneously so that the reacting particles can be detected and the nature of the phase transformations that occur at an overpotential can be determined.

In situ diffraction patterns during the first five cycles of $LiFePO_4$ with an average size of 186 nm at 10 C galvanostatic charge-discharge are shown in **Figure 2(a)**. All peaks in the diffraction patterns can be indexed to either the Li-rich $Li_{1-\alpha}FePO_4$ phase or the Li-poor $Li_\beta FePO_4$ phase. During charge, peaks representing $Li_{1-\alpha}FePO_4$ phase disappear, and these peaks reappear on discharge; conversely $Li_\beta FePO_4$ peaks appear on charge and disappear on discharge. Interestingly, they observed the appearance of positive intensities between the 8.15–8.4, 13.95–14.1, and 15.15–15.4, 2θ ranges, which shows the formation of phases, in which the lattice parameters are different from those of $LiFePO_4$ and $FePO_4$. A closer view of individual diffraction patterns in selected 2θ regions is shown in **Figure 2(b)**. All of the reflections exhibit highly symmetrical profiles at the beginning of the first charge; however, the $LiFePO_4$ (2 0 0) and (3 0 1) reflections start to broaden asymmetrically toward higher angles with the charge. The most significant asymmetrical broadening is observed on discharge in patterns (*f*) and (*g*), where the (2 0 0) reflections from both phases are connected by a positive intensity band. Similar trend is observed in the second cycle as well. Neither the peak position nor the peak shape of $LiFePO_4$ is restored to that of the original state by the end of the second cycle. All selected peaks shift toward higher angle and become broad, as shown in pattern (*r*). This peak shift shows a decrease in the unit cell volume, which will in turn reduce the accessible capacity of $LiFePO_4$ at high rates. So, at the end of each cycle, the Li composition is not restored to stoichiometric $LiFePO_4$, instead a solid solution ($Li_{1-\alpha}FePO_4$) is formed with a smaller unit cell volume than that of the stoichiometric $LiFePO_4$. By using synchrotron radiation-based wide-angle X-ray scattering technique and doing further analysis like profile fitting by convoluting separate contributions from size and lattice-parameter variations with appropriate analytical functions, they further confirmed that phase transformations in nanoparticulate $LiFePO_4$ proceed, at least at high rates, via a continuous change in structure rather than a distinct moving phase boundary between $LiFePO_4$ and $FePO_4$.

http://dx.doi.org/10.5772/67029

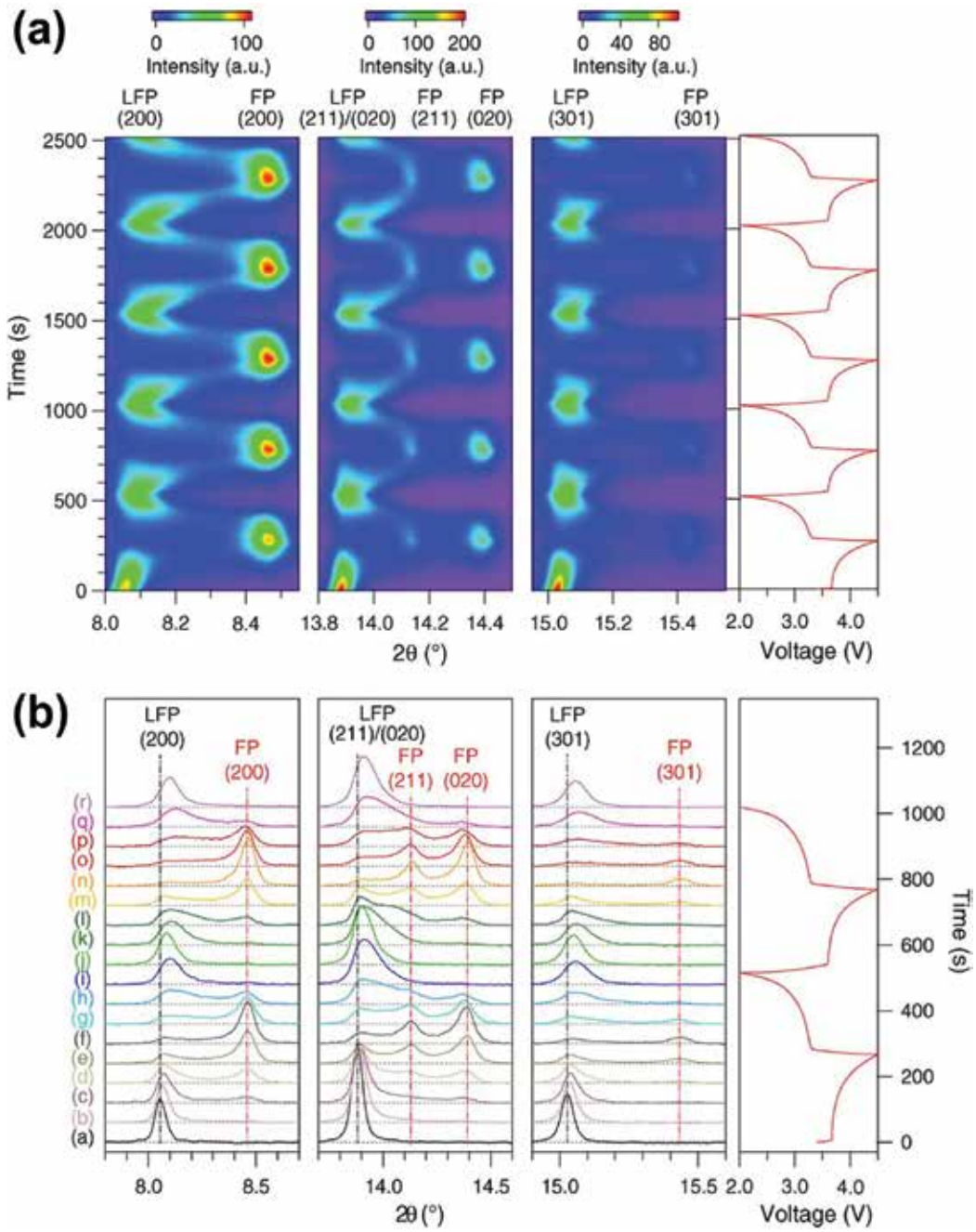

Figure 2. The variations of XRD pattern during the galvanostatic charge and discharge at a rate of 10 C. (a) The image plot of diffraction patterns for selected reflections during the first five electrochemical cycles. The corresponding voltage curve is plotted to the right. (b) Selected individual diffraction patterns during the first two electrochemical cycles stacked against the voltage profile [8].

2.2. Small-angle X-ray scattering (SAXS)

The structural characterization of nanoscale systems is a very active area of research these days not only in energy storage material system but in variety of other scientific disciplines as well. Nanoscale systems can be studied with real-space imaging or reciprocal space scattering techniques. X-ray scattering techniques provide reciprocal space data, whereas electron microscopy-based imaging techniques usually provide real-space data. A distribution of electron density at nanometer length scales will scatter an X-ray beam to low angles, while that in the atomic scale will scatter to high angles. Therefore, small-angle X-ray scattering (SAXS) is a technique to study material structures at small angles or large distances. SAXS is a powerful technique to determine, not only the object's size, size distribution, shape, surface structure, relative positions of particles, but it can also be used for the structure factor analysis. The size distribution function is a key piece of information that can be obtained from SAXS. Collected data can be fitted, when the shape of a particle is known or can be assumed, to get the size distribution. SAXS form factor analysis provides useful information at the single-particle level; the structure factor allows to figure out the organization of particle systems in the structure.

In recent years, the development of synchrotron radiation X-ray sources has made possible to adopt novel approaches to utilize X-ray scattering technique for nanoparticle research. SAXS is nondestructive and provides structural data averaged over macroscopic sample volumes. Modern synchrotron radiation-based SAXS is capable of structural characterization of sample in its working state because of its tunable flux and energy that is particularly useful for nanoparticle research especially for electrochemical energy storage systems.

2.2.1. Case study

SAXS is a useful characterizing technique for characterization of Li-ion batteries and other energy storage materials. Conventional Li-ion batteries suffer from capacity loss due to several failure mechanisms associated with the strain induced in anode and cathode materials upon electrochemical cycling. Ordered mesoporous materials have been considered as potential candidates for the next-generation electrode materials. There are several advantages associated with mesoporous electrode materials, for example, the ordered framework of mesopores which can act as a physical buffer for the volume changes, and it reduces the diffusion path length to promote easy Li and electron transport. These structures offer intrinsic high specific surface area that provides large active surface between electrolyte and electrode material. SAXS is an ideal technique to study ordered mesoporous structures. Recently, Park et al. [9] have developed an *in situ* synchrotron-based small-angle X-ray scattering (SAXS) technique to investigate the nanostructural changes of ordered mesoporous materials during cycling for further understanding the Li storage reactions.

Information on nanostructural changes of an electrode material from SAXS allows to understand fine details of nanostructured electrode dynamics during electrochemical cycling. They performed *in situ* SAXS studies on the meso-Co_xSn_y anode materials to probe the mesoscopic structural changes during its electrochemical cycling to understand the behavior of the entire electrode with different Co contents. *In situ* SAXS data including contour projection for each meso-Co_xSn_y composition during the first cycle are shown in

http://dx.doi.org/10.5772/67029

Figure 3. All the *in situ* SAXS patterns indicate that the present meso-Co_xSn_y materials retain highly ordered meso-structures, even though the intermetallic electrodes are known to form Li alloys during lithium insertion. There are no significant changes in the relative scattering intensities of SAXS patterns, when a discharge current is applied, until the discharge potential reaches to 0.2 V. While discharging below 0.2 V, the scattering peaks move slightly toward the lower angle, and their intensity is decreases. These results indicate that the meso-structures of all the meso-Co_xSn_y electrodes are retained until 0.2 V and then small expansion of mesoscopic cell volume and somewhat loss of meso-structural periodicity take place during the Li-Sn alloying reaction. Both the intensities and positions seem to be recovered to the initial state after the complete cycle, indicating the structural stability of meso-Co_xSn_y electrodes.

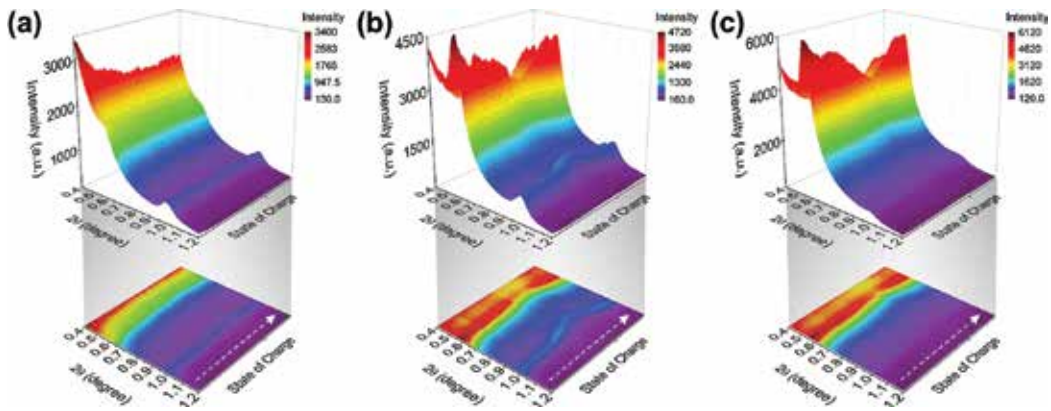

Figure 3. Color-coded 3D contours and projection maps showing SAXS data collected from ordered meso-Co_xSn_y electrodes during *in situ* experiment: (a) meso-$Co_{0.5}Sn_{0.5}$, (b) meso-$Co_{0.3}Sn_{0.7}$, and (c) meso-$Co_{0.1}$ $Sn_{0.9}$ [9].

In order to get more insight of the *in situ* SAXS results, dQ/dV data, relative peak intensities, and mesoscopic lattice parameters were plotted against the cell voltage for the meso-Co_xSn_y electrodes as shown in **Figure 4**. This data indicates about 19% decrease of relative SAXS peak intensity and 14% expansion of meso-structural cell volume in the meso-$Co_{0.5}Sn_{0.5}$ electrode after the full discharge. In meso-$Co_{0.3}Sn_{0.7}$ electrode, there is only 13% change in the peak intensity, whereas the meso-structural cell volume expansion is 41% that is much larger than that of the meso-$Co_{0.5}Sn_{0.5}$. The initial discharge capacities of the meso-$Co_{0.3}Sn_{0.7}$ and meso-$Co_{0.5}Sn_{0.5}$ electrodes are 1321 and 822 mAh/g, respectively, due to the different amount of electroactive Sn. **Figure 4(f)** shows a significant 52% decrease in the SAXS peak intensity with relatively large volume change of 30% in the meso-$Co_{0.1}Sn_{0.9}$ electrode, while its initial discharge capacity is 1493 mAh/g. These *in situ* SAXS results for meso-Co_xSn_y electrodes during cycling directly provide roles of the inactive Co element as a chemical buffer; meanwhile, the well-defined nanoporous system acts as a physical buffer to accommodate the volume changes in the electrode. *In situ* SAXS reveals that the mesoscopic volume and meso-structural order change reversibly during cycling. It indicates that reliable nanostructure is developed and that relieves severe internal strain induced by huge volume change upon the repeated electrochemical reactions.

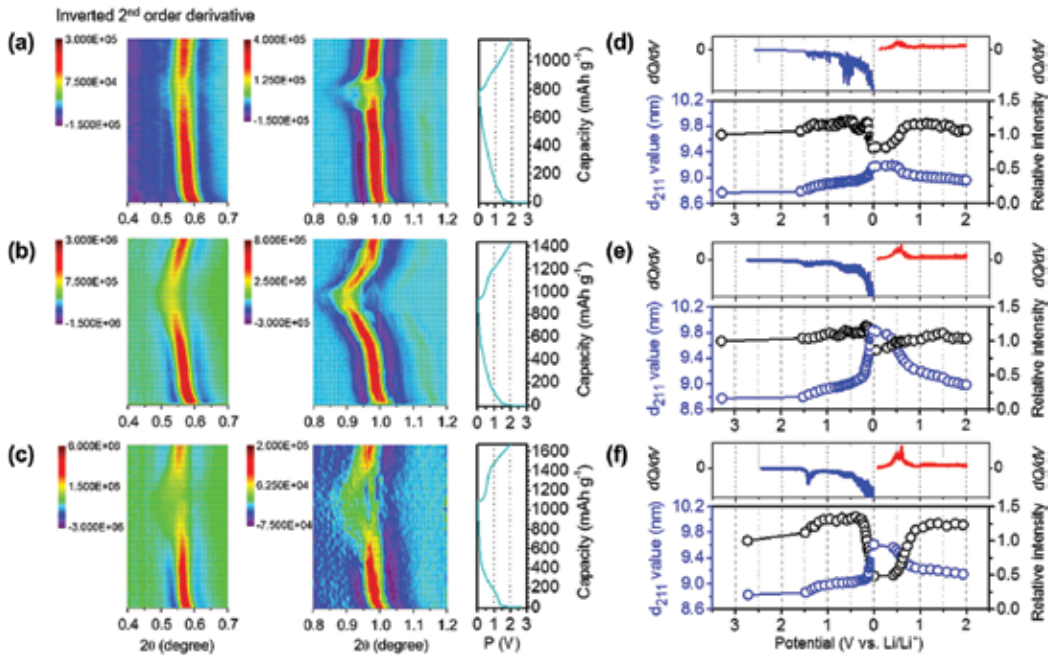

Figure 4. (a–c) Color-coded contour projection maps during *in situ* experiment with corresponding voltage profile and (d–f) the changes in lattice parameters and resolved peak-relative intensities with the corresponding d*Q*/d*V* plot for meso-$Co_{0.5}Sn_{0.5}$, meso-$Co_{0.3}Sn_{0.7}$, and meso-$Co_{0.1}Sn_{0.9}$, respectively [9].

3. Synchrotron radiation-based X-ray absorption techniques

3.1. Hard X-ray absorption spectroscopy (HXAS)

X-ray absorption spectroscopy (XAS) is a powerful technique that can characterize aII forms of matter, irrespective of their degree of crystallinity. Traditionally, diffraction-based characterization methods are being used for structural investigations, and reliable structural information can be determined for materials that exhibit a long-range structural order. In contrast XAS can probe the local structure of disordered solids, liquids, as well as amorphous materials. XAS has vast application area ranging from coordination chemistry, catalysis, biology, and surface physics to material chemistry. One of the major advantages of XAS is its atomic selectivity which makes it possible to study the local structure of each different constituent of a sample. Sample preparation for XAS is very simple, and experiments can be performed *in situ*.

XAS spectrum can be divided in two parts, namely, X-ray absorption near-edge structure (XANES) and extended X-ray absorption fine structure (EXAFS). In XANES phenomenon, an element-specific signal is generated, typically using a synchrotron radiation source. A core electron absorbs the energy of incident X-rays and gets excited beyond the Fermi level, leaving behind a core hole. The synchrotron radiation sources can provide energy that is right for desired electron transitions. When a sample is exposed to X-rays, it will absorb part of the

incoming photon beams. Other phenomena occurring are heat, X-ray fluorescence, production of unbound electrons, and of course the scattering of X-rays. The absorption of X-rays can be measured quantitatively, and it follows exponential decay given by the Beer's law [10].

The EXAFS phenomenon arises from the quantum mechanical interference of the scattering of a photoelectron by the potential of the surrounding atoms. A photoelectron emitted by the photo-absorbing atom propagates as a spherical wave and spreads out over the solid. The amplitude of all the reflected electron waves adds either constructively or destructively to the spectrum of the absorbing atom as shown in **Figure 5(a)** and **5(b)** respectively, and hence the X-ray absorption coefficient exhibits a typical oscillation. A crucial issue is the recognition that the photoelectron is not infinitely long lived; it decays as a function of time and distance, and thus the EXAFS cannot probe long-range distances. EXAFS can give only local structural information of about several angstroms around the selected atomic species.

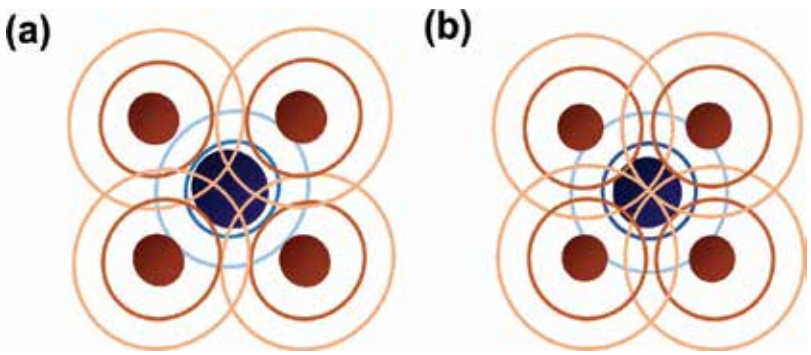

Figure 5. Constructive and destructive interference of electron wave during and XAS event.

The recent availability of high-brightness synchrotron radiation sources has resulted in a prosperous development of XAS technique, and it is finding wide application area including the energy storage material field.

3.1.1. Case study

Major challenges faced by Li-ion batteries are demand for high-energy density, capacity retention, safety, and low cost. In order to achieve the higher-energy density than that of currently commercialized ones, metal oxides are being considered as potential anode materials due to their high-energy density arising from conversion and alloying reactions [11]. SnO_2 is a candidate anode material for future batteries, and previous studies show that SnO_2 anode undergoes an irreversible conversion reaction in the initial cycle followed by a reversible alloying reaction of Sn [12, 13]:

$$SnO_2 + 4Li^+ + 4e^- \rightarrow Sn + 2Li_2O \quad (711\,mAh/g) \tag{2}$$

$$\mathrm{Sn} + x\mathrm{Li}^{+} + x\mathrm{e}^{-} \rightarrow \mathrm{Li}_x\mathrm{Sn}\ (783\mathrm{mAh/g})\ (0 << x << 4.4) \quad (3)$$

Reaction based on Eq. (2) is the main reason for initial irreversible capacity of this anode material, whereas reaction based on Eq. (3) is responsible for reversible capacity of these electrode materials in the subsequent cycles. Surprisingly, reported capacity of nanostructured SnO_2-based anode materials is higher than the abovementioned theoretical capacity (783 mAh/g). To understand this anomalous capacity, Kim et al. [14] conducted the synchrotron-based XAS experiments on mesoporous SnO_2 anode material. The combination of XRD and XAS was used to probe the bulk and local structure. The XRD peaks almost disappeared (not shown here) after discharging below 0.7 V indicating that mesoporous SnO_2 converts to an amorphous nano-Li_xSnO_2 phase, so XRD alone was unable to further characterize this material.

Figure 6(a) shows selected Sn K-edge XANES and EXAFS patterns in the initial discharge region of the first cycle. The oxidation state of Sn in the mesoporous SnO_2 is 4+. The reduction of Sn takes places in the beginning of discharge, and the Sn K-edge XANES spectra show prominent shift toward lower-energy values. This reduction of Sn during conversion reaction effects the local environment around the Sn atom. The first prominent peak in Sn K-edge EXAFS spectra corresponds to the Sn-O interaction in the first coordination shell, and the broad peaks in 2.2–3.9 Å region are due to the Sn-Sn, Sn-O, and Sn-Sn interactions in the subsequent coordination shells. The intensity of these peaks decrease significantly during discharge due to displacement of reacting species during the conversion reaction. **Figure 6(b)** shows XAS data obtained in the middle discharge region of the first cycle. In this region, Sn K-edge XANES spectra show only negligible shift toward lower-energy values. However, Sn K-edge intensities decrease in this region, showing the formation of metallic Sn. After discharging beyond 600 mAh/g, the intensity of the Sn-O peak decreases, a new peak at around 2.6 Å emerges, which corresponds to the Sn-Sn(Li) pair in the Li_xSn alloy, and the intensity of this new peak increases with the increase of the Li/Sn ratio. The intensity of the peaks representing the Sn-O peaks gradually drops, and that of the Sn-Sn(Li) peak increases during this discharge region. The representative peaks for Sn-O bond disappear when the discharge capacity reaches 1500 mAh/g, which shows the completion of the conversion reaction. So, the remaining discharge capacity can be assigned to the alloying reaction only. **Figure 6(c)** shows the XAS data obtained from the mesoporous SnO_2 electrode in the last discharge region of the first cycle. XANES data obtained in this discharge region show a shift toward high energy of the Sn K-edge. During the alloying reaction, charge redistribution takes place to minimize the electrostatic energy which results in shifts of Sn K-edge. In the EXAFS spectra, the amplitude of the Sn-Sn peak continuously decreases in this discharge region. Due to increase in the Li/Sn ratio, the amount of Li around Sn increases. Li has a much smaller electron-scattering cross section compared to Sn. So, the intensity of the Sn-Sn(Li) peak decreases when the Li/Sn molar ratio exceeds 3 [15]. This trend of XANES and EXAFS data suggests that the capacity in this deep discharge region is obtained only by Li alloying in the Li_xSn phase until it achieves its nominal composition of $Li_{4.4}Sn$.

http://dx.doi.org/10.5772/67029

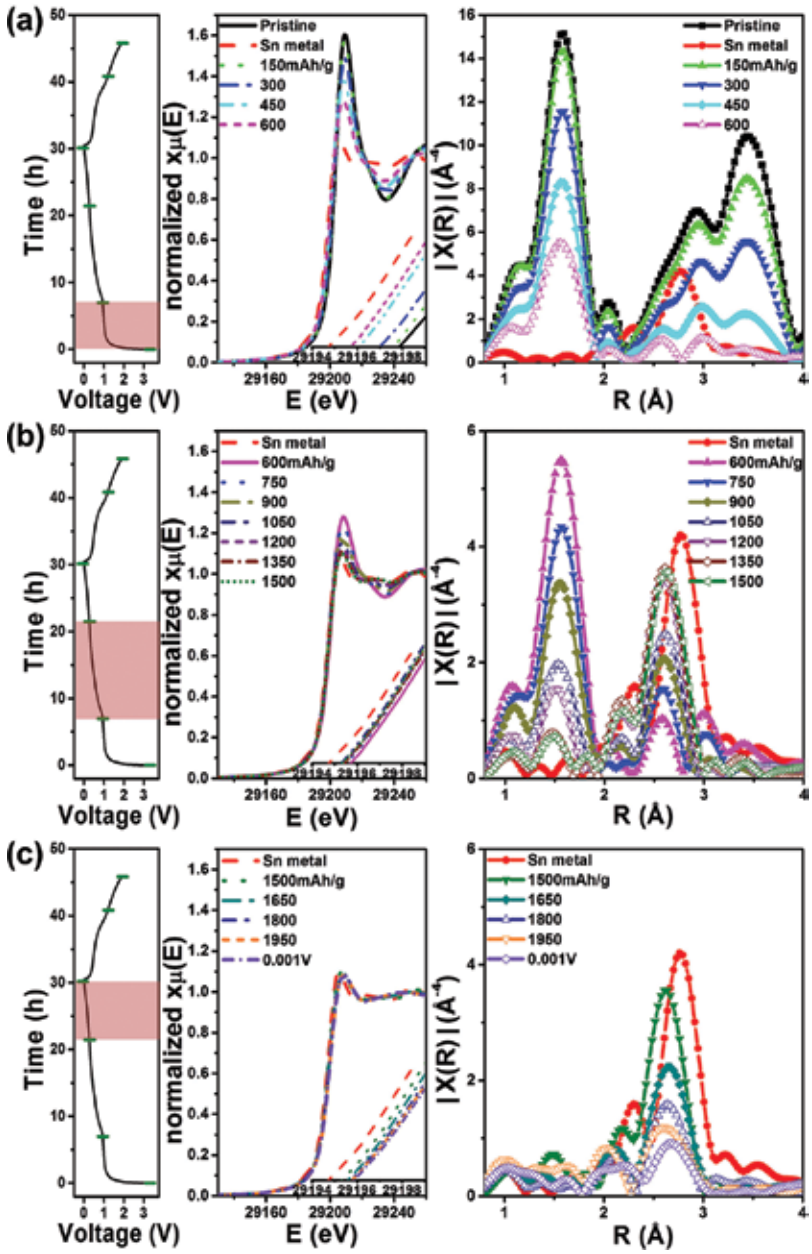

Figure 6. Sn K-edge XANES and EXAFS spectra with corresponding voltage profile taken in (a) the first discharge region, (b) the middle discharge region, and (c) the last discharge region of the first cycle [14].

Figure 7(a) shows XAS data taken from the mesoporous SnO_2 electrode in the beginning of charge. The Sn K-edge XANES spectra shift reversibly toward lower-energy values, and EXAFS spectra show the rise of Sn-Sn(Li)-related peaks, suggesting that the dealloying

reaction is taking place in this voltage region. After the cell was charged to 500 mAh/g, the intensity of the Sn-Sn(Li) peaks starts to decrease and that of Sn-O peak increases, as shown in **Figure 7(b)**. Appearance of the Sn-O peak and damping of the Sn-Sn peak are only possible when Li_2O formation is at least partially reversible, along with the formation of the SnO_x phase. These results suggest that the reversible charge capacity at the end of the charge can be assigned to dealloying of Li_xSn phase as well as the conversion reaction of Sn into the SnO_x phase. After achieving charge capacity of 900 mAh/g, peaks representing the Sn-O coordination shell grow with small change of the Sn-Sn peak, indicating that reversible charge capacity is mainly achieved by conversion reaction in this region. XANES spectra do not show noticeable shift in this charge region. The overall EXAFS data in the first cycle show that active material in SnO_2 does not come back to its initial composition after one complete electrochemical cycle; it changes into metallic Sn with a small quantity of amorphous SnO_x along with Li_xSn phase. In short, local structure analyses via hard XAS technique successfully demonstrated the origin of high capacity of mesoporous SnO_2 beyond its reported theoretical capacity.

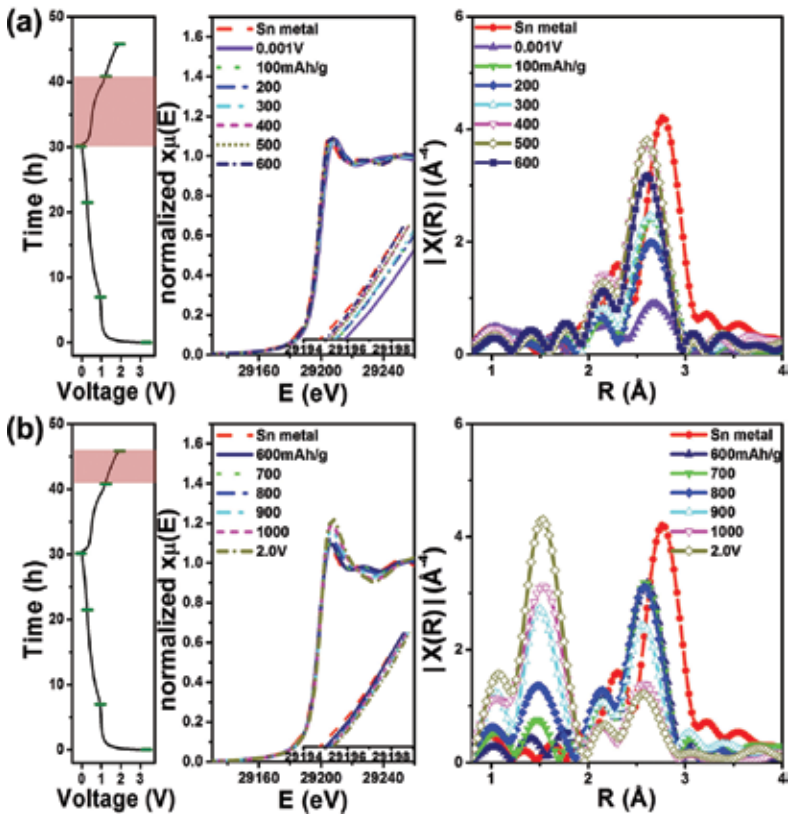

Figure 7. Sn K-edge XANES and EXAFS spectra with corresponding voltage profile taken in (a) the first charge region and (b) the last charge region of the first cycle [14].

http://dx.doi.org/10.5772/67029

3.2. Soft X-ray absorption spectroscopy (SXAS)

Soft XAS is an XAS technique that uses soft X-rays, with energies ranging from 150 to 1200 eV. This energy range covers the K-edge of light elements, for example, B, C, N, O, and F, along with the $L_{2,3}$ edges of the first-row transition metal elements. In an XAS experiment, tunable X-rays hit the sample and 1s electrons are ejected when the X-ray reaches a specific energy, such as the K-edge energy of oxygen (532 eV). The resulting core hole is relaxed either by transfer of electron from higher levels into the core hole which leads to the emission of fluorescent X-rays or by releasing the Auger electrons. A schematic diagram of the core hole relaxation process is shown in **Figure 8**. Both the fluorescent X-rays and the Auger electron signals can be utilized to get XAS spectra as both the signals are proportional to the incident X-ray absorption. The fluorescent X-rays possess higher escape depth of about 2000 Å, contrary to the Auger electrons, which have an escape depth of only about 50 Å. Because of this difference in escape depths, different information can be collected from fluorescent X-rays and Auger electrons. The fluorescent X-ray signal is more sensitive about the bulk structure, whereas the Auger electron yield is responsive for the surface structure. By measuring fluorescent and electron yields simultaneously, information about both surface and bulk can be obtained in the same experiment [16].

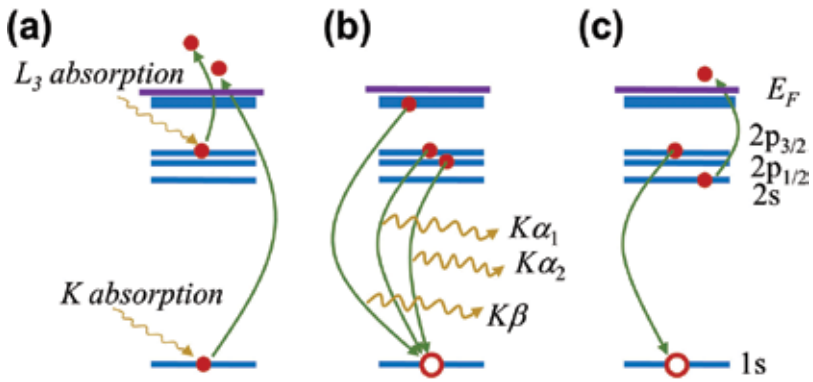

Figure 8. Schematic diagram of principle of (a) absorption, (b) fluorescent, and (c) Auger electron-yield soft X-ray absorption spectroscopy.

3.2.1. Case study

Thermal stability is a critical issue related to the safety of the rechargeable batteries. Traditionally, it is studied by using thermo-analytical techniques like TGA, or there are some studies by using *in situ* XRD. Yoon et al. utilized *in situ* temperature-dependent soft XAS measurements for the first time, in order to understand the role of different transition metals in thermal degradation of the charged $LiNi_{0.8}Co_{0.15}Al_{0.05}O_2$ electrode [17]. They monitored the element-selective structural changes in the charged cathode material on the surface and in the bulk during heating of electrode material. The findings of their study provide important guidelines to design new electrode materials with enhanced thermal safety.

Normalized Ni L-edge spectra of $Li_{0.33}Ni_{0.8}Co_{0.15}Al_{0.05}O_2$ cathode using fluorescent yield (FY) mode at various temperatures are shown in **Figure 9(a)**, and the partial electron yield (PEY)

mode spectra are shown in **Figure 9(b)**. Due to spin-orbit interaction of the core hole, the absorption spectrum splits into two energy bands, Ni $2p_{3/2}$ (L_3 edge) and Ni $2p_{1/2}$ (L_2 edge). Changes in energy position of these bands can indicate valence-state variations during the heating process as energy position shifts about 1 eV per oxidation-state change [18]. Ni L_3 and L_2 spectra obtained in the bulk sensitive fluorescent yield mode do not show energy position changes. $Li_{0.33}Ni_{0.8}Co_{0.15}Al_{0.05}O_2$ material is based on layered structure with $R\bar{3}m$ space group, and the change into the *Fd3m* structure during heating would not involve a valence-state change or shift in energy position of L-edges. However, the energy position of Ni L_3 and L_2 spectrum moves to lower-energy values in case of surface-sensitive electron yield mode, and a rather prominent shift takes place at around 200°C that shows the presence of a NiO-type rock salt structure on the surface at this temperature. **Figure 9(c)** and **(d)** shows normalized Co L-edge XAS spectra at various temperatures using FY and PEY mode, respectively. Unlike the Ni L-edge spectra, the electron-yield spectra of the Co species do not show energy shifts. There are no visible changes in both the FY and the PEY spectra which show that cobalt ions have better thermal stability compared to the nickel ions. Partial substitution of nickel by cobalt in the cathode materials enhances its thermal stability.

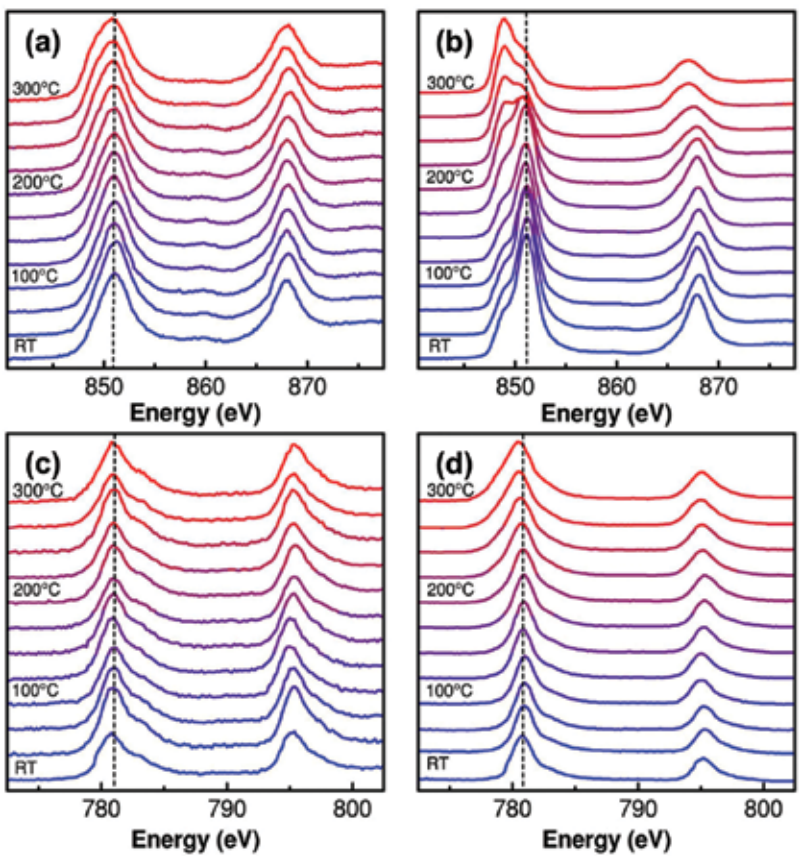

Figure 9. Normalized XAS spectra of $Li_{0.33}Ni_{0.8}Co_{0.15}Al_{0.05}O_2$ cathode material at different temperatures using (a) Ni L-edge FY mode, (b) Ni L-edge PEY mode, (c) Co L-edge FY mode, and (d) Co L-edge PEY mode [17].

Figure 10 shows the normalized O K-edge XAS spectra of $Li_{0.33}Ni_{0.8}Co_{0.15}Al_{0.05}O_2$ cathode material at various temperatures, using FY mode and PEY mode. The first prominent absorption peak at 528.5 eV corresponds to transition from oxygen 1s orbital to a hybridized state of metal 3d-O 2p orbitals. The oxygen K-edge spectra contain information associated with transitions to hybridized states of O 2p-Ni 4sp and other empty orbitals in that energy region. Like the L-edge spectra, there is no significant change in the fluorescence-yield spectra, but the surface-sensitive electron-yield spectra show a significant decrease of the peak at 528.5 eV when temperature rises above 200°C. The PEY data show other distinct differences as well. The intensity of the distinct peak at ~534 eV is decreasing, whereas that of the peak at ~532 eV is increasing with rising temperature. The features at around 532 eV and 534 eV are associated with the presence of NiO and Li_2CO_3, respectively, as shown by the spectra of the standards in **Figure 10(b)**. Upon heating, intensity of the features at 534 eV decreases which suggests that carbonate present on the surface is gradually decomposed. Conversely, the intensity of the 532 eV peak increases with temperature, particularly above 200°C, and the intensity of the 528.5 eV peak decreases. These observations indicate the formation of reduced divalent nickel oxide. This finding is in accordance with the Ni L-edge measurements. The presence of NiO-type rock salt structure and its increased formation at electrode surface with increasing temperature indicates nickel oxides tend to release oxygen at higher temperature. The oxygen K-edge spectra are consistent with the data obtained from the Ni L-edge and point toward the initiation of thermal reduction reactions around Ni sites on the surface of the cathode sample material.

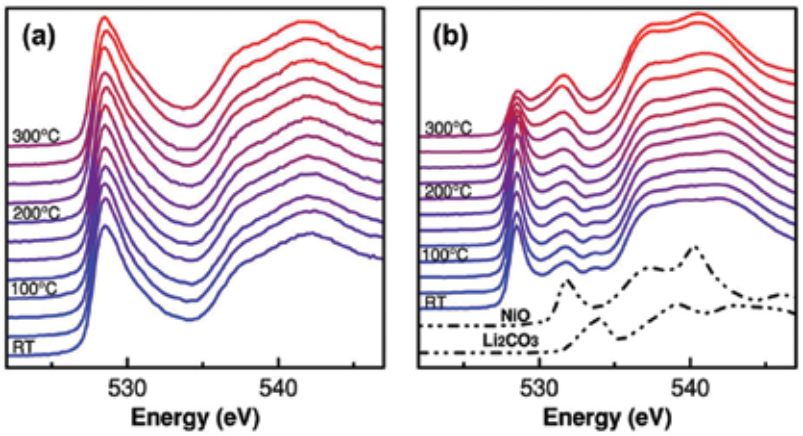

Figure 10. Normalized O K-edge XAS spectra of $Li_{0.33}Ni_{0.8}Co_{0.15}Al_{0.05}O_2$ cathode material at different temperatures using (a) FY mode and (b) PEY mode [17].

These investigations demonstrated the capability of *in situ* soft XAS techniques to investigate thermal behavior of cathode materials and show that there is no valence-state change in the bulk despite the layered structure of the $Li_{0.33}Ni_{0.8}Co_{0.15}Al_{0.05}O_2$ cathode material converts to spinel structure. The surface-sensitive PEY measurements reveal that this electrode material loses oxygen at high temperatures leading to a lower oxidation state of Ni and formation of NiO-like rock salt structure. No evidence of a surface reaction near Co sites in the investigated

temperature range was found which shows that the Co is more stable at elevated temperatures compared to the Ni in $Li_{0.33}Ni_{0.8}Co_{0.15}Al_{0.05}O_2$. The capability of soft XAS to discriminate the surface and bulk electronic structures with element specificity makes it a valuable addition to the advanced synchrotron-based characterization technique that help understand thermal behavior of battery electrodes.

4. Conclusion

The application of synchrotron-based characterization techniques to investigate energy storage materials is playing a major role in the fundamental understanding of the electrochemical reaction mechanism of energy storage materials. This chapter provides an overview about various X-ray synchrotron-based characterization techniques and their applications to electrode materials to characterize the nano- and mesoporous phase dynamics, long-range crystal order, and local and electronic changes during the electrochemical cycling of electrode materials. The combination of these techniques can provide critical information to reveal the electrochemical reaction mechanism and functional properties of electrode materials in order to better understand the existing energy storage systems and help design modern electrode materials for future applications. Given the recent developments, it can be expected that application of synchrotron-based characterization techniques will become increasingly important in development of high-performance and stable energy storage materials.

Acknowledgements

The authors acknowledge the financial support from Human Resources Development Program (No. 20124010203270) of the Korea Institute of Energy Technology Evaluation and Planning (KETEP).

Author details

Shoaib Muhammad, Hyunchul Kim and Won-Sub Yoon*

*Address all correspondence to: wsyoon@skku.edu

Department of Energy Science, Sungkyunkwan University, Suwon, South Korea

References

[1] N. A. Young. The application of synchrotron radiation and in particular X-ray absorption spectroscopy to matrix isolated species. Coordination Chemistry Reviews. 2014;**277–278**:224–274. DOI: 10.1016/j.ccr.2014.05.010

[2] M. Ladd, R. Palmer. X-rays and white radiation. In: M. Ladd and R. Palmer, editors. Structure Determination by X-ray Crystallography. 5th ed. Springer Science+Business Media New York: Springer US; 2013. pp. 111–159. DOI: 10.1007/978-1-4614-3954-7_3

[3] M. Kunduraci, G. G. Amatucci. Synthesis and characterization of nanostructured 4.7 V $Li_xMn_{1.5}Ni_{0.5}O_4$ spinels for high-power lithium-ion batteries. Journal of the Electrochemical Society. 2006;**153**(7):A1345–A1352. DOI: 10.1149/1.2198110

[4] A. K. Padhi, K. S. Nanjundaswamy, J. B. Goodenough. Phospho-olivines as positive-electrode materials for rechargeable lithium batteries. Journal of the Electrochemical Society. 1997;**144**(4):1184–1194. DOI: 10.1149/1.1837571

[5] Y. Orikasa, T. Maeda, Y. Koyama, H. Murayama, K. Fukuda, H. Tanida, H. Arai, E. Matsubara, Y. Uchimoto, Z. Ogumi. Direct observation of a metastable crystal phase of $LixFePO_4$ under electrochemical phase transition. Journal of American Chemical Society. 2013;**135**(15):5497–5500. DOI: 10.1021/ja312527x

[6] Y. Orikasa, T. Maeda, Y. Koyama, H. Murayama, K. Fukuda, H. Tanida, H. Arai, E. Matsubara, Y. Uchimoto, Z. Ogumi. Transient phase change in two phase reaction between $LiFePO_4$ and $FePO_4$ under battery operation. Chemistry of Materials. 2013;**25**(7):1032-1039. DOI: 10.1021/cm303411t

[7] N. Sharma, X. Guo, G. Du, Z. Guo, J. Wang, Z. Wang, V. K. Peterson. Direct evidence of concurrent solid-solution and two-phase reactions and the nonequilibrium structural evolution of $LiFePO_4$. Journal of American Chemical Society. 2012;**134**(18):7867–7873. DOI: 10.1021/ja301187u

[8] H. Liu, F. C. Strobridge, O. J. Borkiewicz, K. M. Wiaderek, K. W. Chapman, P. J. Chupas, C. P. Grey. Capturing metastable structures during high-rate cycling of $LiFePO_4$ nanoparticle electrodes. Science. 2014;**344**(6191):1480–1487. DOI: 10.1126/science.1252817

[9] G. O. Park, J. Yoon, J. K. Shon, Y. S. Choi, J. G. Won, S. B. Park, K. H. Kim, H. Kim, W. S. Yoon, J. M. Kim. Discovering a dual-buffer effect for lithium storage: durable nanostructured ordered mesoporous Co-Sn intermetallic electrodes. Advanced Functional Materials. 2016;**26**(17):2800–2808. DOI: 10.1002/adfm.201600121

[10] D. F. Swinehart. The Beer-Lambert Law. Journal of Chemical Education. 1962;**39**(7):333–335. DOI: 10.1021/ed039p333.

[11] W. J. Zhang. A review of the electrochemical performance of alloy anodes for lithium-ion batteries. Journal of Power Sources. 2011;**196**(1):13–24. DOI: 10.1016/j.jpowsour.2010.07.020

[12] I. A. Courtney, J. R. Dahn. Electrochemical and *in situ* X-ray diffraction studies of the reaction of lithium with tin oxide composites. Journal of the Electrochemical Society. 1997;**144**(6):2045–2052. DOI: 10.1149/1.1837740

[13] I. A. Courtney, J. R. Dahn. Key factors controlling the reversibility of the reaction of lithium with SnO_2 and Sn_2BPO_6 glass. Journal of the Electrochemical Society. 1997;**144**(9):2943–2948. DOI: 10.1149/1.1837941

[14] H. Kim, G. O. Park, Y. Kim, S. Muhammad, J. Yoo, M. Balasubramanian, Y. H. Cho, M. G. Kim, B. J. Lee, K. S. Kang, H. S. Kim, J. M. Kim, W. S. Yoon. New insight into the reaction mechanism for exceptional capacity of ordered mesoporous SnO_2 electrodes via synchrotron-based X-ray analysis. Chemistry of Materials. 2014;**26**(22):6361–6370. DOI: 10.1021/cm5025603

[15] A. N. Mansour, S. Mukerjee, X. Q. Yang, J. McBreen. *In situ* X-ray absorption and diffraction study of the Li reaction with a tin composite oxide glass. Journal of the Electrochemical Society. 2000;**147**(3):869–873. DOI: 10.1149/1.1393284

[16] J. McBreen. The application of synchrotron techniques to the study of lithium-ion batteries. Journal of Solid State Electrochemistry. 2009;**13**(7):1051–1061. DOI: 10.1007/s10008-008-0685-1

[17] W. S. Yoon, O. Haas, S. Muhammad, H. Kim, W. Lee, D. Kim, D. A. Fischer, C. Jaye, X. Q. Yang, M. Balasubramanian, K. W. Nam. *In situ* soft XAS study on nickel-based layered cathode material at elevated temperatures: a novel approach to study thermal stability. Scientific Reports. 2014;**4**(6827):1–5. DOI: 10.1038/srep06827

[18] H. Wang, D. S. Patil, W. Gu, L. Jacquamet, S. Friedrich, T. Funk, S. P. Cramer. L-edge X-ray absorption spectroscopy of some Ni enzymes: probe of Ni electronic structure. Journal of Electron Spectroscopy and Related Phenomena. 2001;**114–116**:855–863. DOI: 10.1016/S0368-2048(00)00370-4

Chapter 6

Studies of Lithium-Oxygen Battery Electrodes by Energy-Dependent Full-Field Transmission Soft X-Ray Microscopy

Dino Tonti, Mara Olivares-Marín,
Andrea Sorrentino and Eva Pereiro

Additional information is available at the end of the chapter

http://dx.doi.org/10.5772/66978

Abstract

Energy-dependent full-field transmission soft X-ray microscopy is a powerful technique that provides chemical information with spatial resolution at the nanoscale. Oxygen K-level transitions can be optimally detected, and we used this technique to study the discharge products of lithium-oxygen batteries, where this element undergoes a complex chemistry, involving at least three different oxidation states and formation of nanostructured deposits. We unambiguously demonstrated the presence of significant amounts of superoxide forming a composite with peroxide, and secondary products such as carbonates or hydroxide. In this chapter, we describe the technique from the fundamental to the observation of discharged electrodes to illustrate how this tool can help obtaining a more comprehensive view of the phenomena taking place in metal air batteries and any system involving nanomaterials with a complex chemistry.

Keywords: metal-air batteries, superoxide, peroxide, XAS, XANES, TXM, spectromicroscopy

1. Introduction

With lithium ion batteries becoming a mature technology, it is now clear that applications such as electric vehicles require chemistries with higher energy density to reach acceptable driving ranges without compromising performance and comfort already common with conventional vehicles. This pushed high research efforts in the area of lithium-air (or more precisely lithium-oxygen) batteries, presenting the highest energy density among known scalable battery devices, and of metal-air batteries in general. However, the difficulty to obtain a

high reversibility and long cycle life still implies a significant barrier to become a technology. In many applications the precise knowledge of composition and morphology of materials at the nanoscale is a key to control performance and reliability. Metal-oxygen batteries are one of these cases; in fact, they involve complex reaction and precipitation processes that need to be understood in detail to obtain true reversible operation. The determination of composition as a function of position in the nano-sized precipitate at different charging states is the most valuable information for this understanding. A few physical techniques are routinely used to reveal the processes underlying battery behavior, e.g., XRD, TEM, SEM, XPS, FTIR, Raman, and mass spectroscopy. In this chapter we present the application to this problem of energy-dependent full-field transmission soft X-ray microscopy. This spectromicroscopical technique based on synchrotron radiation is able to give a full picture at the nanometer scale of the oxidation state and spatial distribution in the cathode of oxygen, the most relevant element in any metal-air battery. Although a host of physical techniques are routinely used to reveal the processes underlying battery behavior (e.g., XRD, TEM, SEM, XPS, FTIR, Raman, and mass spectroscopy), this technique is unique in providing high-resolution imaging with chemical information.

We will first introduce the basic concepts of metal-air batteries and transmission X-ray microscopy, then detail how the technique can be applied to battery electrodes, and finally provide some examples of studies that we performed on lithium-oxygen cathodes, which can be easily extended to other metal-air systems and all those materials where oxygen redox reactivity is involved.

2. Metal-air batteries and the nature of discharge products

With lithium ion batteries becoming a mature technology, it is now clear that applications such as electric vehicles require chemistries with higher energy density to reach acceptable driving ranges without compromising performance and comfort already common with conventional vehicles. This pushed high research efforts in the area of lithium-air (or more precisely lithium-oxygen) batteries, presenting the highest energy density among known scalable battery devices, and of metal-air batteries in general. However, the difficulty to obtain a high reversibility and long cycle life still implies a significant barrier to become a technology. Compared to conventional lithium-ion batteries the reversibility and cycle life of metal-air batteries is generally frustrating [1]. While in a lithium-ion battery the main process is essentially ion transport through different phases that essentially leave electrode interfaces unaffected, in metal-air batteries reversible electrodeposition processes have to take place at the electrodes. For instance, with a lithium anode and aprotic electrolytes molecular oxygen is reduced and precipitates as insulating lithium peroxide inside a porous carbonaceous cathode [2]:

$$\text{Anode: } 2\,\text{Li} \rightarrow 2\,\text{Li}^+ + 2\,\text{e}^-$$
$$\text{Cathode: } \text{O}_2 + 2\,\text{Li}^+ + 2\,\text{e}^- \rightarrow \text{Li}_2\text{O}_2\downarrow$$

http://dx.doi.org/10.5772/66978

The latter reaction may proceed through two subsequent one-electron oxygen reduction steps or through chemical disproportionation of electrochemically generated superoxide:

$$Li^+ + O_2 + e^- \rightarrow LiO_2$$

$$2\,LiO_2 \rightarrow Li_2O_2\downarrow + O_2$$

This implies problems of controlling nucleation and growth processes, but more importantly the oxygen chemistry hugely increases complexity and triggers parasitic reactions with the organic electrolyte and with both electrodes [3, 4].

However, the control of texture, composition, and crystallinity of the discharge products can also have important consequences on the capacity, rate capability, and reversibility. In fact, capacity directly depends on the discharged peroxide volume, which depending on its morphology can be more or less well distributed in a given porous network before it becomes clogged or passivated [5]. The size of the precipitate particles also affects rechargeability: conditions that favor deposition of smaller particles obtain better reversibility [6, 7], likely for the more favorable surface-to-volume ratio. Evidence of the reaction intermediate superoxide in the precipitate has been reported [8–11] and it has been demonstrated that this is easier to oxidize than peroxide [12]. In effect Na/O_2 and K/O_2 cells, where superoxide prevails, have remarkably higher reversibility than Li/O_2 [13, 14].

A precise characterization of the nature and the evolution of the discharge products, and in particular the oxidation state of oxygen, is therefore essential to understand the processes underlying the electrochemical behavior of the cell, and can lead to improvements in materials and operating conditions. Given the light elements involved and the poor stability of incompletely reduced Li-O compounds many imaging, spectroscopic, or diffraction techniques are not suitable for their compositional analysis. In addition, amorphous phases are occasionally possible with Li_2O_2 (which may benefit rechargeability) [15] and usual with Li superoxide [10]. It is then evident that a technique such as full-field transmission spectromicroscopy has high value, being able to accurately spatially resolve distributions of superoxide, peroxide, and other oxygen compounds even within a single particle, and regardless of crystallinity.

3. Full-field transmission soft X-ray spectromicroscopy

In this paragraph the full-field transmission spectromicroscopy technique will be shortly explained. In Section 3.1, some basic concepts will be introduced following references [16, 17]. Then two possible experimental setups, the scanning and the full-field X-ray transmission microscope will be compared [16]. Finally, a brief paragraph will describe the full-field transmission microscope installed at the Mistral beamline (Alba Light Source, Spain) [18, 19].

3.1. The interaction of X-rays with matter

Usually for X-rays, the refraction index is written as:

$$n(\omega) = 1 - \delta(\omega) - i\beta(\omega) \tag{1}$$

while $E = \hbar\omega$ is the energy of the incident radiation. It is interesting to consider the asymptotic trend of δ and β for high energy (E far from absorption edges):

$$\delta(E) \propto \frac{1}{E^2} \quad \beta(E) \propto \frac{1}{E^4} \tag{2}$$

Let us consider now the propagation of a plane wave in the sample. Assuming **kr** = kr and using the *dispersion relation* $k^2 = \omega^2 n^2/c^2$, one has:

$$\mathbf{E}_0 e^{i(\omega t - kr)} = \mathbf{E}_0 e^{i[\omega t - \frac{\omega}{c}(1-\delta-i\beta)r]} = \mathbf{E}_0 e^{i(\omega t - k_0 r)} e^{ik_0\delta r} e^{-k_0\beta r} \tag{3}$$

where $k_0 = \omega/c = 2\pi/\lambda$ is the wave vector in vacuum. In Eq. (3), the first factor is the phase advance had the wave been propagating in vacuum; the second factor containing δ represents the modified phase shift due to the interaction with the medium; and the last factor containing β represents the decay of the wave amplitude in the medium due essentially to photoelectron absorption for X-rays. Hence, the phase shift due to the interaction with the sample is determined by δ, while the attenuation by β. The *linear absorption coefficient* μ is defined as the inverse of the distance into the material for which the intensity related to the wave amplitude, Eq. (3), is diminished by a factor $1/e$. Using Eq. (3):

$$\mu(E) = \frac{4\pi}{\lambda}\beta(E) \tag{4}$$

It is usually measured in μm^{-1} and the corresponding characteristic distance is called the *attenuation length*. μ is a rapidly increasing function of the atomic number and a rapidly decreasing function of the energy, taking into account Eq. (2):

$$\mu(E) \propto \frac{1}{E^3} \tag{5}$$

and at some particular energies called "absorption edges" it has peaks that correspond to the energies required to eject an electron from an internal core level to a final available electronic state. It is useful to introduce the *mass absorption coefficient*, defined as

$$\mu_m = \frac{\mu}{\rho} \tag{6}$$

with ρ being the mass density, $\rho = m_a n_a$ (m_a is the atomic mass, n_a is the density of the atoms).

To properly account for the transitions corresponding to the absorption edges, the use of quantum mechanics is needed. Considering a well-defined initial core state and using the *Fermi golden rule* in the *dipole approximation* one can write μ_m as:

http://dx.doi.org/10.5772/66978

$$\mu_m(E) \propto \left| \langle \psi_i | \hat{\varepsilon} \cdot r | \psi_f \rangle \right|^2 \rho_f(E_f) \tag{7}$$

where ψ_i and ψ_f are the initial and final single electron states, E_i and E_f are the corresponding energies and $E = E_f - E_i$ is the energy of the incident photons, ρ_f the density of final state, and $\hat{\varepsilon}$ the polarization of the electric field. The interaction between the atom and the electromagnetic field, classically pictured by the wave in Eq. (3), removes an X-ray photon whose energy is used to promote an electron from the initial core state ψ_i to the final state ψ_f. The absorption is modulated by the density of final state which has peaks in correspondence of the absorption edges. The dipole matrix element, almost flat with the energy, contains the angular momentum selection rules for dipole transitions (l = orbital angular momentum, s = spin, j = total angular momentum, m = z-component of the total angular momentum):

$$\Delta l = \pm 1, \quad \Delta s = 0, \quad \Delta j = \pm 1, 0, \quad \Delta m = 0 \tag{8}$$

and the dependence on the direction of the photon polarization $\hat{\varepsilon}$.

X-ray absorption imaging technique consists in detecting the photons transmitted through the observed object. Experimentally, the number of photons N after the transmission through the sample, along z, obeys to the *Beer-Lambert's law*:

$$N(x, y) = N_0(x, y) \exp\left[- \int_{\text{sample}} \mu(x, y, z)\, dz \right] \tag{9}$$

where N and N_0 are the emerging and incident number of photons, respectively, and the integral is extended through all the sample thickness. The measured transmission $T = I/I_0$ (with I and I_0 proportional to N and N_0, respectively) depends exponentially on the linear absorption coefficient μ, integrated along the X-ray path in the sample (**Figure 1**).

In a transmission microscope based on X-ray photons, the contrast will therefore depend on the sample thickness, the elements by which it is composed, their density, and the energy and polarization of the incident radiation. Assuming not oriented samples (so that we neglect the polarization) and μ constant along z in a thickness t, we can write:

$$\mu(x, y, E)\, t = \mu_m(x, y, E)\, \rho t = -\ln\left(\frac{I}{I_0}\right) \tag{10}$$

This product is proportional to the *absorbance A*, which is defined as $A = -\log_{10}(I/I_0)$, and is usually considered in the place of the transmission because of its additivity:

$$\mu t = \sum_i \mu_i t_i \tag{11}$$

Figure 1. Optical absorption and the Beer-Lambert's law.

which, for the particular case of i chemical species in a thickness t, becomes:

$$\mu t = t \sum_i \mu_{m,i} \rho_i \tag{12}$$

As a function of the photon energy parts of the images will then suddenly become darker (or brighter if we use the absorbance) when the radiation is triggering some electronic transitions allowed by Eqs. (7) and (8). As the exact energy is also dependent on the atom environment, it will also be possible to detect chemical states of the same element. This chemical information is available with spatial resolution down to few tens of nanometers in a synchrotron-based transmission X-ray microscope and the corresponding technique is called transmission X-ray spectromicroscopy. By using X-rays of the "soft" energy region (<3 KeV), it is possible to access transitions from core levels of light elements, among them the K-edge of nitrogen, oxygen, fluorine, as well as L – and M - edges of other elements (**Figure 2**).

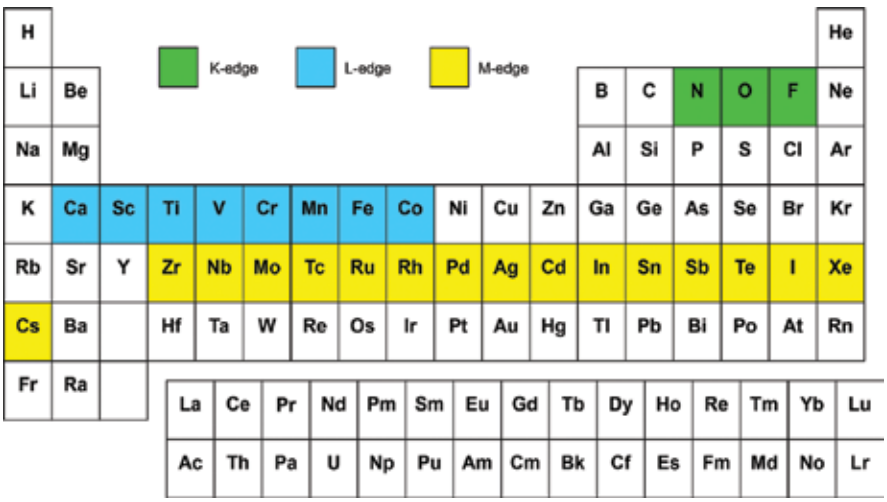

Figure 2. Accessible absorption edges with a soft X-ray radiation of 300–800 eV in the periodic table.

3.2. Zone plate-based X-ray transmission microscopes

Using the "radiography setup" depicted in **Figure 1**, the spatial resolution would be limited by the detector pixel size to few microns. In lens-based microscopy, this limit is imposed by the lenses. In the following we will briefly describe two examples of lens-based microscope geometries used at synchrotron radiation sources: the full-field transmission X-ray microscope (TXM) and the scanning transmission X-ray microscope (STXM), both represented in **Figure 3**.

http://dx.doi.org/10.5772/66978

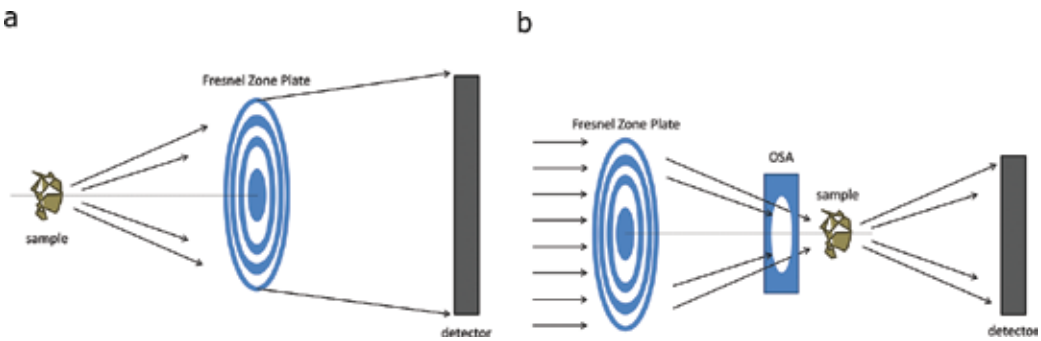

Figure 3. Scheme of the two common transmission X-ray microscopes: (a) Full-field microscope, in which a full sample image is formed on the detector; (b) Scanning microscope, in which the sample is scanned in the focal spot of the incoming beam.

Both of them are lens microscopes based on the application of Fresnel Zone Plate diffractive lenses (ZP). A ZP lens works like a circular diffraction grating whose period radially decreases from the center in such a way that all the waves of the same diffracted order are redirected to the same point (**Figure 4**). The expression for the focal length can be calculated as:

$$f \cong \frac{4N(\Delta r)^2}{\lambda} \tag{13}$$

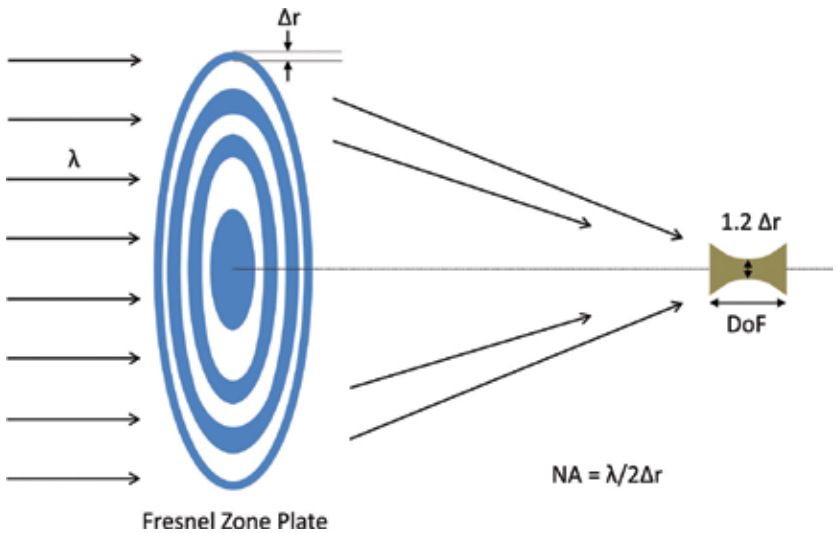

Figure 4. Conceptual scheme of a Fresnel Zone Plate lens.

Present technology allows the fabrication of ZP capable to produce focal spots down to few tens of nanometers (≥15 nm) [20]. Spatial resolution (r_s) and depth of focus (DoF) both depend

on λ and the *numerical aperture* (NA) of the lens which is, in the case of ZP lenses, related to the dimension of the outermost zone width Δr:

$$r_s = \frac{0.61\lambda}{NA} = 1.22\Delta r \quad DoF = \pm\frac{1}{2}\frac{\lambda}{(NA)^2} = \pm\frac{2(\Delta r)^2}{\lambda} \tag{14}$$

In the first equation of (14) the spatial resolution is defined following the *Rayleigh* criterion. It is interesting to note that a better spatial resolution will imply also a smaller DoF.

The nanofabrication of a ZP is typically realized on a thin silicon nitride membrane and involves high technology processes such as electron beam lithography. In general, the choice of the material for the ZP's opaque zones determines the efficiency depending on the energy range. For the TXM case we have the typical scheme of a common visible light microscope: a sample is placed at the focal plane of two lenses. The first lens is usually called "condenser" and it focalizes the beam on to the sample plane, while the second lens is called "objective lens" and it produces a full magnified image of the sample on to the detector plane. The objective lens is a ZP lens which works as a *thin lens* between the sample and the detector plane so that the magnification M is:

$$M = \frac{p}{q} \tag{15}$$

With p being the distance ZP-detector and q being the distance ZP-sample as indicated in **Figure 5**.

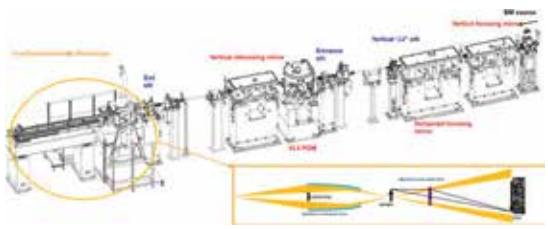

Figure 5. Mistral beamline layout. In the inset, a scheme of the TXM optics setup is reported.

The spatial resolution is limited by the NA of the objective lens, i.e., by the external zone width of the ZP lens as indicated in Eq. (14). This limit is reached if the microscope operates at M big enough to neglect the dimension of the pixels size of the detector (typically a CCD-based detector) and if the NA of the objective lens is filled by the beam emerging from the sample. Also, the ZP lens is strongly chromatic as indicated by Eq. (13), so that also a minimal requirement on the energy resolution of the incident beam has to be satisfied: $\Delta\lambda/\lambda \leq 1/N$, with N being the number of zones.

In a STXM system, the sample is placed in the focal spot of a ZP lenses. If illuminated with the proper coherent beam the ZP will produce a focal spot (more precisely an *airy pattern*) with

resolution set again by the first equation of (14). In this case, higher order diffracted beams will be stopped using an order sorting aperture (OSA) as indicated in **Figure 3**. The sample is scanned through the ZP focal spot and the full image of the sample is reconstructed electronically, step by step. The spatial resolution will be limited by the dimension of the focal spot produced by the ZP on the sample. **Table 1** summarizes the main properties of the two microscopes.

TXM	STXM
Best spatial resolution	Good spatial resolution
Shortest exposure time	Longer exposure time
Higher radiation dose	Least radiation dose
	Requires spatially coherent radiation

Table 1. Comparison between the main properties of full-field and scanning transmission electron microscopy.

The main advantage of the STXM over the TXM system is in terms of radiation dose: the lens is before the sample and then all the photons emerging from the sample are used to produce the image. Instead in a TXM system, the ZP is after the sample: due to its limited efficiency, most of the photons arising from the sample will not contribute to the formation of the image, therefore to obtain the same image quality of a STXM, the TXM will require more radiation dose absorbed by the sample. The main advantage of the TXM over the STXM system is in terms of the exposure time: in one "snapshot" the full image of the sample is obtained.

3.3. The MISTRAL microscope

An example of a state-of-the-art soft X-ray full-field transmission microscope is the one installed at the Mistral beamline of the ALBA Light source. A picture of the beamline (BL) is reported in **Figure 5**. The BL is devoted to transmission cryotomography of biological cells in the water window energy range (284.2–543.1 eV [21]). It is useful to distinguish between the BL optical elements and the TXM which is just the end station of the BL, as indicated in the picture. Presently the TXM can works in the energy range (ER) between the C–K edge and the Ni L edge excluded, i.e., 290–850 eV. All the optical elements before the TXM work to prepare the beam for the condenser lens of the microscope and are in ultra-high vacuum chambers (working $p \sim 1 \times 10^{-9}$ mbar) to minimize absorption and scattering of the X-ray beam. Moreover, the full beamline from the source to the CCD detector chip is windowless. In the case of Mistral the condenser lens is a glass capillary which work like a single reflection elliptical mirror. It is characterized by a good efficiency (50–75% in the ER) and achromaticity: its focal length of about 1 cm is energy independent. The 2 × 2 μm^2 condenser focal spot is wobbled to cover a field of view of typically 10 × 10–16 × 16 μm^2 on the sample plane. Two ZP are available as objective lens: 25 and 40 nm ZP. The first one is used typically for experiments

in which one wants to maximize the 2D spatial resolution and the depth of focus is not a critical parameter. More technical details on the MISTRAL beamline are reported in references [18, 19].

4. Spectromicroscopy at the O K-edge of discharged cathodes

In this section, we describe the preparation, collection, and analysis of cathodes used in Li-oxygen batteries, although most of the principles and considerations may well apply to other systems and energy regions.

4.1. Sample preparation and transfer

For images of optimal quality, we take common carbon-coated Au TEM grids (200 mesh, 3.05 mm diameter) directly as a cathode. Gold works as a current collector that is inert in the cathode electrochemical window, while carbon provides an ideal substrate for transmission microscopy. However, also a few micrograms of super P/PVdF slurry are deposited on the TEM grids to provide a roughened surface closer to that present in practical electrodes.

Electrochemical treatments are performed using homemade cell based on the Giessen battery design [13], resulting in Swagelok-like battery arrangement. After the electrochemical treatment the cell is opened in an Ar-filled glove box and the grid washed with DME and hexane to fully remove the electrolyte. The grid is then transferred in the microscope in cryogenic condition (T < 110 K) under N_2 vapor to minimize atmospheric contamination. The samples are kept at cryogenic temperature and under high vacuum during the measurements.

4.2. Measurement protocol

Selection of a field of view consists of two steps, first an overview of the TEM mesh with a visible light microscope (VLM), and then selection of a specific mesh hole where a 100 μm × 100 μm mosaic image can be composed by 10 × 10 individual TXM images (see **Figure 6**). Repeating mosaics at two energies, above and below the O K-edge can be useful for a first localization of oxygen compounds.

For the case of the O K level, XANES images are collected varying the incident photon energy with an exposure time of 2 s at each energy step. For each energy step, a flat field image (FF), i.e., an image without the sample, is recorded. An energy range of 515–580 eV ensures the most reliable spectral normalization and allows EXAFS analysis. The energy step can be adjusted between 0.1 and 0.5 eV depending on the spectral features to record. The objective zone plate lens (outermost zone width of 40 nm, 937 zones) and the CCD detector positions are automatically adjusted to maintain focus and constant magnification. The CCD motion is the slowest part of acquisition which typically requires between 1 and 2 h.

http://dx.doi.org/10.5772/66978

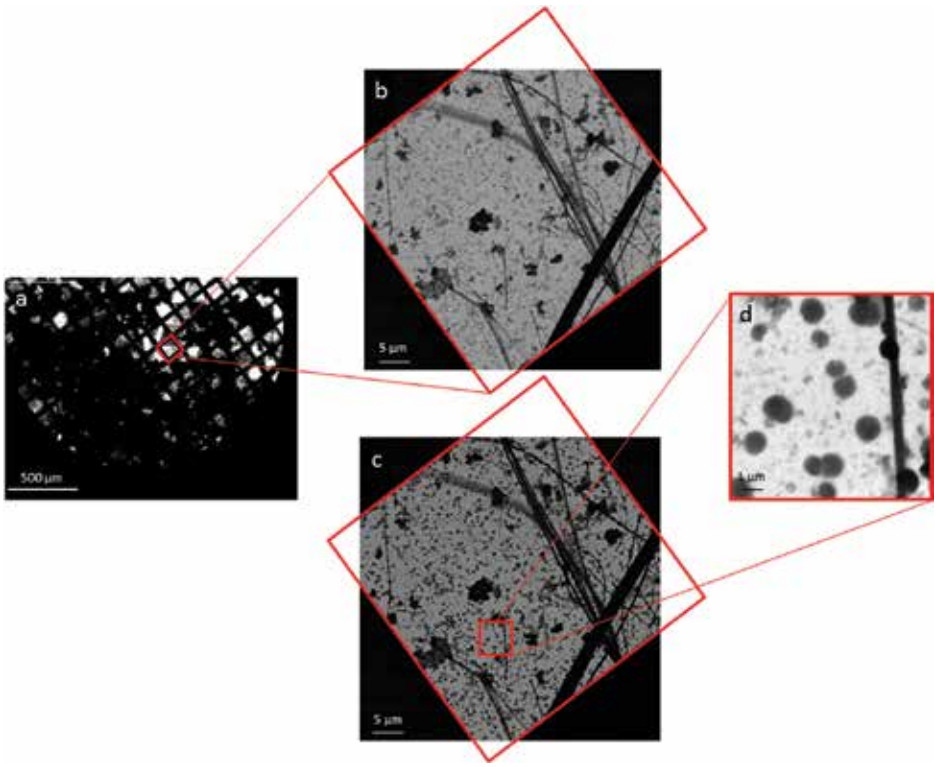

Figure 6. Stepwise selection of a field of view: grid overview by VLM (a), mosaic TXM image of an individual mesh hole before (b) and after (c) the O-K edge, and TXM field of view (d).

4.3. Radiation damage

A recurring issue in techniques involving high brilliance light is the sample stability to irradiation. This is often considered a major problem with organic compounds, whereas inorganic compounds are regarded as essentially stable [22]. However, Li_2O_2 is also very sensitive. For instance, in our own experience, electron microscopy requires special care, as the electron beam is able to fully decompose a micrometric layer of lithium peroxide in a few seconds, as shown in **Figure 7**.

Qiao et al. [24] specifically studied the effect of irradiating lithium peroxide, oxide, and carbonate with soft X-rays at room temperature. They found that carbonate and peroxide evolve toward oxide within several minutes of irradiation. In contrast with their respective electrochemical oxidation stability, the evolution of carbonate is faster, with oxide features appearing after 1 h for peroxide and already after 20 min for carbonate. The stability of a given compound depends on the activation process. However, in general, the high cross-section of soft X-rays implies a stronger interaction with matter and consequently a faster degradation than hard X-rays, in particular when the photon energy is close above the absorption edge of elements such as C and O.

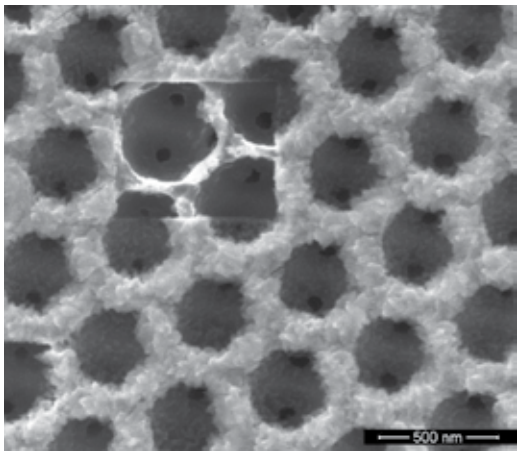

Figure 7. SEM image showing the effect of the electron beam on the deposits of a Li/O_2 discharged cathode. The support is a carbonaceous inverse opal [23]. The deposit-free rectangle has been obtained after scanning during about 1 min for a higher magnification image.

This problem is obviously of special relevance for biologic samples, which are always observed with soft X-rays in cryogenic conditions. The lower nuclear thermal motion favors the reconstruction of the bonds excited by radiation, significantly improving the sample stability. For this reason, we also keep our discharged electrodes at $T < 110$ K (liquid nitrogen) during irradiation with soft X-rays. Under these conditions, we can irradiate long enough to gain acceptable signal to noise and energy step without evident damage. As an example, **Figure 8** compares two O K-edge XANES spectra (duration about 2 h each) of a sample recorded before (red) and after 24-h period (blue). Spectra demonstrate very good reproducibility corresponding to no detectable radiation damage within our resolution and experimental noise.

4.4. Reference samples

Reference samples are essential for correct assignment of the peaks found in the sample. They must be measured in the same conditions and preferably in the same session to allow similar instrumental peak broadening and proper spectra subtraction. This is useful to detect components that may be masked by more abundant species.

Unfortunately, commercial compounds may not always correspond exactly to the expected composition. Although also commercially available, we have chemically generated Li_2O_2 from the reaction of KO_2 with dicyclohexyl-18-crown-6 (crown ether) in solution [25]. We have obtained images of the precipitate with different local O K-edge XANES spectra. By inspection of the spectra at different points of the images we concluded that locally rather pure phases of both Li_2O_2 and Li_2CO_3 coexisted, being the first in agreement with the literature [24], and the second with a commercial sample we measured. LiO_2 can only be hardly obtained in a pure

http://dx.doi.org/10.5772/66978

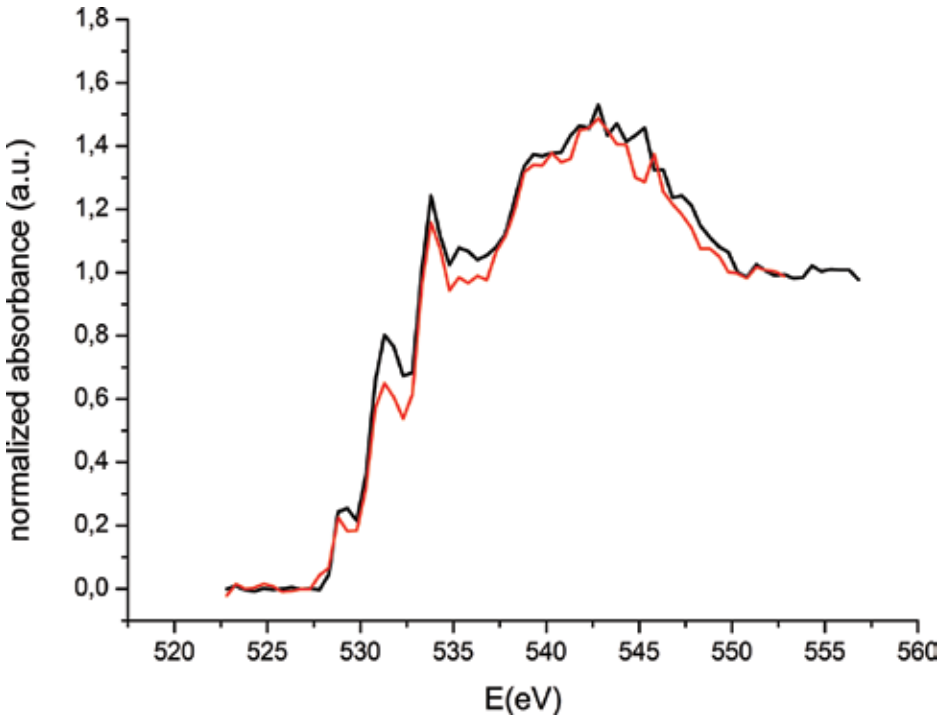

Figure 8. O K-edge XANES spectra of discharged sample before (black) and after (red) 24-h in the same experimental condition. Reprinted with permission from Olivares-Marín et al. [11]. Copyright 2015 American Chemical Society.

form [12, 26], and we used just a literature absorption spectrum as reference [26], mainly to confirm its energy.

4.5. Data analysis

4.5.1. Images normalization, alignment, and spectra extraction

As a first step, each image of the energy scan is normalized to one using the corresponding FF. This normalization consists in simply dividing the image with the sample by the corresponding FF, obtaining the transmission $T = I/I_0$ as a function of the energy (see Section 3.1). In the transmission only, the measured intensity variations along the energy scan due to the sample itself are taken into account, all the contribution coming from the optical setup (beamline and microscope optics) are discarded. The normalized images (or transmission images) present drifts along the scan due to the relative movement between the ZP lens and the CCD detector. Therefore, the image sequence needs to be aligned. At Mistral for instance this is done using a in-house software named "ctalign." Each of the images is aligned taking as reference a chosen ROI of the first image of the scan. The software uses the normalized cross-correlation of both ROIs to detect the best matching between them. Once aligned, the absorbance images can be simply obtained from the corresponding transmission images using Eq. (10), i.e., calculating

the –log of the series. The free NIH ImageJ software [27] is for instance useful to handle the aligned TXM images and doing calculations with them.

By taking the average absorbance from a given region of an image for all images, the absorption spectrum for that region is obtained. In principle, the technique gives access to a single pixel spectra analysis, practically the dimension of the selected region is limited by the lens resolution, the effectiveness of the series alignment, and single pixel spectra noise to 5–6 pixels[2].

4.5.2. Spatial distribution of the discharge products

Given that the different oxygen reduction states present in discharged metal/oxygen electrodes (superoxide, peroxide, and carbonate) are characterized by distinct absorption peak energies (around 529, 531, and 533 eV, respectively) oxygen-state-resolved maps can be obtained. A full quantitative approach consists in measuring a full set of pure reference samples (superoxide, peroxide, and carbonate in our case) and fit with them the obtained measured spectra. If measured reference spectra are not available some sophisticated linear algebra technique such as principle component analysis and factor analysis can also be used for the interpretation of XANES spectra. The number of principal components determined in this way was used as the basis for multivariate curve resolution-alternating least squares (MCR-ALS) analysis [28]. However, precise and accurate calculations of all spectral features are still difficult and not always reliable. Presently, quantitative analyses of XANES spectra using *ab initio* calculations are very rare, and a full description of absorption spectra data analysis and interpretation is beyond the scope of this paragraph. Here, we will describe a simple, qualitative/semiquantitative approach based on the construction of absorbance image differences D obtained from single absorbance images at specific energies. Let us consider two chemical species A and B in a thickness t, then the corresponding absorbance will be (from Eq. 12):

$$\mu(E)\,t = (\mu_{m,A}(E)\,\rho_A + \mu_{m,B}(E)\,\rho_B)\,t \tag{16}$$

where $\mu(E)\,t$ represents the intensity map in the absorbance image at a generic energy E. Now if we choose the two values of the energy position of the absorption edge peak maximum and minimum, respectively, of the species A for instance ($E_{\mathrm{MAX,A}}$ and $E_{\mathrm{min,A}}$ in **Figure 9**), we can write for the corresponding absorbance difference D_{A}

$$D_A = (\mu_{m,A}(E_{\mathrm{MAX},A})\,\rho_A + \mu_{m,B}(E_{\mathrm{MAX},A})\,\rho_B - \mu_{m,A}(E_{\mathrm{min},A})\,\rho_A - \mu_{m,B}(E_{\mathrm{min},A})\,\rho_B)\,t \tag{17}$$

$$\text{and assuming } \mu_{m,B}(E_{\mathrm{MAX},A}) \approx \mu_{m,B}(E_{\mathrm{min},A}), \tag{18}$$

$$D_A \approx (\mu_{m,A}(E_{\mathrm{MAX},A}) - \mu_{m,A}(E_{\mathrm{min},A}))\rho_A\,t \tag{19}$$

If $\mu_{m,A}(E_{\mathrm{min},A}) \ll \mu_{m,A}(E_{\mathrm{MAX},A}) \Rightarrow D_A \approx \mu_{m,A}(E_{\mathrm{MAX},A})\,\rho_A t$, that is the absorbance image difference D_{A} is proportional to the concentration map of the chemical specie A. Doing the same for the specie B, we have:

http://dx.doi.org/10.5772/66978

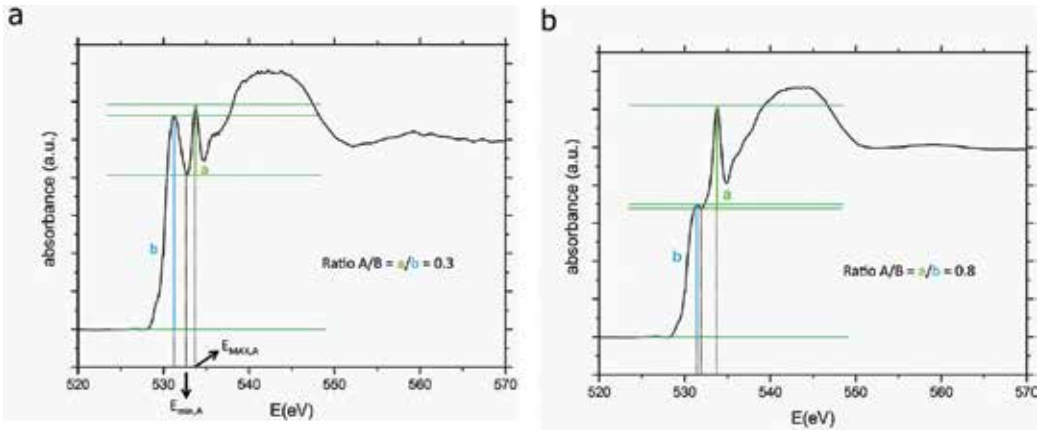

Figure 9. Two examples of fraction estimation for different components in integrated spectra.

$$D_B \approx \mu_{m,B}(E_{MAX,B})\,\rho_B\,t \tag{20}$$

and then for the ratio between the two species: $\frac{D_A}{D_B} \propto \frac{\rho_A}{\rho_B}$. The corresponding estimation in integrated spectra is shown in **Figure 9**.

Under these considerations we have used absorbance images corresponding to the relative maximum absorbance of LiO_2 (528.75 eV), Li_2O_2 (531.25 eV), and Li_2CO_3 (533.8 eV). The image at 520 eV was subtracted from that at 528.75 eV to obtain the 2D LiO_2 distribution, and the image at 528.75 eV was subtracted from that at 531.25 eV to obtain the one for Li_2O_2. Also, Li_2CO_3 was calculated subtracting image at 531.25 eV minus image at 533.8 eV. Three distribution images obtained were then merged with different colors.

From these maps and possibly calibrating the image intensity using reference samples with known ratio between species, it is possible to obtain profiles or images of ratios and fractions, which is useful to establish correlations or associations between species.

5. Some case studies

Thanks to the measurement and analysis procedure described above, synchrotron-based energy-dependent transmission soft X-ray microscopy (TXM) provides a unique access to the chemical state, spatial distribution, and morphology of oxygen-containing materials in particular when they present different oxidation states, regardless of their crystalline state. Given its lateral resolution, this technique is also able to reveal minor components that are not evident in the integrated spectra, but are well localized. In this part we will illustrate the potential of this technique with some examples of energy-dependent TXM measurements on cathodes discharged in Li/O_2 cells. In fact, this allows detecting different oxygen-bearing components among the discharge products of electrodes, and associating it to its characteristic shape. In this way it is possible to quantify and localize the distribution of the oxygen discharge products, revealing lithium superoxide, peroxide, hydroxide, and carbonates.

5.1. Spatial distribution of products

The discharge products of Li/O_2 batteries are reported in the literature with different morphology and composition. When the product is well crystalline electron diffraction coupled to TEM may help to assign a given composition to a certain morphology. In our case, we can attribute a composition to most oxygen-bearing objects, regardless of the crystallinity. To illustrate this, **Figure 10** shows a typical example. The overall spectrum of this sample presents features of superoxide (529 eV), peroxide (531 eV), and a component typical for fully oxidized oxygen, such as carbonate or hydroxide (533 eV). However, spectra at different points differ significantly, which implies that heterogeneity is larger than the spatial resolution, and that the spectral (and hence chemical) difference between the various independent components is remarkable. By inspecting differential images we can localize the spots where each component has maximum concentration. We can distinctly observe oblate particles with an essentially peroxide composition, probably corresponding to platelets reported in the literature [29]. Centering at the 533 eV peak some needle-like particles, but also a more diffuse background can be imaged. Local spectra strongly suggest a hydroxide-like composition. The weaker superoxide component cannot be localized at specific points. A very characteristic spectrum, that is not evident in the overall spectrum, is instead found in a few spots, and corresponds to ice, probably deposited during the transfer process. Even if this component is external to the cathode material, it shows that statistically less relevant components that do not appear in the total spectrum can be detected if spatially well localized. Thus, the fluctuating local spectra not only greatly facilitate the attribution of the components that appear mixed in the integrated spectrum, but even allow lowering the detection limit.

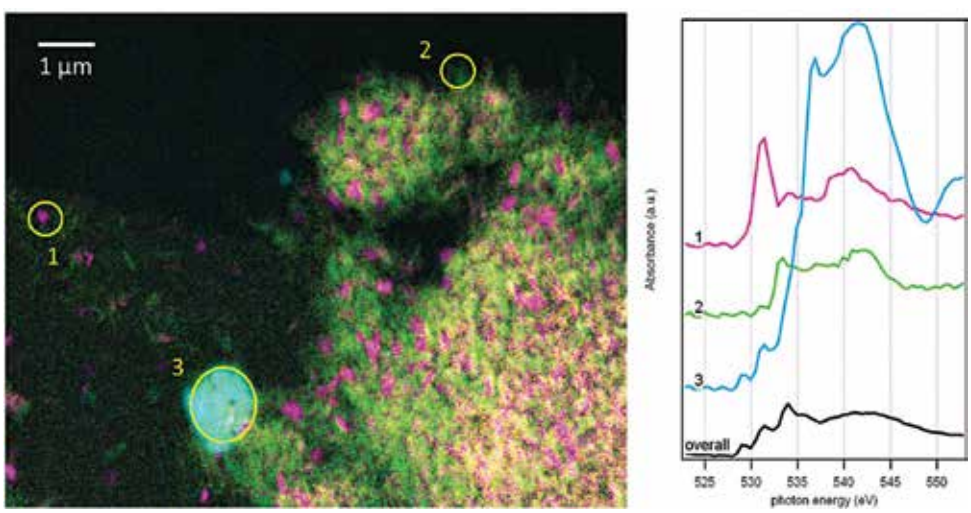

Figure 10. Left: Combination of differential images for different spectral components. Each component is represented with a respective color: superoxide (yellow), peroxide (magenta), hydroxide (green), and ice (cyan). Right: Absorption spectra in the O K region at selected points and for the overall image.

http://dx.doi.org/10.5772/66978

5.2. Toroidal particles

The sample reported in **Figure 11** includes the characteristic toroidal-shaped particles also reported by several authors working with ether-based solvents. Beside these main objects, we actually also appreciate platelet-like particles and irregular aggregates. Also in this case, differently shaped particles present different composition. Small platelets and irregular particle aggregates are mainly composed of carbonate (red). Instead, Li superoxide and peroxide dominate in toroidal objects (green). From intensity maps, it is also possible to generate ratio or fraction maps that are useful to tell if some components are associated.

Such estimations indicate that toroidal peroxide particles included 10–30% superoxide-like phases. Superoxide does not appear to show any preferential localization with respect to peroxide in the particles, suggesting some coprecipitation mechanism that may favor toroid formation. In fact, smaller particles have smaller superoxide content than large particles. Significant amount of carbonates were found irregularly distributed on the electrode, appearing as aggregates, but also coating lithium peroxide particles. A closer analysis suggests that carbonates form a shell on the surface of all particles, so that smaller particles seem associated to relatively larger quantities of carbonate. This resembles a passivating layer, indicating that carbonate formation is a surface reaction and forms a kind of passivating layer. Thus, a strategy for more reversible batteries appears to be conditions that favor operation with larger particles.

5.3. Redox mediators and recharge

The use of redox mediators has opened an important strategy to recharge lithium-oxygen batteries [30]. These are redox-active soluble molecules, which are able to readily oxidize electrochemically during charge, and then reach the peroxide deposits giving place to a chemical redox reaction that evolves oxygen and switches back the molecule to its reduced state. By providing alternative electron paths from the insulating peroxide to the electrode collector, they act as catalysts, with considerable decrease of overpotentials increased charging rates and efficiencies. One of the requirements for the mediator is its stability to the electrochemical conditions, in effect we found UV-visible spectroscopy evidence that oxygen actually reacts with the mediator iodide [31]. Other authors instead have shown that the product may also be significantly affected by iodide [32]. By comparing **Figure 12** with **Figure 11** we could not notice any remarkable difference in the morphology or composition of fully discharged electrodes with or without iodide. Although in this case it is difficult to unambiguously detect subtle spectral changes that may prove small deviations in the irreversible processes, the information we obtain is more representative of the relative amounts of oxygen in different chemical states. This allows affirming. That overall the mediator iodine has practically no effect on the proportions of main and side Li/O_2 discharge products. When we eventually recharge the battery, using these small TEM grid-based electrodes, the voltage usually increases fast above 4 V vs. Li. With the iodide mediator we instead obtain a large charge profile (**Figure 12a**). During this profile, we can observe that toroids disappear fast (sample B). Then, we can see that the sample just shows circular imprints inside a carbonate-like material at the place of the toroids (sample C). The spectrum still shows some peroxide,

in agreement with the tiny yellow fragments that can be noted embedded in the carbonate matrix, without being accessible even to the mediators, making the corresponding capacity highly irreversible.

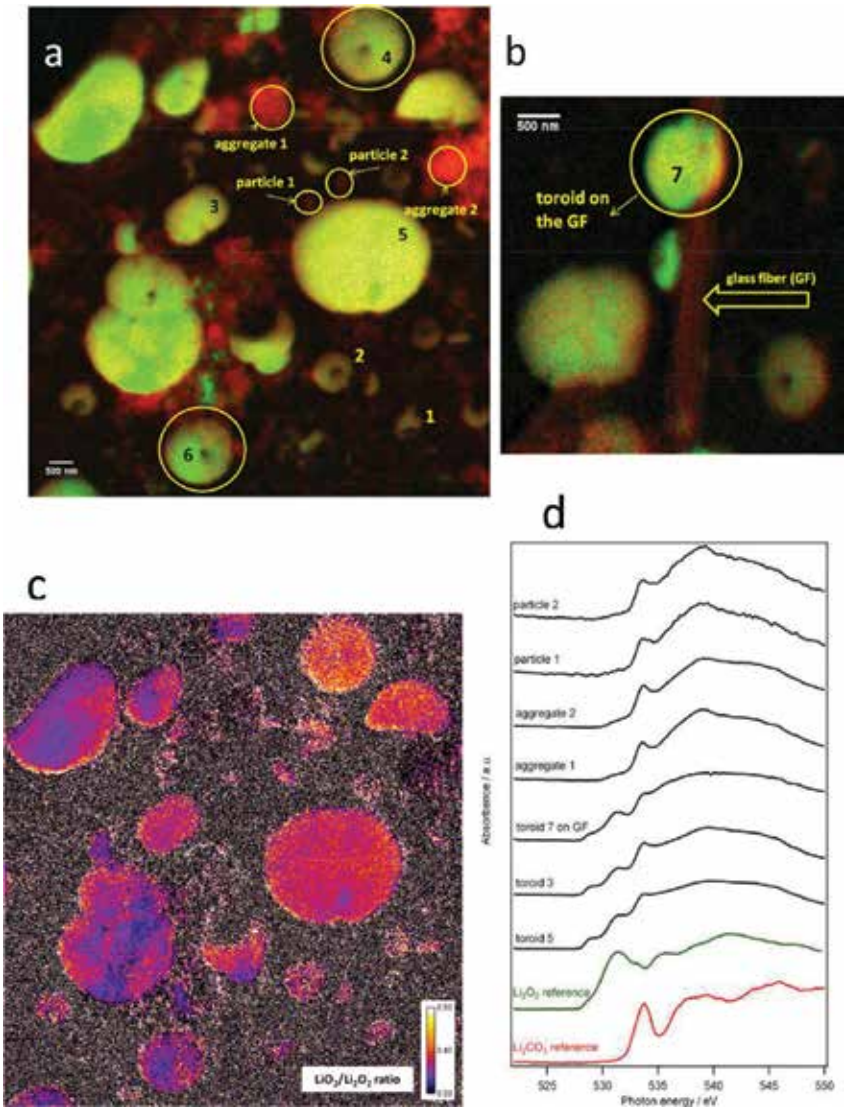

Figure 11. (a and b) TXM images of a carbon-coated Au TEM grid after being fully discharged in a Li-O_2 cell. The images are the result of overlapping three color maps with intensities proportional to the amounts of Li superoxide (cyan), Li peroxide (green), and carbonate (red). (c) Map of the LiO_2/Li_2O_2 ratio. The respective LiO_2 and Li_2O_2 intensities have been obtained by the same method. The gray noisy area results from regions with low LiO_2 and Li_2O_2 values. (d) Corresponding O K-edge XANES spectra at the selected points indicated by arrows in figures a and b, together with reference Li_2O_2 and Li_2CO_3 spectra. Reprinted with permission from Olivares-Marín et al. [11]. Copyright 2015 American Chemical Society.

http://dx.doi.org/10.5772/66978

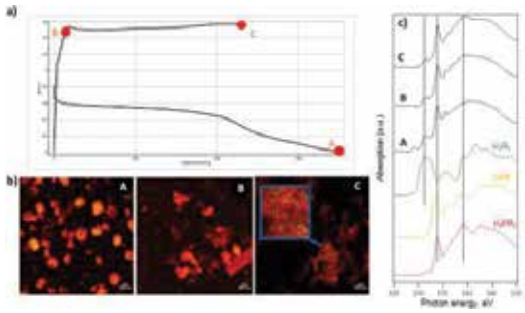

Figure 12. Galvanostatic discharge-charge profile of a TEM mesh-based cathode in a 1 M Li triflate electrolyte in TEGDME with a 0.02 M LiI additive (a), showing the position of three different samples. TXM images of the three samples (b) and corresponding overall O K spectra compared with references (c).

6. Conclusions

Full-field transmission soft X-ray microscopy is a powerful tool for the characterization of nanocomposites and nanostructured materials. Its high energy and space resolution provide accurate and semiquantitative chemical information at the scale of few tens of nm. This technique is particularly useful to inspect heterogeneities in all those materials involving the redox activity of several elements, including O and N. The unique access to the oxygen chemical state is extremely valuable to the investigation of metal air batteries. In this field, the technique contributes to understand the morphology and nature of the discharge products, their formation, and removal mechanism during discharge and charge of metal-air batteries. In particular, it is likely the most effective technique in detecting the critical superoxide component and its interplay with the other compounds present. The correlation between the respective spatial distributions gives one of the most comprehensive pictures of the reactivity and failure mechanisms, which hopefully will lead to strategies able to turn the Li/O_2 and other metal-air chemistries into a technological reality.

Acknowledgements

The X-ray microscopy experiments were performed at MISTRAL beamline at ALBA Synchrotron with the collaboration of ALBA staff. Alvaro Yamil Tesio is acknowledged for contribution to the experimental work. Work was funded by the Spanish Ministry of Economy and Competitiveness, through the "Severo Ochoa" Programme for Centres of Excellence in R&D (SEV- 2015–0496), and through project MAT2012-39199-C02-01, by the Generalitat de Catalunya (grant 2014 SGR 1505), and by the European Commission in the Seventh Framework Programme FP7-2010-GC-ELECTROCHEMICAL STORAGE, under contract no. 265971 "Lithium-Air Batteries with Split Oxygen Harvesting and Redox processes (LABOHR)". M.O.M. acknowledges CSIC for a JAE-DOC research contract cofinanced by the European Social Fund.

Author details

Dino Tonti[1]*, Mara Olivares-Marín[2], Andrea Sorrentino[3] and Eva Pereiro[3]

*Address all correspondence to: dino.t@csic.es

1 Institute of Materials Science of Barcelona, Spanish National Research Council (ICMAB-CSIC), Barcelona, Spain

2 CUM - University of Extremadura, Mérida, Spain

3 ALBA Synchrotron Light Source, MISTRAL Beamline – Experiments Division, Barcelona, Spain

References

[1] Luntz AC, McCloskey BD. Nonaqueous Li-air batteries: a status report. Chem Rev. 2014;114(23):11721–50.

[2] Christensen J, Albertus P, Sanchez-Carrera RS, Lohmann T, Kozinsky B, Liedtke R, et al. A Critical Review of Li/Air Batteries. J Electrochem Soc. 2012;159(2):R1–30.

[3] Yao X, Dong Q, Cheng Q, Wang D. Why do lithium-oxygen batteries fail: parasitic chemical reactions and their synergistic effect. Angewandte Chemie - International Edition. 2016;55(38):11344–53.

[4] Aurbach D, McCloskey BD, Nazar LF, Bruce PG. Advances in understanding mechanisms underpinning lithium–air batteries. Nat Energy. 2016;1(9):16128.

[5] Aklalouch M, Olivares-Marín M, Lee RC, Palomino P, Enciso E, Tonti D. Mass-transport control on the discharge mechanism in Li-O_2 batteries using carbon cathodes with varied porosity. ChemSusChem. 2015;8(20):3465–71.

[6] Gallant BM, Kwabi DG, Mitchell RR, Zhou J, Thompson CV, Shao-Horn Y. Influence of Li2O2 morphology on oxygen reduction and evolution kinetics in Li-O2 batteries. Energy Environ Sci. 2013;6(8):2518–28.

[7] Elia GA, Hassoun J, Kwak WJ, Sun YK, Scrosati B, Mueller F, et al. An advanced lithium-air battery exploiting an ionic liquid-based electrolyte. Nano Lett. 2014;14(11):6572–7.

[8] Yang J, Zhai D, Wang HH, Lau KC, Schlueter JA, Du P, et al. Evidence for lithium superoxide-like species in the discharge product of a Li-O2 battery. Phys Chem Chem Phys. 2013;15(11):3764–71.

[9] Frith JT, Russell AE, Garcia-Araez N, Owen JR. An in-situ Raman study of the oxygen reduction reaction in ionic liquids. Electrochem Commun. 2014;46:33–5.

[10] Zhai D, Lau KC, Wang HH, Wen J, Miller DJ, Lu J, et al. Interfacial effects on lithium superoxide disproportionation in Li-O2 batteries. Nano Lett. 2015;15(2):1041–6.

[11] Olivares-Marín M, Sorrentino A, Lee R-C, Pereiro E, Wu N-L, Tonti D. Spatial distributions of discharged products of lithium–oxygen batteries revealed by synchrotron X-ray transmission microscopy. Nano Lett. 2015;15(10):6932–8

[12] Lu J, Lee YJ, Luo X, Lau KC, Asadi M, Wang HH, et al. A lithium-oxygen battery based on lithium superoxide. Nature. 2016;529(7586):377–82.

[13] Bender CL, Hartmann P, Vračar M, Adelhelm P, Janek J. On the thermodynamics, the role of the carbon cathode, and the cycle life of the sodium superoxide (NaO2) battery. Adv Energy Mater. 2014;4(12):1301863.

[14] Ren X, Wu Y. A low-overpotential potassium-oxygen battery based on potassium superoxide. J Am Chem Soc. 2013;135(8):2923–6.

[15] Zhang Y, Cui Q, Zhang X, McKee WC, Xu Y, Ling S, et al. Amorphous Li2O2: chemical synthesis and electrochemical properties. Angewandte Chemie - International Edition. 2016;55(36):10717–21.

[16] Attwood D. Soft X-Rays and Extreme Ultraviolet Radiation: Principles and Applications. Cambridge: Cambridge University Press; 1999, 1999/008/28.

[17] Mobilio S. Interaction between radiation and matter: an introduction. In: Mobilio S, Vlaic G, editors. Synchrotron Radiation: Fundamentals, Methodologies and Applications. Vol. 82. Bologna: Società Italiana di Fisica; 2001.

[18] Pereiro E, Nicolas J, Ferrer S, Howells MR. A soft X-ray beamline for transmission X-ray microscopy at ALBA. J Synchrotron Radiat. 2009;16(Pt 4):505–12.

[19] Sorrentino A, Nicolás J, Valcárcel R, Chichón FJ, Rosanes M, Avila J, et al. MISTRAL: a transmission soft X-ray microscopy beamline for cryo nano-tomography of biological samples and magnetic domains imaging. J Synchrot Radiat. 2015;22(4):1112–7.

[20] Chao WL, Harteneck BD, Liddle JA, Anderson EH, Attwood DT. Soft X-ray microscopy at a spatial resolution better than 15 nm. Nature. 2005;435(7046):1210–3.

[21] Sayre D, Kirz J, Feder R, Kim DM, Spiller E. Potential operating region for ultrasoft X-ray microscopy of biological-materials. Science. 1977;196(4296):1339–40.

[22] Cazaux J. A physical approach to the radiation damage mechanisms induced by X-rays in X-ray microscopy and related techniques. J Microscopy-Oxford. 1997;188:106–24.

[23] Olivares-Marín M, Palomino P, Amarilla JM, Enciso E, Tonti D. Effects of architecture on the electrochemistry of binder-free inverse opal carbons as Li-air cathodes in an ionic liquid-based electrolyte. J Mat Chem A. 2013;1(45):14270–9.

[24] Qiao R, Chuang YD, Yan S, Yang W. Soft x-ray irradiation effects of Li(2)O(2), Li(2)CO(3) and Li(2)O revealed by absorption spectroscopy. PLoS One. 2012;7(11):e49182.

[25] Black R, Oh SH, Lee JH, Yim T, Adams B, Nazar LF. Screening for superoxide reactivity in Li-O-2 batteries: effect on Li2O2/LiOH crystallization. J Am Chem Soc. 2012;134(6):2902–5.

[26] Ruckman MW, Chen J, Qiu SL, Kuiper P, Strongin M, Dunlap BI. Interpreting the near Edges of O2 and O2- in alkali-metal superoxides. Phys Rev Lett. 1991;67(18):2533–6.

[27] Kremer JR, Mastronarde DN, McIntosh JR. Computer visualization of three-dimensional image data using IMOD. J Struct Biol. 1996;116(1):71–6.

[28] Jaumot J, Gargallo R, de Juan A, Tauler R. A graphical user-friendly interface for MCR-ALS: a new tool for multivariate curve resolution in MATLAB. Chemomet Intell Lab Syst. 2005;76(1):101–10.

[29] Zakharchenko TK, Kozmenkova AY, Itkis DM, Goodilin EA. Lithium peroxide crystal clusters as a natural growth feature of discharge products in Li-O2 cells. Beilstein J Nanotechnol. 2013;4(1):758–62.

[30] Chen Y, Freunberger SA, Peng Z, Fontaine O, Bruce PG. Charging a Li-O2 battery using a redox mediator. Nat Chem. 2013;5(6):489–94.

[31] Landa-Medrano I, Olivares-Marín M, Pinedo R, Ruiz de Larramendi I, Rojo T, Tonti D. Operando UV-visible spectroscopy evidence of the reactions of iodide as redox mediator in Li–O2 batteries. Electrochem Commun. 2015;59:24–7.

[32] Kwak W-J, Hirshberg D, Sharon D, Shin H-J, Afri M, Park J-B, et al. Understanding the behavior of Li–oxygen cells containing LiI. J Mater Chem A. 2015;3(16):8855–64.

Edited by Mehdi Khodaei and Luca Petaccia

Nowadays, nanomaterials are attracting huge attentions not only from a basic research point of view but also for their potential applications. Since finding the structure-property-processing relationships can open new windows in the application of materials, the material characterizations play a crucial role in the research and development of materials science. The increasing demand for energy with the necessity to find alternative renewable and sustainable energy sources leads to the rapid growth in attention to energy materials. In this book, the results of some outstanding researches on synchrotron-based characterization of nanostructured materials related to energy applications are presented.

ISBN 978-953-51-4896-8

Photo by fanjianhua / iStock

IntechOpen